Evaluating the Industrial Application of Non-destructive Inspection of Composites using Transient Thermography

by

Jared Eric Kretzmann

Thesis presented in partial fulfilment of the requirements for the degree of Master of Engineering (Mechanical) in the Faculty of Engineering at Stellenbosch University

Supervisor: Prof. Gerhard Venter
Co-supervisor: Prof. Kristiaan Schreve

March 2016

Declaration

By submitting this thesis electronically, I declare that the entirety of the work contained therein is my own, original work, that I am the sole author thereof (save to the extent explicitly otherwise stated), that reproduction and publication thereof by Stellenbosch University will not infringe any third party rights and that I have not previously in its entirety or in part submitted it for obtaining any qualification.

Date: March 2016

i

Abstract

Evaluating the Industrial Application of Non-destructive Inspection of Composites using Transient Thermography

J.E Kretzmann

Department of Mechanical and Mechatronic Engineering,
University of Stellenbosch,
Private Bag X1, Matieland 7602, South Africa.

Thesis: MEng (Mech)

March 2016

Transient thermography is a non-destructive testing method used in the detection and visualization of sub-surface flaws. Transient thermography could use one of two heating methods: step and square-pulse heating. Both these methods rely on observing the temperature rise of a surface that is subjected to a constant heat flux, while square pulse thermography also observes the subsequent thermal decay after the heat has been removed.

The transient methods have not been thoroughly explored in literature with respect to the more popular methods, such as pulsed and lock-in thermography. Particular interest has been placed on investigating transient thermography on fiber-reinforced polymer (FRP) materials and its application in industry.

Composites are prone to flaws such as delaminations, voids and inclusions that do not accurately represent flat-bottom holes, which are commonly evaluated in experimental work. Therefore, the inspection of thin artificial air-gaps and Teflon® delaminations were investigated. These artificial flaws can be considered to represent either a fully-separated or contacting delamination. A significant reduction in defect contrast and definition was observed for the thin delaminations, which is ascribed to the lower thermal resistance than that for flat-bottom holes.

Further studies investigated the qualitative and quantitative performance of thermographic inspection on defective samples provided by an industrial partner. Experimental results demonstrated that variability in core geometry, ply arrangement, surface and sub-surface anomalies could be identified. The smallest detectable anomaly was found to be 1 mm wide, which was a spatial resolution limitation of the infrared camera. The investigated samples

exhibited small radius and low resistance defects. It was found that current techniques to quantify defect depth are inadequate, especially if an accurate reference depth cannot be found.

Thermography data is typically associated with subtle defect signatures that are strongly affected by non-uniform heating and surface variability. Advanced processing methods have been shown to help mitigate these effects. Various processing methods are reviewed from literature. Several methods were tested here for the first time, such as: multiscale retinex, matched filters, Markov error contrast and modified differential absolute contrast (IDAC) for step thermography.

Transient thermography has shown to be a strong competitor amongst other thermographic methods for its simple application, relatively fast inspection times, and high thermal contrast for low defect resistance cases. It further enables the use of an entry-level infrared camera. The findings of the artificial samples reported a maximum defect depth up to 7 mm was observed for clear Plexiglas®. The clear Plexiglas® can be considered to be the least optimal case of heating with optical excitation and has a low thermal emissivity. For the carbon and glass fibre reinforced polymers, a maximum detectable defect depth of 5 mm was observed, which is considered to be comparative or even better than pulsed thermography. The method was particularly better for low diffusivity materials, such as glass fibre composites.

Uittreksel

AFRIKAANS

("Evaluering van die Industrële Toepassing van Nie-destruktiewe Inspeksie van Saamgesteldemateriale met Oorgangstermografie")

J.E Kretzmann

Departement Meganiese en Megatroniese Ingenieurswese,
Universiteit van Stellenbosch,
Privaatsak X1, Matieland 7602, Suid Afrika.

Tesis: MIng (Meg)

Maart 2016

Oorgangstermografie is 'n nie-destruktiewe tegniek om defekte onder die oppervlak waar te neem en te visualiseer. Oorgangstermografie kan een van twee verhittingsmetodes gebruik: stap en vierkant puls verhitting. Beide tegnieke is gebaseer op die waarneming van die temperatuur styging van 'n oppervlak onderwerp aan 'n konstante warmtelas, terwyl vierkant puls verhitting ook die temperatuur daling waarneem nadat die warmtelas verwyder is.

In vergelyking met meer populêre metodes, soos gepulseerde en geslote termografie, is die oorgangsmetodes nog nie ewe deeglik beskryf in die literatuur nie. Daar is veral belangstelling in ondersoeke na oorgangstermografie vir veselversterkte polimere en die toepassing daarvan in industrie.

Saamgesteldemateriale is geneig om defekte soos delaminasie, leemtes en inklusies te hê wat nie goed voorgestel word deur plat bodem gate nie, soos algemeen gebruik in eksperimentele werk. Hier is die gebruik van dun, kunsmatige, luggapings en Teflon® delaminasies ondersoek. 'n Beduidende verlaging in kontras en definisie is waargeneem vir dun delaminasies wat toegeskryf kan word aan die feit dat dit 'n laer termiese weerstand het as plat bodem gate.

Verdere ondersoeke na die kwalitatiewe en kwantitatiewe vermoë van die termografiese inspeksie van defektiewe onderdele voorsien deur 'n industriële vennoot is gedoen. Eksperimentele resultate het getoon dat variasies in die kern geometrie, laag oriëntasie, oppervlak en sub-oppervlak afwykings geïdentifiseer kan word. Die kleinste, waarneembare afwyking was 1 mm wyd, wat toegeskryf word aan die beperkte ruimtelike resolusie van die infrarooikamera. Die ondersoekte voorbeelde het klein radius en lae weerstand defekte getoon.

Dit is gevind dat bestaande tegnieke om defek diepte te vind deur die gebruik van inversie metodes ontoereikend is, veral wanneer 'n verwysingsdiepte nie akkuraat bepaal kan word nie.

Termografiese data word dikwels geassosieer met fyn defek kenmerke wat sterk beïnvloed word deur oneweredige verhitting en oppervlakte variasies. Dit is al gevind dat gevorderde verwerkingsmetodes die effek hiervan kan verminder. Verskeie van hierdie tegnieke, soos gevind in die literatuur, is oorweeg. Nuwe metodes, soos multiskaal retinex, bypassende filters, Markov fout kontras en aangepaste differensiële absolute kontras, word ook beskryf en ge-evalueer. Die prosesseringsmetodes is geïmplimenteer in 'n oopbron sagteware pakket en is getoets met voorbeelde uit die industrie.

Dit is getoon dat oorgangstermografie 'n sterk mededinger is in die versameling termografiese tegnieke vernaamlik as gevolg van die eenvoudige toepassing daarvan, relatief vinnige inspeksie tye en hoë termiese kontras vir gevalle waar die termiese weerstand van die defek laag is. Verder is dit moontlik om intreevlak infrarooikameras te gebruik met hierdie tegnieke. Gebaseer op toetse met kunsmatige defekte kon foute so diep as 7 mm onder die oppervlak gevind word in helder Plexiglas®. Helder Plexiglas® is nie 'n ideale materiaal vir hierdie tegnieke nie as gevolg van die materiaal se lae termiese emmisiwiteit. Defekte so diep as 5 mm kon gevind word in koolstof- en glasvesel versterkte polimere. Dit is vergelykbaar met en selfs beter as gepulseerde termografie. Die tegniek het veral beter resultate gelewer met materiale met lae diffusiwiteit, soos saamgeselde veselglas materiale.

Acknowledgements

I wish to express my sincere gratitude to Prof. Gerhard Venter and Prof. Kristiaan Schreve for their continuous guidance, exceptional feedback, their words of encouragement and immense knowledge.

I sincerely thank Mrs. Sarah Boyd and AAT Composites (Pty) Ltd, Somerset West for their willingness to help and for providing a large number of samples that was necessary for this project.

I am also grateful to the Mechanical and Mechatronic Workshop members for always being willing to help to solve my problems and for displaying a friendly attitude.

Last but not the least, I would like to thank my family: my parents for supporting me through my studies and throughout my master's degree. Without their financial support and encouragement this would have never been possible.

Contents

List of Figures

List of Tables

Nomenclature

Constants

σ Stefan-Boltzmann constant $[5.67 \times 10^8 \text{ W m}^2 \text{ K}^4]$

Acronyms

A/D	Analog-to-digital
ACE	Adaptive coherence estimator
CFRP	Carbon fibre reinforced polymer
CMF	Clutter matched filter
DAC	Differential absolute contrast
EOF	Empirical orthogonal function
FT	Fourier transform
FFT	Fast Fourier transform
IFFT	Inverse fast Fourier transform
GFRP	Glass fibre reinforced polymer
GUI	Graphical user interface
HE	Histogram equalization
IDAC	Interpolated differential absolute contrast
IRT	Infrared thermography
MEC	Markov error contrast
MSR	Multiscale retinex
NDT	Non-destructive testing
NETD	Noise equivalent temperature difference
PC	Principle component
PCT	Principle component thermography
PMMA	Polymethyl methacrylate (Plexiglas®)
PTFE	Polytetrafluoroethylene (Teflon®)
SAM	Spectral angle map
SMF	Simple matched filter
SVD	Singular value decomposition

TSR	Thermal signal reconstruction	
WT	Wavelet transform	

Variables

a_n	Polynomial coefficients	$[-]$
A	Area	$[\text{m}^2]$
A	Absorbed radiation	$[\text{J}]$
A	Amplitude	$[-]$
AR	Aspect ratio (D/z)	$[-]$
C	Contrast	$[\text{K}]$
c_p	Specific heat	$[\text{J kg}^{-1}\,\text{K}^{-1}]$
D	Defect diameter	$[\text{m}]$
e	Effusivity	$[\text{W s}^{1/2}\,\text{m}^{-2}\,\text{K}^{-1}]$
erf	Gaussian error function	$[-]$
erfc	Complementary error function	$[-]$
E	Markov error	$[\text{K}]$
f	Frequency	$[\text{Hz}]$
f_m	Modulation frequency	$[\text{Hz}]$
f_b	Blind frequency	$[\text{Hz}]$
f_s	Sampling frequency	$[\text{Hz}]$
f_c	Critical or Nyquist frequency	$[\text{Hz}]$
f_0	Center frequency	$[\text{Hz}]$
I	Current	$[\text{A}]$
I_N	Normalized image	$[-]$
Im	Imaginary values	$[-]$
ierfc	First integral of the complementary error function	$[-]$
k	Thermal conductivity	$[\text{W m}^{-1}\,\text{K}^{-1}]$
L	Sample thickness or length	$[\text{m}]$
$N_{x,y,t}$	Thermal matrix coordinates	$[-]$
P	Power	$[\text{VA}]$
q	Heat flux density	$[\text{W m}^{-2}]$
Q	Heat input	$[\text{J}]$
R	Thermal resistance	$[\text{K W}^{-1}]$
Re	Real values	$[-]$
s	Laplace variable	$[-]$
S	Scale factor	$[-]$
S_a	Sound area	$[-]$

t	Time	. . . .	[s]
t_c	Characteristic time	. . . .	[s]
T	Temperature	. . . .	[K]
T_i	Initial temperature	. . . .	[K]
T_∞	Semi-infinite body temperature	. . . .	[K]
T_{amb}	Ambient temperature	. . . .	[K]
Tr	Translation factor	. . . .	[−]
V	Voltage	. . . .	[V]
x, y	Lateral coordinate	. . . .	[m]
X	Distance from surface	. . . .	[m]
z	Depth/thickness coordinate	. . . .	[m]

Greek letters

α	Thermal diffusivity	. . . .	[m² s⁻¹]
δ_p	Penetration depth	. . . .	[m]
Δt	Time step	. . . .	[−]
ΔT	Excess temperature	. . . .	[K]
$\Delta \phi$	Phase difference	. . . .	[Rad]
ε	Emissivity	. . . .	[−]
Γ	Thermal mismatch factor	. . . .	[−]
κ	Laplace constant	. . . .	[K]
λ	Wavelength	. . . .	[m]
μ	Mean	. . . .	[m]
$\mu_{t,eff}$	Characteristic length	. . . .	[m]
∇T	Temperature gradient	. . . .	[K m⁻¹]
ω	Angular frequency	. . . .	[rad s⁻¹]
ω_0	Center angular frequency	. . . .	[rad s⁻¹]
ϕ	Phase	. . . .	[Rad]
$\phi_{i,o}$	Laplace heat flux density variables	. . . .	[−]
Φ	Heat flux (flow rate)	. . . .	[W]
Ψ	Dimensionless time	. . . .	[−]
ρ	Density	. . . .	[kg m⁻³]
ρ	Reflected radiation	. . . .	[J]
σ	Standard deviation	. . . .	[−]
τ	Transmitted radiation	. . . .	[J]
θ	Angle or direction	. . . .	[°]
$\theta_{i,o}$	Laplace surface temperature variables	. . . .	[−]

ξ Error function argument   . . . . $[-]$

Subscripts

∞	Semi-infinite half-space model
abs	Absolute contrast
acq	Total acquisition time
atm	Atmosphere
d	Defect
ij	Repeated for all pixels
k	Frequency increment
$meas$	Measured
$norm$	Normalized contrast
$pseudo$	Pseudo-frequency
$refl$	Reflected or reflections
run	Running contrast
$slab$	Slab model
std	Standard contrast
$surf$	Surface
S_a	Sound area
tot	total

Superscripts

T	Transpose

Dimensionless numbers

Fo	Fourier number

Chapter 1

Introduction

The main focus of this study is to evaluate transient thermography as a competitive non-destructive testing method alongside pulsed and lock-in thermography. Transient thermography provides a more affordable setup that includes the use of inexpensive halogen lights and the use of an entry level infrared camera. This chapter will provide the necessary background information that will put the study into context and further define the project's objectives. Finally, the chapter will conclude with an overview of the work performed.

1.1   Background

The benefits of non-destructive testing (NDT) techniques in the manufacturing industry are understood, but the various methods often require expensive equipment and technical expertise. Many times technical expertise can have an influence on the interpretation of the data. Therefore there is a need for research into simple non-destructive testing methods for both in-house and *in situ* testing of materials. Using a NDT method to evaluate materials in operation provides not only the state of material integrity but also provides an added benefit of further understanding material mechanics and behaviour.

The growing use of fiber-reinforced polymer (FRP) composites in the automotive, aeronautical, marine and defence industry has placed more interest on the investigation of these materials' performance (Ibarra-Castanedo et al., 2007). Their high strength-to-weight ratio, stiffness, durability and corrosion resistance make them a desirable material for various in-service roles. However, their success and performance relies, to a large extent, on the variability in substrate bonding, strength of inter-laminar adhesion, polymer thickness, the manufacturing process and consequently on the reliability of the quality control method. Poor quality control methods may deliver composites that are more susceptible to intrinsic defects, such as air voids, debonds and contaminates. These flaws or irregularities make them more susceptible to accelerated in-service debonds and delamination that leads to premature failure.

For this reason NDT methods are conducted to inspect and characterize the flaws within composites.

Non-destructive testing with infrared thermography (IRT) has gained more attention over the last 40 years. IRT presents favourable performance specifically towards composite material testing. IRT is inherently sensitive to near-surface anomalies (Maldague, 2001) and most FRP composites are relatively thin structures. Equally there is a shift towards automated NDT testing (Madruga et al., 2009) for batch product processing and IRT has a potential to further simplify user interaction and interpretation through images known as thermograms. There is an obvious need to find a suitable NDT method that is both affordable and simple to use.

1.2 Quality Control with NDT

For completeness, established non-destructive techniques (NDT) are briefly discussed for composite inspection before the attractive qualities of the thermography is highlighted.

1.2.1 Electromagnetic & Electric Testing

Carbon-fibre reinforced polymer composites (CFRP) can be evaluated using resistive eddy-current or resistive capacity eddy current testing (Starnes, 2002). These techniques can determine orientation of ply stacking, however it needs a conductive material with typically a high fibre-volume ratio. Moreover this method is insensitive to delaminations, material porosity and non-conductive inclusions (Starnes, 2002). The detection process assesses the composite by inducing a magnetic field over one side of the composite with a primary coil, while a receiver coil on the other side captures the changes in magnetic field.

Magnetic techniques closely resemble eddy current NDT methods and commonly evaluate ferrous materials for corrosion, pitting and crack detection. There are currently four methods that include magnetic induction, the flux-leakage method, magnetic resonance imaging (MRI) and nuclear magnetic resonance imaging (NMRI) for small lab specimens (Starnes, 2002). These methods are applicable to metallic composites, such as soft magnetic composites (SMCs) which have ferrite shavings within the epoxy resin (Stabik et al., 2010). Notably the MRI and NMRI techniques do not need magnetic materials but only small specimens can be evaluated in a controlled environment.

1.2.2 Vibration Testing

Vibration methods require intimate contact between a specimen and mechanical transducer coupled by a medium, such as oil or water. These methods

work on the propagation and reflection of sound waves applied to the specimen's surface. A defect causes a change in material density that affects the attenuation and reflection of the received wave.

Ultrasonic testing is one of the more popular vibration methods that is commonly used to detect flaws, inspect quality of welds and estimate material thickness. Many standards exist for ultrasonic NDT methods on a variety of materials. The typical advantages include the detection of minute flaws and high penetrating power that allows detection of deep flaws (Drury, 2004). Ultrasonic testing is often performed on metal alloys, though it can also be performed on wood, concrete and composites with less resolution (Brigante, 2014). Nonetheless the method requires extensive technical knowledge for the interpretation of a localized signal. The method also requires surface preparation for rough or uneven materials. The signal can be affected by material contours and generally requires a follow up with other NDT methods (Birks & Green, 1991). The inspection requires rigid clamping of the entire tested part making *in situ* testing challenging. Components that are irregular in shape or very small or thin are also difficult to inspect.

Coin-tap testing, is one of the oldest NDT methods used on composites to determine defects. It is currently the most simple and inexpensive inspection method, however the method is localized and qualitative in nature (Kim, 2008). Interpreting the location and size of an anomaly may be difficult and relies on the experience of the user.

1.2.3 Microwave Radar

Microwave radar testing observes reflected or absorbed energy when an electromagnetic beam encounters a discontinuity within a material. Discontinuities, such as voids, rebars, delaminations and porosity can be detected by the interpretation of transmitted waves (Starnes, 2002). This method is frequently used to evaluate concrete structures, bridges and pavements and has proven to detect flat inclusions and discontinuities (Nezadal et al., 2013). The technique surpasses the previous methods, by its low cost, deep penetration in non-metallic materials, two-dimensional resolution and its non-contact microwave sensor. However, to produce this two-dimensional image, tests must be repeated over equally spaced grid points on the target's surface. The proper application of microwave testing will unlikely exceed safe radiation limits, however steps should be taken to avoid over exposure (Nezadal et al., 2013).

1.2.4 Shearography

A method based on the interferometry of coherent light is shearography. The method generates two laser speckle patterns under different strain conditions, which are superimposed to extract the necessary data. These strain conditions can be induced by vibrational excitement, vacuum and thermal stressing

(Starnes, 2002). Detection of flaws and estimation of anomaly depth can be achieved with this method. Typical defects that can be detected include delaminations, debonds, cracks, porosity, corrosion and moisture ingress. However, the cost involved with the purchase of shearography equipment is high (Findeis et al., 2014).

1.2.5 Radiography

Radiography and its different forms are well understood. The technique requires penetration of high frequency electrical radiation (X-, gamma, beta or neutron rays) in a material which is then recorded on a film. More expensive systems use digital X-ray sensors. The array of radiographic methods are limited in the inspection of FRP composites, because they cannot detect interlaminar defects such as debonds and delaminations (Starnes, 2002). Detection of imperfections perpendicular to rays are impossible. However, these methods can detect structural composition, density, fibre-volume ratio, moisture content and permeability thickness of a composite. A non-radioactive method that falls under radiography is liquid dye penetrant testing. This technique exposes surface defects by the application of a dye that is viewed under electromagnetic radiation such as light or ultraviolet light. The penetrants may be toxic and require a clean and smooth surface.

1.2.6 Thermography

Thermography is a surface measurement technique that relies on an infrared camera to convert infrared energy into a measurable signal that can be displayed as an image, known as a thermogram. Internal anomalies are observed as hot or cold spots as a result of a temperature contrast between a sound (free of defects) and a defective region. Basic equipment includes an external energy source and an infrared camera. The raw signal typically exhibits subtle defect signatures and requires enhancement through the application of signal processing methods. Much research has been performed on establishing a foundation for quantitative analysis of defects in metals, polymers and concrete (Ishikaw et al., 2013). Active infrared techniques have been used to assess damage in structural aerospace parts made out of carbon fiber reinforced polymer (CFRP) (Susa et al., 2007) and glass fiber reinforced polymer (GFRP) composites (Shepard, 2007; Badghaish & Fleming, 2008). Detection and characterization of surface and subsurface debonds and delaminations are possible in thin composites (Biju et al., 2009; Theodorakeas, 2011). Impact damage was also investigated by Meola & Carlomagno (2014).

There are various energy sources for stimulating heat on a target's surface which include: vibration, heated blanket, hot air, eddy-current heating and optical illumination being the more popular method (Servais, 2006; Maldague, 2001). In a similar manner, the target specimens can be cooled down as long as

the material experiences a change in temperature. However heating methods are preferred as the heat input can be more easily controlled.

Even though other NDT methods can detect anomalies within FRP composites, the most attractive quality of thermography is the ability to scan fairly large samples quickly before focusing on areas of concern to achieve better accuracy. In addition the approach does not require physical contact with the inspected surface. The effect of geometry and surface curvature has negligible effect on the actual measurement (Shepard, 2007) but these geometries are more prone to non-uniform surface heating, which is a major problem in thermography.

1.2.7 Summary

Ideally all these methods present limitiaions and should be recognised as complimentary tools to be used in parallel with other NDT methods; but this can be economically challenging. The implementation of NDT needs to be cost-effective, accurate, easy to use and allow for *in situ* testing. Many techniques experience difficulties when it comes to anisotropy, thickness, electrical resistance, variable ultrasonic attenuation and non-magnetism (Cielo et al., 1987; Varis et al., 1994; Starnes, 2002) all of which are common in FRP structures. Most of the time user experience is the primary resource in effective quality control management.

1.3 Motivation

Optical thermography describes a method in which a material's surface is heated by a photo-thermal energy source and the surface temperature distribution is measured using an infrared camera. Optical thermography presents some key advantages in comparison with the other available technologies for composite material testing, namely:

- portable and non-contacting,

- inspect relatively large areas in a single snapshot,

- allows fast inspection rates,

- data is contained in a picture or video format which grants rapid decision making,

- data is easily stored and retrieved with any common laptop and

- the safety of personnel is guaranteed when compared to radiography (Servais, 2006).

The most widely used directions in optical thermography have been towards pulsed and lock-in thermography. Lock-in thermography requires periodic heat input to stimulate an oscillating steady-state thermal response on a target material's surface. In addition to the long inspection times required to obtain thermal stabilization, the method requires the inspection to be performed for other modulating frequencies in order to detect all flaw depths. This is because the modulating frequency of the input is linked to the probing depth of the inspection. In pulsed thermography the surface is flashed with high-power xenon lamps. These xenon lamp systems are typically more expensive than halogen flood lamps and both methods require additional power controllers and high-current power supplies.

A particular focus of the current study has been on the application of transient thermography which requires heating of the target surface by a constant heat input for a duration that lasts from one second to several minutes using halogen lamps. The heating and cooling phases are generally observed for flaws. Transient methods are expected to combine the advantages of both lock-in and pulsed thermography without sharing the drawback of long inspection times of lock-in and the need for costly light systems. The particular benefit in transient thermography compared to pulsed thermography is that the total heat-input can be easily increased by increasing the power and duration of the heating. This makes transient thermography a promising method for inspecting deeper defects than pulse thermography (Ishikawa et al., 2013). There have been few attempts made on the inspection of defects with transient thermography and the few applications have been performed without any theoretical basis (Dumoulin et al., 2011; Balageas & Roche, 2014).

Many of the thermographic studies have been performed on flat-bottom holes, which do not represent true flaws in composites. True flaws may include resin variations, inclusions, open (fully separated) or closed (contacting) delaminations. Flat-bottom holes are considered to have a large thermal resistance, while the true flaws are finite in thickness and typically exhibit significantly lower thermal resistances. The lower thermal resistance has a corresponding effect on thermal contrast and defect detectability. Therefore the effect of thermal resistance, i.e. the flaw types are compared. This will describe the limitations or transient thermography in industry.

In this study an entry-level infrared camera will be also used, which highlights the affordability of a thermography system compared to other NDT methods. Furthermore the availability of qualitative and quantitative processing software is limited and the project aims to provide an open-source software package containing current thermographic algorithms.

There has been little worked performed in South Africa and possibly Africa on thermography as a quantitative NDT method. Currently no authoritative body exists within South Africa that deals with defect characterization. Similarly, there is a lack of official standards and procedure guidelines that describe the benefits and limitations of thermography (Maierhofer et al., 2014).

1.4   Objectives

This research is aimed at evaluating detection and quantification of defects within polymethyl methacrylate (PMMA), carbon and glass FRP composites by transient thermography. Moreover specimens taken from industry that have not been properly manufactured or cured will also be evaluated without any prior knowledge of the flaws. Exact details of the material flaws will be only made available after conclusions about the materials integrity has been drawn. This will help determine the actual performance of transient thermography for industrial applications where defect knowledge is not known *a priori*. There is currently a need to:

1. broaden the scope of knowledge within South Africa,

2. explore the application of transient thermography as a competitive commercial NDT system,

3. develop an open-source processing package for thermography,

4. experimental evaluation of the performance to other IRT methods,

5. evaluate the performance of popular processing methods, and

6. assess impact of energy input on material variability, such as thermal properties, fibre content and flaw types.

1.5   Organisation

This thesis is divided into 6 main chapters and 7 appendices. In Chapter 2, active transient infrared thermography is first established before presenting a literature review on advanced signal processing methods and defect characterization methods.

Chapter 3 discusses the experimental setups and procedures on how a suitable transient heating setup was achieved. Further details about the samples and the defects are also provided. Subsequently, image processing algorithms are introduced in Chapter 4. This will familiarize the reader with favourable techniques available for transient thermography before discussing their effects in Chapter 5. These algorithms are included in an open-source application available at http://tinyurl.com/ptu25n7. Lastly in Chapter 6, the preceding chapters and experimental results are discussed before conclusions and recommendations are proposed.

Chapter 2

Nondestructive Testing With Thermography

2.1 Terminology

Throughout this thesis the term *target specimen* refers to the material or sample under investigation. The material has its largest surface area normal to the camera. Lateral defects are considered to be parallel to this area and the defect depth is the perpendicular distance from the inspection surface. The terms debond, delamination, defect, flaw and anomaly are all sources of change of thermal resistances and can be used interchangeably throughout this thesis. However *defects* can be considered as deliberate inclusions or flat bottom holes of known dimensions, where as *anomalies* and *flaws* refer to unusual changes in thermal resistance being present in samples with unknown defect history. Lastly, the term *delamination* is the local debond of plies that can either be separated or in contact with the adjacent laminate plies.

2.2 Fundamentals of Thermography

Non-destructive testing with active infrared thermography requires the target material's surface to be subjected to a thermal stimulus. The rise in the surface temperature causes heat to diffuse towards the material's cooler interior and can be visualized as successive wavefronts moving through the material over time. When these wavefronts encounter a local change in thermal properties, such as a delamination, the wavefront alternatively slows down or speeds up depending on the thermal properties of the discontinuity. In the event of the thermal wave slowing down, the region will experience increased heating, or in the other case of the thermal wave speeding up, the region will dissipate heat faster towards the rear face of the material. The internal interference produced by successive thermal fronts at this region will reverberate towards the surface over time. The extent of this is different for a non-defective and

8

defective region and will induce a thermal contrast between these regions. The delamination can now be observed as either a hot or cold spot. This thermal contrast provides the ability to detect subsurface anomalies provided that the thermal properties of the anomalies are different to the bulk thermal properties of the host material.

2.2.1   Common Thermography Scenarios

Several preferred thermographic scenarios have emerged earning them their characteristic names such as lock-in, pulsed and transient thermography and they differ in the way they deliver energy. For example, lock-in thermography requires a square or sinusoidal heat pulse, pulsed thermography requires an instantaneous heat pulse and transient requires a long pulse of energy. Each method can be performed with different sources of thermal excitation as mention in Chapter 1.

Preferred inspection scenarios rely mostly on optical illumination demonstrating its effective role in active thermography. Optical illumination is chosen in this project for the following advantages: fast inspection rate; non-contact observations; easily controlled through common line voltage, power supplies or batteries; the light-bulbs are replaceable at a fraction of the cost of other lighting and the variety of bulb shapes allow design of heating apparatus for complex and curved shapes. However there are problems associated with optical heating. An inherent problem is deploying a fast and uniform heat over the entire surface of the sample (Ibarra-Castanedo et al., 2013). Non-uniform heating and thermal losses introduce spurious contrasts that affect defect detectability and characterization in the raw thermogram.

Effects that are not a result of optical heating but rather material properties include surface emissivity. Emissivity of the target material affects both the absorption of energy and the strength of the signal that reaches the infrared camera. Local variation in emissivity has a noticeable effect in the amplitude of the thermal signal. The signal being measure can be strongly contaminated with ambient infrared reflections especially for low emissivity materials.

Appendix A discusses the theory behind optical heating and the photothermal properties that need to be considered when using an infrared camera.

2.2.2   Qualitative Versus Quantitative

The direction of thermography has been to detect and quantify defect parameters in composites since changes in the composite physical structure have a recognized degradation in the composite's performance and expected lifetime. Thermography is naturally qualitative enabling the detection of subsurface anomalies. However thermal diffusion effects alter the lateral size of the anomaly and the actual size can not be correctly evaluated. In addition,

knowing the depth and thickness of the anomaly can provide more critical information on the extent of the damage.

This had led to the application of two thermographic approaches: active and passive. For the passive approach, the specimen is itself the source of the temperature difference and usually involves steady state thermal conditions, i.e. external excitation is not employed. Passive approaches can include detection of water ingress (Laurens et al. 2003, Ibarra-Castanedo et al., 2007) in sandwich-composites and tensile fatigue (Steinberger et al., 2006) in FRP composite plies. This method can be applied to any mechanical application that will undergo localised heating in stress regions or generate heat during operation.

Active thermography on the other hand requires thermal excitation. Active thermography requires surface temperature measurement as a function of time. Only through time-resolved thermography can the depth and thickness of a flaw be measured (Maldague, 2001; Sultan et al., 2012). Naturally active thermography provides both qualitative and quantitative measures to be able to fully describe the presence of anomalies.

2.2.3 Reflection Versus Transmission

Each thermographic scenario can be implemented in two common modes, namely reflection and transmission. In the reflection mode, heat is delivered to the same side from which the thermal response is measured, whereas the transmissive mode relies on observing the thermal response from the opposite side to that of the heated surface.

Reflection mode allows the empirical measurement of defect depth as a function of time, which is lost in the transmission mode (Maldague, 2001). This is because the thermal waves will travel the same distance, or time, to the back of the sample in the transmission mode regardless of the thermal waves being attenuated by the presence of a defect.

The reflection mode is suitable for *in situ* inspection as only one side of the specimen is needed. It is best suited for near-surface defects or inspection of coating thickness (Vavilov et al., 1993). The transmission mode is only preferred when inspecting deeper defects in thicker layered composites and for diffusivity measurement techniques (Parker et al., 1961). In addition, this mode is known to produce a low thermal resolution of defects.

2.3 Heat Flow Theory

The application of thermography is straightforward. However the main issue in thermography is that the heat flow inside a solid is complex. The complexity originates from molecular composition of the material that can be described through macroscale thermal properties, such as thermal conductivity, density,

effusivity, porosity and specific heat. In order to characterize defects the effects of conduction need to be understood.

2.3.1 Thermal Conduction

Heat flow is governed by a temperature difference with heat moving from a high to low temperature region until thermal equilibrium is reached. The rate at which heat flows in a solid body is often expressed by the material's thermal conduction. Fourier's law of conduction defines the steady-state heat flux in an arbitrary direction r as (Fourier, 1952)

$$\Phi = -kA\nabla T_r \ , \tag{2.3.1}$$

where k is the thermal conductivity, A is the cross-sectional area normal to heat flow and $\nabla T = \partial T / \partial r$ defines the temperature gradient. The negative sign describes the flow is opposite to the direction of the gradient.

Active thermography is however a non-stationary process that relies on transient heating and cooling. Transient flow through a solid is a complex three-dimensional problem that can be described by Fourier's heat diffusion equation, which combines the law of conservation of energy with Fourier's law, Equation 2.3.1. The spatial and temporal distribution of heat can be modelled as

$$\frac{\partial^2 T}{\partial x^2} + \frac{\partial^2 T}{\partial y^2} + \frac{\partial^2 T}{\partial z^2} = \nabla^2 T = \frac{1}{\alpha}\frac{\partial T}{\partial t} - \frac{Q}{k} \ , \tag{2.3.2}$$

where all thermophysical properties are assumed constant, T is the temperature at time t and $Q > 0$ represents internal heat generation or heat loss $Q < 0$. The Laplacian operator for a Cartesian coordinate system is defined by ∇ where principal axes x and y forms a plane parallel to heated surface and z describing the direction normal to this surface, or alternatively seen as the thickness or defect depth direction. The thermal diffusivity is α:

$$\alpha = \frac{k}{\rho c_p} \ , \tag{2.3.3}$$

where ρ is the density and c_p is specific heat for constant pressure, which together describes the volumetric heat capacity. The thermal diffusivity describes the speed of material's thermal response to a change in temperature and is a product of steady state conduction k.

The right hand-side of Equation 2.3.2 describes the transient transport process resulting in a time-rate of change of internal energy produced by unbalanced heat entering or leaving the representative volume while the left hand-side describes the conductive (steady-state) change in temperature.

2.3.2 Characteristic Length

In order to visualize the behaviour of heat flow within a material and the non-stationary heat conduction described in Equation 2.3.2, it is necessary to evaluate the thermal behaviour of a material experiencing a single momentary impulse of energy. Solving the three-dimensional Fourier equation for a Dirac delta function is difficult since an analytical solution does not exist for a non-linear partial differential equation. However the use of the one-dimensional model allows one to simplify Equation 2.3.2. The one-dimensional Fourier heat equation for conduction in a planar medium with constant thermal properties and no heat generation is expressed as

$$\frac{\partial^2 T(z,t)}{\partial z^2} = \frac{1}{\alpha} \frac{\partial T(z,t)}{\partial t} \ , \tag{2.3.4}$$

where z is the direction normal to the planar surface at time t. This model assumes the diffusion normal to the surface to be significantly greater than the lateral diffusion with no thermal loss from sample surfaces.

Now Equation 2.3.4 can be solved for a semi-infinite homogeneous medium undergoing a Dirac delta impulse at the surface $z = 0$ from an initial temperature T_{amb} to T_i producing a temperature response (Carlsaw & Jaeger, 1959)

$$T(z,t)_\infty = T_i + (T_{amb} - T_i) \ \text{erf}\left(\frac{z}{2\sqrt{\alpha t}}\right), \tag{2.3.5}$$

where erf is the Gaussian error function. By differentiation of the temperature response, the heat flux density $q = \Phi/A$ can be estimated as (Marin, 2010)

$$q_\infty = \frac{(T_i - T_{amb})}{e\sqrt{\pi t}} \ \exp\left(-\frac{z^2}{\mu_t^2}\right), \tag{2.3.6}$$

where $e = \sqrt{k\rho c_p}$ is the thermal effusivity and the heat flow is described as a Gaussian decay of energy in time with a characteristic width of

$$\mu_t = 2\sqrt{\alpha t} \tag{2.3.7}$$

This equation actually provides a notable feature in visualizing the temperature front as travelling a distance in time t before being attenuated by a factor of 1/exp when diffusing one diffusion length from the heated surface $(x = 0)$. In other words it describes the heat flux amplitude at different depths in the material. This definition is regarded as the characteristic length μ_t or effective thermal diffusion length that can further describe three dimensional diffusion over a sphere of radius μ_{eff} .

Thermography measurements using an infrared camera represents only heat released within the thermal diffusion length of the sample surface and the fact that the thermal front being a critically damped amplitude as time goes on makes thermography only suitable for near surface defects and thin samples.

This could be another possible reason why interest is placed on inspecting composites with thermography.

2.3.3 Characteristic Time

The time needed for heat to diffuse through a conductor of characteristic length L, is known as the characteristic time

$$t_c \sim \frac{L^2}{\alpha} \; . \tag{2.3.8}$$

Cielo et al. (1987) observed a similar relationship relating the square of depth and diffusivity for emerging defects. Later a observation time describing a defect at depth L below the measured surface was theoretically proven and experimentally validated in defining the observation time of a defect (Karbhari, 2013; Marin, 2010; Sun, 2006; Ringermacher, 1998). The ratio also describes a well-known dimensionless number known as the Fourier number defined for transient heat conduction.

For most composite solids having a thermal diffusivity $\alpha \sim 10^{-5}$ m/s and characteristic length $L \sim 10^{-3}$ m, the diffusion time $t_c = L^2/\alpha$ is estimated around 10^{-1} s. The significance of this characteristic time allows the definition of an appropriate acquisition time. This time describes a rough estimate of time when heat that has reached the back-wall is displayed on the surface of specimen in reflection mode. This characteristic time is reasonably short compared to the average time of a thermal inspection and the times of deeper defects emerging. The reason why deeper defects appear much later is the result of limited camera sensitivity and the amount of excitation applied to the surface. The surface will still experience changes from subsurface diffusion at early times regardless of a limited ability to measure it (Shepard et al., 2014). To conclude the time heat travels to the back surface is unaffected by input energy, but an increase in input energy is expected to increase defect contrast.

This relationship is clearly illustrated by the solution of a one dimensional slab of finite thickness exposed to an instantaneous heat pulse. Figure 2.1 illustrates the change in surface temperature for the slab model of different thickness L in the double logarithmic domain. The surface response is seen to follow a constant decay typical of the one dimensional semi-infinite model before reaching a thermal steady state originating from the back-wall reflections. Two well-defined asymptotic curves are observed for each thickness L that intersect at a time $t' = L^2/\alpha\pi$ which connects a measurable point in the surface thermal response to a particular slab thickness and corresponds to Equation 2.3.8.

Consequently if the diffusivity is known plate thickness can be "quite precisely" determined and the reverse is also true when thickness is known (Ringermacher et al., 1998). Therefore a defect at a set depth will cause termination of
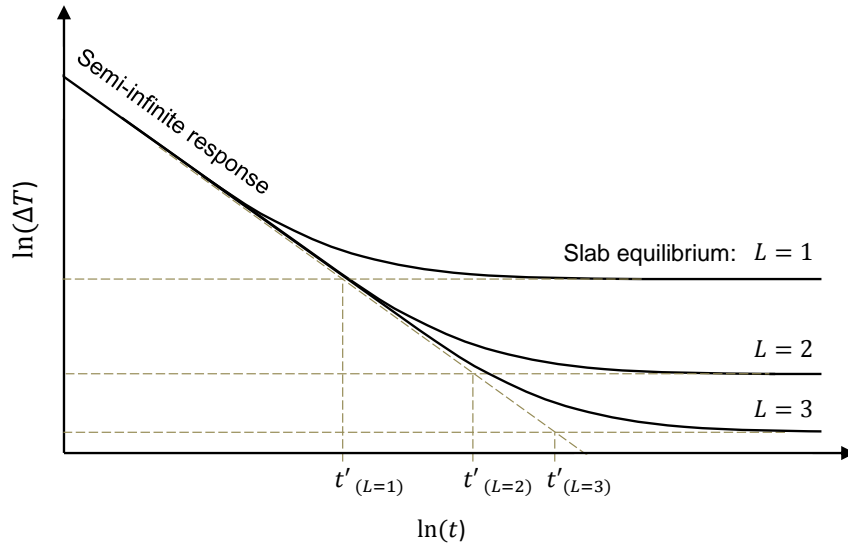
Figure 2.1: Response of semi-infinite and slab model to Dirac delta heating showing the breakpoint for three different thickness values L (adapted from Karbhari, 2013)

the one-dimensional thermal response in much the same way as the back-wall does. Although L is by strict definition the slab thickness which describes a defect having a infinitely large adiabatic planar surface with a infinitely large thermal resistance. In reality a defect or delamination may be finite in size and have a relatively low thermal resistance. The relationship nevertheless provides the definition, that for a constant thermal diffusivity, depth is related to a characteristic time of observation using thermography in reflection.

The characteristic time for defect depth, $t_c \sim z^2/\alpha$, indicates that only at longer times will deeper defects emerge on the surface and for a lower diffusivity the time is further delayed. At these longer times, three-dimensional diffusion will take preference reducing the thermal contrast of these deeper defects independent of diameter. In fact the thermal contrast C is proportional to the cube of depth (Allport & McHugh, 1988):

$$C \sim \frac{1}{z^3} \tag{2.3.9}$$

This observation is valid for homogeneous isotropic material and, in the case of anisotropic materials, the depth probing is even more constrained.

2.3.4   Significance of One-Dimensional Model

The one-dimensional Fourier equation is considered for its simplicity and has allowed further understanding of the heat flow phenomenon. It has provided relationships through the thermal diffusion length and characteristic thermal

times and more importantly been applied to many image processing algorithms. The first use of the one-dimensional model was by Parker et al. (1961) to determine the thermal diffusivity for a plate of uniform thickness under ideal flash thermography conditions. Parker et al. showed that by knowing the thickness of the sample and determining the half-maximum rise time of the back-wall temperature response the material's diffusivity could be determined. This suggests that depth is a function of both time and material diffusivity. Another method to calculated diffusivity was proposed by Cernuschi et al. (2002) that uses the flash method in reflection mode.

Shepard et al. (2014) confirmed the material's thermal response follows the one-dimension model reasonably well for a homogeneous material but deviates from this model at times when the heat flow reaches internal thermal heterogeneities. The model still holds reasonably well for shallow defects in anisotropic materials and provides good results for homogeneous materials (Susa et al., 2006).

2.4   Lateral Diffusion

The one-dimensional model describes heat flow of a homogeneous material that is subjected to a uniformly distributed heat flux and assumes one-dimensional diffusion normal to the surface. This is unfortunately not the case for real materials, especially for composite materials, that are prone to three-dimensional diffusion. Thermal diffusion perpendicular to the heated surface provides the ability to inspect internal defects however diffusion parallel to this surface is described as lateral diffusion and is an inherent and unavoidable problem in thermography. Lateral diffusion is accelerated by non-uniform heating and local changes in the geometric shape and thickness of a material (López et al., 2014b). Even for a perfect distribution of surface heat, lateral diffusion will eventually occur when the thermal wavefronts experience a change in thermal resistance and instead of being perfectly reflected towards the surface tend to spread laterally over the face of the defect. Lateral diffusion is increased for material anisotropy with higher thermal conductivity in the fibre directions (Varis et al., 1995).

If one recalls the thermal diffusion length $\mu_{eff} = 2\sqrt{\alpha t}$ which describes heat flow in three-dimensional space from a point source, one can see that lateral diffusion will increase with time. Considering that there is an obvious connection between time of emerging defects to their depth, shallow defects will emerge at early times and will be less affected by lateral diffusion. While for deeper defects that appear at later times, the diffusion in all directions is significant.

In addition lateral diffusion is influenced by volumetric heating and edge effects caused by defects of finite diameter and thickness (Saintey & Almond, 1995). For a large and shallow sub-surface defect, the heat is trapped in

a small volume above the defect causing the volume's temperature to elevate rapidly, which produces a high surface contrast. However the high temperature gradient between the trapped heat and the surrounding sound area produces high diffusion rates from the center of the defect towards the defect edge. The increase in lateral heat flow causes the surface to experience a rapid reduction in defect size and rounding of the temperature profile on the surface seen in Figure 2.2. This process is known as the edge-effect. For a deeper defect the volume above the defect is much larger and the material remains cooler, producing a smaller thermal contrast. Adding more heat into the control volume will increase the thermal contrast over time but the lateral diffusion effects become significant.
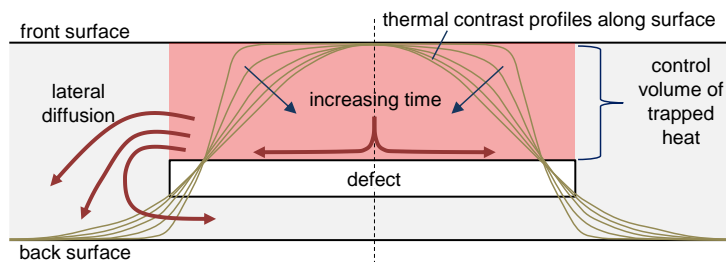
Figure 2.2: The consequence of edge effects and lateral diffusion on the thermal contrast of defects

The thickness of the defect affects the thermal resistance and amount of heat trapped. For relatively thick defects, in the case of flat-bottom holes, the contrast is high and the edge effects only cause reduction in thermal contrast size. For relatively thinner defects, specifically when the defect diameter is small, the edge effects have a chance to meet up on the back-side of the defect and reduce the heat trapped above the defect, which further reduces the contrast.

Because there is a combined effect of defect depth, thickness and lateral diameter, defects should be rather assessed on their diameter-to-depth ratio under the surface known as the defect's aspect ratio:

$$\text{AR} = \frac{D}{z}, \tag{2.4.1}$$

where a large ratio is less likely to be affected by lateral diffusion and blurring. An empirical rule of thumb for pulsed thermography says that the radius of the smallest detectable defect should have an aspect ratio AR of at least two (Madague, 2000, Omar et al., 2005, Shepard, 2007). As AR approaches unity or less, the thermal contrast between the sound and defect area is often at a level comparable to the noise level of the infrared camera (Karbhari, 2013). Therefore the defects that can be detected accurately are limited to large and shallow defects.

2.5   Thermal Effusivity

The thermal effusivity is defined by $e = \sqrt{k\rho c_p}$ and expresses the rate a material can absorb or release heat to another material in contact. Since the interface is governed by two materials with their own thermal effusivity a thermal mismatch factor, or reflection coefficient, is defined (Karbhari, 2013)

$$\Gamma_{host/inclusion} = \frac{e_{host} - e_{inclusion}}{e_{host} + e_{inclusion}}, \qquad \text{where } -1 \leq \Gamma \leq 1, \qquad (2.5.1)$$

which describes the variation in thermal properties of an inclusion (defect or delamination) at an interface within the host material. A $|\Gamma|$ value close to one describes a large difference in thermal properties of the materials in contact and the net flow of heat is limited by one of the materials. The limiting material can be regarded as having a thermal resistance. A high thermal resistance encourages the reflection of heat back towards the surface producing a relatively higher contrast than for a interface allowing heat to pass through unreflected. Consequently when $\Gamma = 0$, the inclusion is perfectly matched, or thermally transparent, with the bulk material and little or no contrast will be observable on the target surface (Marin, 2010). Therefore the thermal mismatch factor is an indication if inclusions or defects will become observable in thermography. One must note that effusivity is not the strict definition of thermal resistance but merely an indication of it. This has a practical implication on the type of inclusion used to artificially replicate a delamination.

2.6   Transient Thermography: Step and Square-pulse Thermography

Transient thermography methods include step and square pulsed thermography. For both these methods the surface of the material is heated and simultaneously recorded for a duration from one second to several minutes. Square pulse thermography requires the additional recording of the subsequent cooling phase once the heat has been removed. The cooling phase is recognised to allow deeper defects to gain higher contrast. Usamentiaga et al. (2012) noted that the cooling phase shows slightly better results than the heating phase, even though shallow defects begin to appear during the heating phase.

Some applications of step heating include measuring surface coating thickness and thermal diffusivity of multi-layered coatings (Maclachlan Spicer et al., 1998). Badghaish & Fleming (2008) recognised that material thickness estimations using a characteristic time can be extended to evaluate depth of flat-bottom holes in glass fibre composites for defect depth estimation. An

empirical relationship using the characteristic time was defined for thickness estimations of zirconia coatings (Maclachlan Spicer et al., 1991).

There has been no preferred choice between the two transient methods and the advantages of step and square pulse heating have not been fully described in literature. The application of the many different processing algorithms has not been evaluated on transient methods. Only recently, has a theoretical basis emerged for step heating (Balageas & Roche, 2014). From the theoretical studies step thermography has a potential to observe deeper defects (Balageas & Roche, 2014). Since square pulse thermography shares the same heating regime as step thermography the theoretical background is the same.

The use of the one-dimensional heat equation was shown to be beneficial in understanding heat flow and characterizing defect parameters. The one-dimensional heat transfer problem is given in Figure 2.3 for a infinitely large slab of finite thickness L experiencing a constant heat flux and the back-wall is assumed adiabatic. The increase in temperature through the thickness z is given as (Carlsaw & Jaeger, 1959)

$$T(z,t) = \frac{2\sqrt{\alpha t}Q}{k} \sum_{n=0}^{\infty} \left[\text{ierfc}\left(\frac{L(1+2n)-z}{2\sqrt{\alpha t}} \right) + \text{ierfc}\left(\frac{L(1+2n)+z}{2\sqrt{\alpha t}} \right) \right], \qquad (2.6.1)$$

where the surface temperature is attained by substituting $z = L$:

$$T(L,t) = \frac{2\sqrt{\alpha t}Q}{k\sqrt{\pi}} \left[1 + \sqrt{\pi} \sum_{n=1}^{\infty} 2 \, \text{ierfc} \frac{nL}{\sqrt{\alpha t}} \right], \qquad (2.6.2)$$

and where *ierfc* is the first integral of the complementary error function defined as

$$\text{ierfc}(\xi) = \frac{1}{\sqrt{\pi}} \exp^{-\xi^2} - \xi \cdot \text{erfc}(\xi) . \qquad (2.6.3)$$

At sufficiently small times for a given thickness L and for composite materials having a low diffusivity, the *ierfc* is large and the summation term becomes negligible as the *ierfc* approaches zero for a large argument, $\xi \sim \frac{L}{\sqrt{\alpha t}} \to \infty$. Therefore the front face temperature response at early times is equivalent to the semi-infinite response:

$$T(t)_{\infty} = \frac{2Q}{k} (\frac{\alpha t}{\pi})^{1/2}, \qquad (2.6.4)$$

where the change in temperature of the semi-infinite solution follows a constant slope of $+0.5$ in a homogeneous material and is remarkably analogous to well-defined -0.5 slope in pulsed thermography (Balageas & Roche, 2014). When the heat has reached the back-wall, a familiar breakpoint can be observed when the surface response deviates away from the semi-infinite behaviour of the semi-infinite model, seen in Figure 2.4. Again the time of the breakpoint

is characteristic of the thickness of the plate and the time of the breakout point will be delayed for increased slab thickness. In practice the asymptotic intersection is not easily measurable due to three-dimensional material effects and non-adiabatic behaviour as the plate seldom reaches a constant steady state temperature.
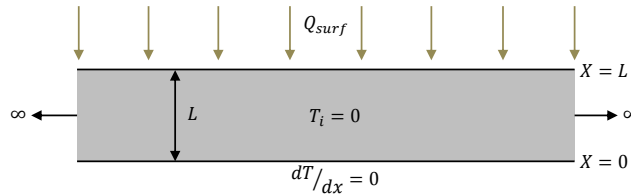
Figure 2.3: Step heating applied to one-dimensional slab of finite thickness L
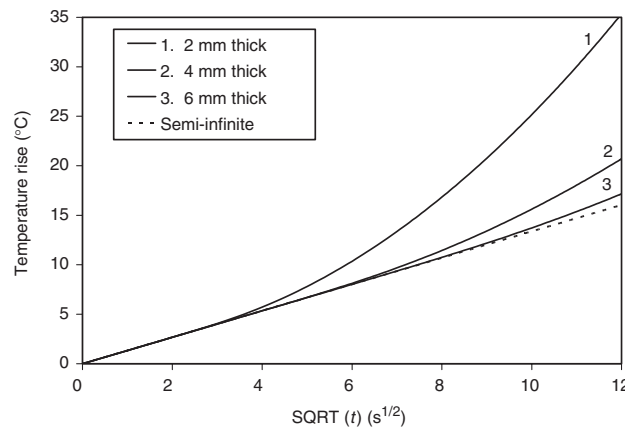
Figure 2.4: The surface temperature for an one-dimensional slab of different finite thickness L (Badghaish & Fleming, 2008)

No analytical model was found for square-pulse heating, however the heating phase is identical to the thermal response of step heating and the decay similar to pulsed thermography. Even though a sharp change is observed from the heating to the cooling phase, a smooth continuous contrast will still exist when one normalizes the thermal response with that of a sound zone experiencing the same heating and cooling phases.

2.7   Review of Signal Processing Methods

There is a need for processing methods to help aid in the identification and characterization of defect parameters as the raw signal contains subtle signatures masked by optical irregularities. Without a suitable processing method

only shallow defects with high thermal resistance are generally observable in the raw signal. Processing algorithms applied to thermographic data are reviewed below. These processing methods have originated from their application in either lock-in or pulse thermography.

2.7.1 Noise Removal

Degradation in the signal is result of optical, electronic, heating and ambient noise. Noise removal can be performed using median filtering and Gaussian low-pass filtering as they are less prone to diffuse or blur defect edges (Ibarra-Castanedo et al. 2004; Maldague, 2001; Venegas et al., 2012). Other methods include polynomial fitting (Shepard, 2007), least-squares fitting of a theoretical model (Sun, 2003), one-dimensional wavelet denoising and through the application of smoothing filter, such as Savitzky-Golay filter (Savitzky & Golay, 1964).

2.7.2 Thermal Contrast Techniques

Contrast methods improve the thermal contrast between defective and non-defective areas while maintaining relevant temporal information. The most basic form of contrast enhancement technique is using pseudocolors or false colours that can be applied to a grayscale image.

Maldague (2001) defines four image contrast definitions such as absolute, running, normalized and standard contrast. Absolute contrast is the most basic form of subtracting a non-defective or sound pixel S_a from all other pixels. This method performed poorly on samples that were susceptible to non-uniform heating and surface variability (emissivity, reflections, and cleanliness) effects which lead to erratic contrasts (Susa et al., 2007). Running, normalized and standard contrast methods were modifications to the absolute contrast developed to reduce the effect of local inhomogeneities. Most studies performed in determining defect depth has been based on the use of these contrast methods.

The main obstacle in the proper use of these image contrast definitions is the selection of a non-defective region S_a by a user. The selection can include a single pixel's time history or the average of a group of pixels. Even when the selection of S_a is straightforward, there is a considerable variation in the observed results for a different choice of S_a (Martin et al., 2003). The selection of the sound zone determines the threshold for all other pixels, even those that experience lower variability.

The differential absolute contrast (DAC) method (González et al., 2004a) eliminated the need for the selection of a sound zone. However a reference frame needs to be chosen that contains no defects after the last instant of heat. The method assumes the thermal signal follows a one-dimensional decay after an instantaneous heat pulse. Any deviations from this theoretical model

will be damped and the impact of non-uniform heating, emissivity variations and surface complex or non-planar geometry and emissivities are efficiently removed (Benítez, 2008). The performance of DAC has shown to be successful on Teflon® inserts in CFRP thermography (Klein et al., 2008) for short times. At later times the one-dimensional model collapses as the thermal response of the material is affected by lateral diffusion effects.

To extend the validity of DAC to later times a modified version, named the interpolated differential absolute contrast (IDAC) was introduced (González et al., 2004b; Benítez et al., 2006). The IDAC is based on the thermal quadrupoles theory using the Laplace transform (Maillet et al., 2000), which is a technique of solving the one-dimensional heat problem as a set of linear equations in the Laplace space. The Laplace domain provides an explicit form of the system equations where a direct calculation of the thermal response can be solved or, alternatively, used to estimate the system parameters based on the thermal response. IDAC derives the solution of the one-dimensional heat problem in a transformed Laplace space after defining material thickness and thermal diffusivity as input parameters. Although not always known, a user can interactively adjust input values while trying to match a sound region. This IDAC method preserves the performance of DAC at short times and helps extend the validity to later times, i.e. deeper depths.

Klein et al. (2008) further improved the heat transfer model of IDAC by including additional thermal loss parameters. At later times the IDAC and modified IDAC contrast is greatly improved which can be seen in Figure 2.5 on a CRFP plate slab.
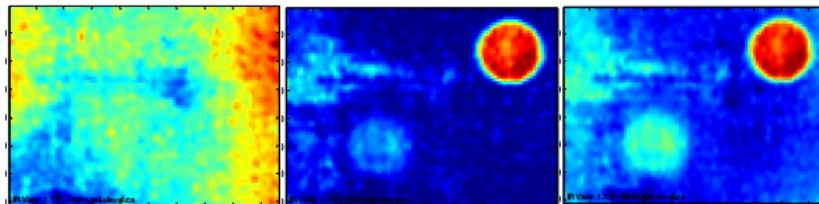
Figure 2.5: Maximum contrast images of DAC, IDAC and modified IDAC with thermal losses (Ibarra-Castanedo et al., 2015)

The DAC methods may perform reasonably well for shallow defects in composites but they rely on the one-dimensional model of heat transfer to deal with a three-dimensional heat transfer problem. Many of the algorithms presented in literature do not account for lateral diffusion of heat. The effects of lateral diffusion along with non-uniform heating limit the detection of deeper defects. Restrepo & Loaiza (2012) considered using a three-dimensional discrete Fourier heat model that relies on a spatial filtering mask rather than performing temperature estimation in the three Cartesian directions. This use

of a convolution filter speeds up the algorithm and is seen as an appropriate method for multiple frame processing. The mask would estimate the next temperature on each pixel according to the current temperature of that pixel and its four-neighbours. This method is known as finite differences thermal contrast (FDTC) and does not need the selection of a sound area or referenced frame as in the former contrast techniques and DAC. The method was applied to an numerical data set of a CRFP model that was contaminated with irregular effects like noise and non-uniform heating effects (Restrepo & Loaiza, 2012). The method demonstrated that the thermal profiles of sound regions remained quite flat removing the irregularities, but an vast improvement was observed in the absence of noise and optical effects in the artificial signal.

Techniques that account for lateral diffusion include inverse scattering techniques (Favro et al., 1994; Crowther et al., 1993) and point spread functions (Omar et al., 2005) that optimize the edge response in the image by inverting the blur effect produced by diffusion at later times. Pulse-echo thermal wave imaging considered by Han et al. (1996) is not an processing method but describes analytical formulae to represent three-dimensional thermal wave diffraction of circular, planar subsurface defects in anisotropic material. This analytical formulae has performed well against experimental data having similar contrast peaks for varying lateral sizes and depths of flat-bottom holes. Fitting data to this model may seem a more appropriate approach in making this method more useful, but unfortunately this method relies on knowing the presence of defects before comparison.

Not to be confused with the normalized contrast method, normalization proposed by Zalameda et al. (2003) requiring the user to calculate each pixel's average of the total images divided by the average set of images where the zone of interest is observed in the temperature data. This is of course localised to one particular anomaly and requires prior knowledge of the anomaly. As well as requires the user to find the relevant images from a substantially large dataset.

2.7.3 Spatial Contrast Techniques

Spatial contrast techniques enhance the dynamic range of the image and are qualitative by helping a user visualize internal anomalies. Correlation methods measure the statistical relationship between two similar images or temperature profiles (Klein et al., 2008a; Sun et al., 2007). This method can produce an image showing the differences between a defect free sample to a similar sample that is suspected of having internal deficiencies from the manufacturing process. Classical image enhancement methods include image normalization and histogram equalization methods (Gonzalez & Wood, 2010). Histogram equalization methods have been used in infrared image enhancement for military purposes (Bai et al., 2011).

Other methods like K-means clustering has been useful in unsupervised learning machines for the mutli-threshold segmentation of the flaws (Abdel-Qader et al., 2008). Due to the presence of non-uniformities and blurry edges of the data, Usamentiaga et al. (2014) proposed a group of algorithms called active contours (Kass et al., 1988) which are able to perform segmentation in images with intensity heterogeneities. Likewise the use of Sobel and Canny filters are common methods to defect defect edges. These methods are typically straightforward once a good visual image is obtained.

2.7.4 Thermal Signal Reconstruction

Thermal signal reconstruction (TSR) is a curve fitting method proposed for flash thermography, and later for step heating (Balageas & Roche, 2014), to increase the spatial and temporal resolution (Shepard et al., 2003; Shepard, 2007). A least squares fit of a m-degree polynomial is applied to the logarithmic time sequence of each pixel on the assumption that the temperature for non-defective pixels should follow the linear decay curve given by the one-dimensional solution. Therefore any deviations from linearity can be seen to be amplified.

The entire thermal sequence can be reduced to a set of $m + 1$ coefficient images. The optimal choice of polynomial order depends on the purpose of the fit according to Roche & Balageas (2014). For pulsed thermography, a polynomial order of $4 - 8$ is used for defect enhancement while an order of 11 was used for time analysis (Shepard et al., 2003; Klein et al., 2010; Roemer et al., 2013). Numerical simulations and experimental trials performed by Dumoulin et al. (2011) agreed with the choice of polynomial order. For step heating, a 7th order polynomial was used for the temperature response and a 10th order to fit the thermal contrast of defects (Balageas & Roche, 2014). High order polynomials are generally avoided as they are more prone to oscillating effects beyond the sampled data. However there is no need to determine a trend or extrapolate thermographic data since only the fitted data is of concern, therefore the use of a high polynomial is an acceptable choice.

The classical application of TSR was used in visualizing and estimating defect depth using the best derivative images. These derivative images were selected based on their maximum temperature contrast at a particular depth of a defect. A popular advantage in pulsed thermography is that the time of maximum contrast in the second derivative corresponds to the breakpoint associated with characteristic length in pulsed thermography.

Noise is a typical trait in thermographic data, especially for low emissivity target specimens, and the TSR method has become a popular method with many derived extensions exploiting the noiseless properties to characterize defects. The various methods can be seen in Figure 2.6 and include the calculation of first and second time derivatives (Shepard et al., 2003b), a unique colour depth map using coefficient data (Shepard, 2007), visualization

of defects through coefficient images (Balageas et al., 2013), creating a unique depth composite image based on the coefficients (Roche et al., 2014) and finding the first and second derivative using the fingerprint transform (Shepard, 2014).

The depth composite image and the fingerprint transform are of particular interest since they both help speed-up depth and lateral size characterization via a single image as well as simplifying the data of the large thermal sequences. Firstly, the depth composite image requires some user input to select three best coefficient images that display as many of the detected defects. Then the three coefficients are normalized and respectively defined as the red, green and blue channels of an RGB colour image. The combination of the different channel intensities will essentially create a depth map which can express the depth information through a colour table being a linear summation of the three channels. The colour table is calibrated accordingly by inversion methods.

The fingerprint transform method produces a 'fingerprint' of the entire sequence and represents it as one image. The image is constructed by combining the histograms of each image in the sequence so that the x-axis represents time or frame of histogram and the y-axis describes the first or second derivative intensity values . The image information can then be numerically compared using cross-correlation tools to other fingerprint images. The correlation of two of these images is interestingly translation and rotation invariant.
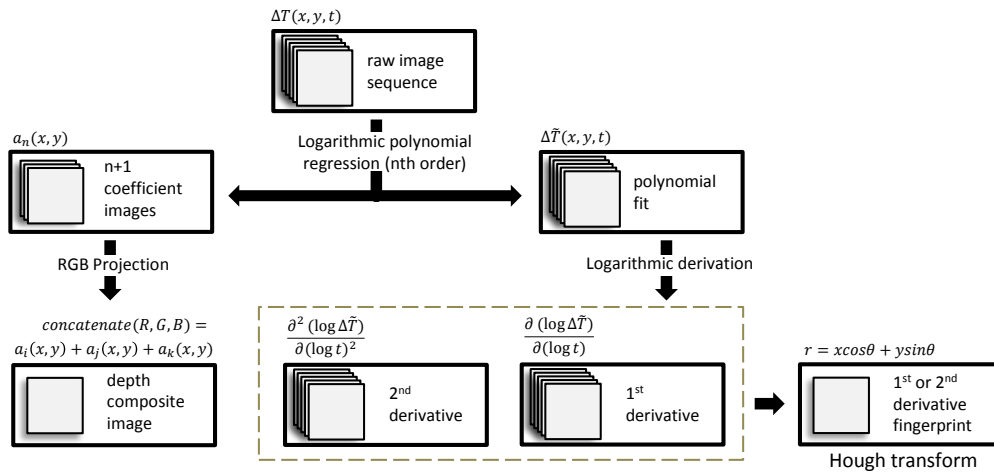
Figure 2.6: Extensions of the thermal reconstruction method (TSR)

2.7.5   Signal Transforms

Signal transforms rely on transforming the thermal data from its time-space to another domain space. A notable transform is the Fourier transform that

decomposes the one-dimensional signal as a set of sinusoidal waves of increasing frequency in the frequency-space. Due to the sinusoidal fidelity property of sinusoidal waves that is not observed for any other waveform, an input waveform will produce an output waveform of the same frequency that only differs in amplitude and phase. Based on the fact that depth can be obtained from the phase and amplitude images in lock-in thermography, the idea was introduced for non-periodic signals of pulse thermography. The benefits of phase images are known to be less affected by non-uniform heating, emissivity variations and ambient reflections. The Fourier transform method applied to pulsed thermography is often described as pulsed phase thermography (PPT) (Maldague & Marinetti, 1996).

The wavelet transform (WT) is proposed as an alternative method to FT to better describe non-periodic transient functions (Zauner et al., 2010). Contrary to the FT method producing a frequency-space, the WT produces a scale-time space that preserves time information. This is of interest when estimating depth as a function of characteristic time. The scale can be associated as a frequency coordinate. The method produce good qualitative results even for noisy signals (Olbrycht et al., 2007).

Instead of transforming the data to the frequency space, the Hough transform performs a parametric transform of the thermal data as a polar representation of a line (González et al., 2006a). This method is not further discussed as it requires substantial amount of user input and interpretation.

2.7.6 Matrix factorization

Principal component thermography (PCT) transforms the thermal data as an orthogonal data set such that the largest possible variance in the multivariate data is expressed first (Rajic, 2002a & 2002b). The decomposition is seen to be more appropriate than the sinusoidal decomposition of the Fourier transform in representing the transient thermal data. Another statistical correlation method is the partial least-square regression that is applied to pulse thermography data that decompose the data into a set of latent variables (López et al., 2014a & 2014b). The latent variables are similar to PCT data sets where the latent variables can be transformed into images, but in this case, the first latent image generally represents the non-uniform heating in pulsed thermography.

2.7.7 Statistical Methods

Statistical methods include high order moments, such as skewness and kurtosis (Madruga, 2008; Usamentiaga et al., 2012), which are measures of the shape of the temperature distribution compared to a probability distribution. A skewness value of zero describes a symmetrical probability distribution where the mean, median and mode correspond to the center peak of the distribution.

For a positively skewed data set, the mean and median lie to the right of the peak frequency. The reverse is true for negatively skewed. Kurtosis describes the flatness of the peak and the distribution of frequency in the tails of the distribution.

Other methods that where designed and adapted for pulse thermography in the inspection of historic documents include the Markov error contrast, time-difference contrast, total harmonic distortion, time constant analysis, and matched filtering (Larson, 2011). Matched filters having been successfully implement in multi-spectral imaging in enhancing writing in ancient documents (Griffiths, 2011) and adapted for thermographic inspection of documents. They attempt to maximize defect visibility while minimizing the visibility of non-defective pixels creating an enhanced contrast between these pixels.

2.8   Depth Characterization

Determining the depth of internal flaws has been a large focus in thermography literature and has been achieved by using calibration samples containing three or more defective regions of a similar flaw type (Zauner et al., 2010; Ghadermazi et al., 2015) and particularly on flat-bottom holes (Maldague et al., 2002; Rajic, 2002; Ibarra-Castanedo, 2005; Badghaish & Fleming, 2008; Benítez et al., 2008; Ishikawa et al., 2013). Defect detectability is clearly limited by the heat diffusion process, the applied excitation energy and noise threshold of the infrared camera. With lateral diffusion being the main contributor in limiting the depth probing range of thermography. The surface contrast is dependant on the thickness, lateral size, depth of defect as well as the thermal properties of both the defect and bulk material. Therefore trying to determine one defect parameter without knowing the other is difficult. To overcome this problem, depth inversion methods based on empirical observations of prepared samples have been proposed.

2.8.1   Thermal Contrast

The majority of the inversion methods are related to thermal contrast and its corresponding time since shallow defects produce higher contrasts at shorter times while deeper defects produce lower contrasts at later times. Depth inversion can be performed using an appropriate thermal contrast C and a time such as the beginning of thermal contrast t_{early}, half maximum contrast $t_{\frac{1}{2}}$, time of maximum contrast t_{max} and time of maximum slope t_{slope} (Balageas et al., 1987; Maldague, 2001; Han et al., 1996; Ringermacher et al., 1998). These times are denoted by Figure 2.7. A typical inversion methods shares this form

$$z = A \sqrt{t} \ C^h \tag{2.8.1}$$

with parameters A and h obtained from the calibration process.
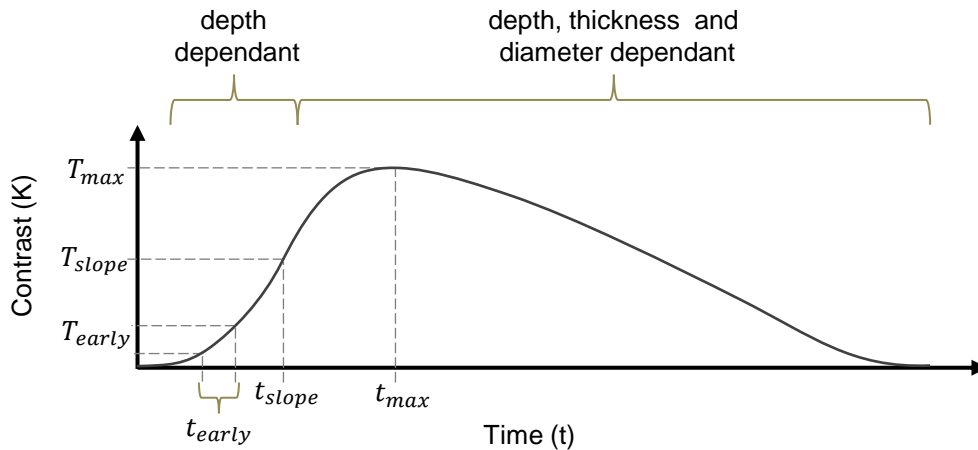
Figure 2.7: Thermal contrast times used for depth estimation in pulse thermography

Early times, (t_{early}) describe times of $1 - 5\%$ of maximum contrast. These early times are less affected by edge-effects and thus defect sizing (Maldague et al., 2002). Badghaish & Fleming (2008) reported that an aspect ratio of two or more was less susceptible to three-dimensional diffusion effects in step heating using early times. Early times contrast methods include the early detection approach which tries to determine earliest time of emergence of contrast by extrapolating a suitable one-dimensional model to zero contrast (Almond & Lau, 1994; Krapez & Balageas, 1994; Krapez et al., 1994; Balageas, 2013; Balageas & Roche, 2014).

2.8.2   Logarithmic Peak Second-derivative Method

The logarithmic peak second-derivative does not require the selection of a sound zone to define a contrast (Shepard et al., 2003). Instead the method relies on the second derivative produced by the TSR method on the raw temperature signal. This method is only valid for pulse thermography as for transient methods the second derivative does not correspond to the theoretical breakpoint previously discussed.

2.8.3   Blind frequency

Another quantitative inversion method for defect depth relies on determining the blind frequencies in the frequency domain instead of the time domain. This inversion method is taken from lock-in thermography. The thermal response of lock-in thermography suffers from blind frequencies where there exists a range

of modulation frequencies for which defects at different depths do not become visible. The relationship between thermal diffusion length μ and modulation frequency f_m was found to be (Busse et al., 1992; Busse & Rosencwaig, 1980; Saintey & Almond, 1995):

$$\mu = \sqrt{\frac{2\alpha}{\omega}} \ , \tag{2.8.2}$$

where the angular frequency is $\omega = 2\pi f_m$. The probing depth is inversely proportional to the modulation frequency, where lower modulating frequencies provide deeper depth probing, i.e. $z \propto \frac{1}{\sqrt{\omega}}$. The frequency for which a defect at a given depth becomes visible is known as the blind frequency f_b (Meola & Carlomagno, 2004). The phase of the blind frequency is directly proportional to depth z by

$$\phi(z) = \frac{z}{\mu} \ . \tag{2.8.3}$$

Applying this relationship to time domain data of pulse excitation, rather than lock-in, is quite easily achieved knowing that the thermal diffusion length of the time domain is actually derived from the solution of the frequency domain analysis. Now considering that a pulse of thermal energy is a combination of thermal waves at all frequencies, the defects will emerge for different frequencies. A phase contrast needs to be defined to normalize the phase information (Ibarra-Castanedo, 2004b)

$$\Delta\phi(f) = \phi(f) - \phi_{S_a}(f) \ , \tag{2.8.4}$$

where there is a need to select a reference sound area S_a in the phase data ϕ over the frequency f. The blind frequency (f_b) of a particular defect can the be obtained where the phase contrast reaches zero, illustrated for different defect depths in Figure 2.8. Interestingly the deeper defects show up at low frequencies and shallow defects show up at higher frequencies. This is seen to be consistent with Equation 2.8.2 where deeper defects are observed for lower modulation frequencies and visa versa.

Using Equation 2.8.2 a linear relationship exists between defect depth z and the inverse square root of the blind frequency, $\sqrt{f_b}$ (Bai & Wong, 2001; Sakagami et al. 2002; Ibarra-Castanedo & Maldague, 2004)

$$z = C_1 \sqrt{\frac{\alpha}{\pi f_b}} + C_2 \tag{2.8.5}$$

where C_1 is an empirical constant with reported values equal to 1 for amplitude data and in the range $1.5 < C_1 < 2$ for phase data for flat-bottom holes (Ibarra-Castanedo, 2006; Busse & Rosencwaig, 1980; Meola & Carlomagno, 2004). The finite range highlights again the benefits of phase data being invariant to non-homogeneous, heating power and lateral size effects and the depth is practically reduced to the estimation of f_b from the phase.
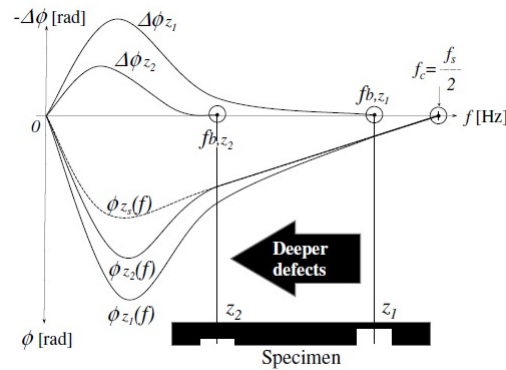
Figure 2.8: Defect depth relationship with blind frequency (Ibarra-Castanedo, 2005)

2.8.4   Other

Neural Networks and supervised learning machines have been implemented to use calibrated data to autonomously detect and estimate defect depth of similar samples under same heating conditions (Benítez et al., 2009). Other defect depth calculation methods include viewing of the polynomial coefficient images (Balageas, 2012) and RGB coloured image produced by the projection of polynomial coefficients (Roche et al., 2013). Curve fitting procedures have been proposed that derive defect depth using semi-analytical approaches from same-sided (reflection) and two-sided (transmission) experimental data (Winfree & Zalameda, 2003). A technique that did not rely on an inversion technique was investigated for step thermography. The technique determined the time of separation from the semi-infinite model. For a low thermal resistance defect, such as a simple closed delamination, "the determination of the separation time [became] impossible" (Badghaish & Fleming, 2008).

2.9   Defect Lateral Size

Lateral defect size can be determined through a simple length measurement on the image at a particular observation time $(t_{C_{slope}}, t_{C_{max}}, t_{C_{early}})$. This observation time effects the estimated accuracy of the subsurface due to increased lateral diffusion effects experienced at later times (see Section 2.4).

Even though the lateral size requires the measurement of two points defining the defect periphery, the defect periphery is blurred and no defined edge is discernible. Therefore selection of these periphery points is subject to user bias. In order to avoid user bias, automatic sizing techniques have been performed. A popular technique is image segmentation such as thresholding and edge detection using Sobel and Canny filters. The optimal performance of these techniques requires advance processing methods to produce an 'ideal'

thermogram that best approximates the defect size with increased definition of the defect periphery and uniform contrast for sound regions. An alternative method was described by Choi et al. (2008) for determining defect size without a user having to choose a threshold value. An image is taken at an appropriate time and shifted by certain number of pixels. They describe the subtraction of the original image and the shifted images as a shearing image that provides shearing phase values having maximum, minimum and zero points. These points help quantitatively determine the location and size of defects regardless of the shape of the defect.

A less automatic method is suggested by Almond & Lau (1994) that requires the measurement of the full width half maximum (FWHM) amplitude of the defects intensity profile for all images in the sequence. The FWHM method fits a Gaussian curve to the defect profile where the maximum amplitude of the curve represents the center of the defect. Instead of selecting the base of the profile, which represents the blurred defect periphery, a distance between the Gaussian curve located at half the maximum amplitude is measured. The FWHM sizes are plotted against the square root of time and linearly extrapolated to a zero time to yield estimation of defect depth. The method is limited to symmetric shaped defects and underestimates the true defect size with estimation errors on the order of 15 % (Vavilov, 2000).

The findings in literature suggest estimated delamination sizes are smaller than actual size (Rantala & Hartikainen, 1991) and concluded that there is an overestimation of actual flaw size in carbon composite material by 1.5 to 3 (Connolly et al., 1990).

2.10 Defect Thickness

Defect thickness is another parameter that characterizes the internal flaw and has a significant influence on depth and size predictions. The thermal resistance of the flaw is defined as a function of thickness Δz and thermal conductivity k of the flaw (Özi̇sik, 1985):

$$R = \frac{\Delta T}{q} = \frac{\Delta z}{k} \qquad (2.10.1)$$

For defects with a high thermal resistance $R \rightarrow \infty$, the time of separation from the semi-infinite model occurs at an earlier time compared to defects with a low thermal resistance defect, $R \rightarrow 0$ (Badghaish & Fleming, 2008). In other words, an emerging contrast is observed at different times for the same depth of defect having a different thermal resistance, which is defined by either a different thickness or thermal conductivity.

2.11 Summary

The most popular techniques for processing pulsed thermography images include the differential absolute contrast, thermographic signal reconstruction and pulsed phase thermography using the Fourier transform that produced the highest signal-to-noise ratio (Ibarra-Castanedo et al., 2009). For step heating only the high order moments and thermal signal reconstruction have been applied with reasonable success.

The net effect in thermographic inspection is that elapsed time will increase the approximation error in defect characterization. The time and amplitude of the thermal contrast is influenced by defect depth, lateral size, thickness and thermal properties of both the defect and host material. The fundamental problem with determining depth based on thermal contrast or time of thermal contrast is that a change in any of the above mentioned factors will affect the accuracy of the results. Estimation of defect depth has only been achieved through the use of inversion and curve fitting procedures based on empirical findings. The relationship found for estimating defect depth found by an inversion method, can only be applied to the same sample material sharing similar defect flaws, i.e. thickness, material properties and size.

The contrast, Fourier and wavelet transform inversion methods are fairly straightforward to apply once the data is processed with the respective processing method. Fitting data to a semi-analytical curve however can be more challenging, but both techniques still rely on a calibration sample.

The usefulness of depth inversion methods in industry may be a problem when defect geometry and material parameters are not known *a priori*. More importantly, many of the quantitative inversions methods have been performed on flat-bottom holes, which describe a high thermal resistances not exhibited by true flaws.

Chapter 3

Experimental Study

Transient thermography is performed on target specimens that include carbon and glass fibre composite laminates (CFRP and GFRP), polymethylmethacrylate (PMMA) polymer and industrial specimens, which range from thin laminates to honey-comb sandwiched composites. This chapter discusses the experiments performed to minimize the reflections and non-uniform heating effects on the target surface.

3.1   Transient Thermography Setup

The transient thermography setup comprises of an infrared camera, a light controller and two or more light sources to minimize unsymmetrical heating effects, seen in Figure 3.1. The setup is orientated in the reflection mode and a controller is used to synchronise the start of heating and recording.
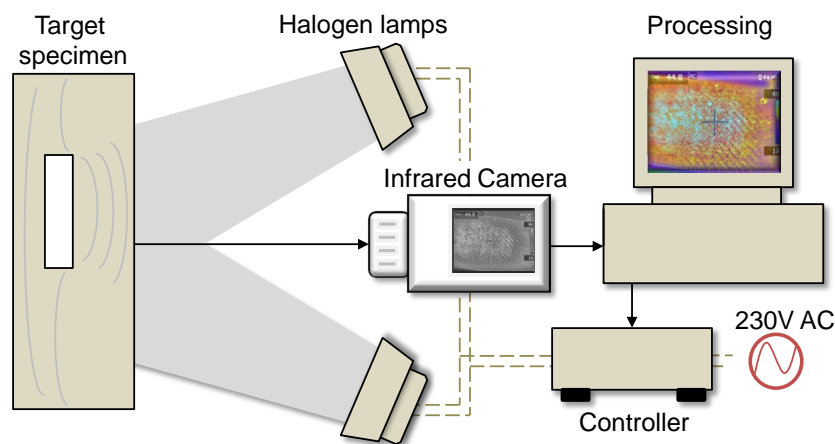
Figure 3.1: Experimental setup for transient thermography

3.1.1   Thermal Camera

Data acquisition was performed with a FLIR® E60.The camera's detector is a focal plane array, uncooled microbolometer with a spatial resolution of 320×240 pixels. The camera is a medium-wave infrared camera (MWIR) operating in the 7.5 to 13 µm spectral band. The sampling frequency is limited to a maximum of 30 Hz with a noise equivalent temperature difference, NETD = 0.05 °C with an accuracy of ± 2 %. The E60 is a portable, hand-held infrared camera with a wide field of view intended for building and outdoor thermal inspection. This camera may not be ideal for detecting small defects due to its low sensor resolution, wide viewing angle and minimum focus distance of 0.4 m.

Research-grade thermal cameras are typically cryo-cooled for better noise attenuation and operate at higher frame rates $(60-120 \text{ Hz})$ with greater spatial resolution and shorter minimum focusing distance to inspect smaller anomalies. High frame rates may not be a central consideration for inspecting composites with a low thermal diffusivity where the thermal response occurs over a longer time in contrast to the rapid thermal events in pulsed thermography (Maldague, 2001). The spatial resolution and minimum focusing distance will only limit the detection of small anomalies and measuring accuracy of defect sizing. Nevertheless larger anomalies are of greater interest than minute details as they are more detrimental to the materials performance. In practise a defect can be detected if its detectable size is at least two pixels wide and the thermal contrast is greater than the NETD to be not mistaken as noise.

3.1.2   Heating Source

Tungsten-halogen lamps are preferred for a transient setup for their affordability, availability, step heating capabilities. They can be arranged in a variety of designs. Halogen lamps produce a fairly uniform and wide power distribution for all wavelengths. This can be described by the lights spectral power distribution seen in Figure 3.2. For an increase in rated power of the halogen lamp the spectral distribution will produce high energy per wavelength. The peak wavelength(s) will also shift towards shorter wavelengths (or higher frequencies) according to Plank's Law (see Appendix A). This allows the lamp source to be suitable for a range of materials with different spectral absorption properties. Infrared light sources were not considered as they may introduce additional infrared reflections on the target surface.

Another consideration in the use of halogen lamps may be their increased power density, which is the amount of power per unit volume (W m^{-3}), especially in cases when the target surface is large or the overall space is constrained. Moreover performing a comparative study on other heating sources may be unnecessary as one can simply filter out the desired wavelengths produced by the halogen lamp.
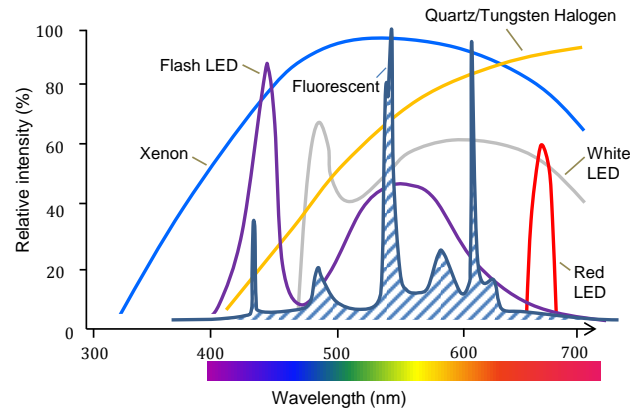
Figure 3.2: Relative wavelength energy of common light sources (adapted from Sedgewick, 2014)

3.1.3   Front-on Heating Setup

An initial setup was attempted to produce uniform heating on the target specimen, since this is a significant problem in thermography. In order to produce optimal heating that favours more uniform heating, the surface needs to be directly parallel to the heating source. Placing the halogen lights to the sides of the sample will always create irregular illumination effects and hotspots (Maldague et al., 1996; Ishikawa et al., 2013; Gaussorgues & Chomet, 2012). However front-on heating is not always possible while using large flood lamps as they are typically bulky and get in the way of the camera's field of view.

Consequently a frontal heating setup was implemented using 20 collimating halogen downlights arranged in a custom designed parabolic dish configuration. The parabolic configuration was designed to have the focal point behind the sample surface to reduce the central concentration of heat. The particular use of the parabolic configuration was to direct heat towards the central area of the sample as the center lights of the configuration were removed to allow the central positioning of the infrared camera. The focal point was determined using the minimum focusing distance of the camera, since the camera needed to be as close as possible to provide the best spatial resolution of the sample. The focal point position ensured that the cone of influence falls on the entire surface of the samples. This setup can be seen in Appendix B.

The maximum power output is rated at 1000 W (20×50 W). Literature is vague on the required heat source power. From a few studies that report on transient heating, the lamps had total power ratings of 1200 to 3000 W (Roche & Balageas, 2014; Usamentiaga et al., 2014).

The setup produced a fairly uniform heating pattern but was highly sensitive to unfavourable heating-setup reflections when a reflective sample was inspected. This configuration brought attention to the adverse effects of in-

frared reflections from ambient sources as well as the heating setup. Even when the lights were turned off, the residual heat from the bulbs introduced noticeable artefacts in the thermogram that masked the contrasts of defects. Similarly the reflected infrared radiation from the light bulbs heated the lens of the infrared camera that created additional noise in the image. This noise could not be mitigated by simple subtraction of an initial frame as the lens temperature increased for the duration of the experiment. The light bulbs as well as the thermal signature of the infrared camera contributed to higher thermal reflections from the sample surface over the duration of the heating.

After discovering through preliminary testing that a glass pane is opaque to infrared wavelengths, the glass pane was positioned in front of lights to reduce the infrared reflections produced by the heating source. Figure 3.3 shows a thermogram of a target sample that is contaminated with infrared reflections that is produced by a tear-drop shaped halogen light and its housing. As the glass pane is moved in front of the lights, designated by the arrow, the measured surface reveals four circular sub-surface defects.
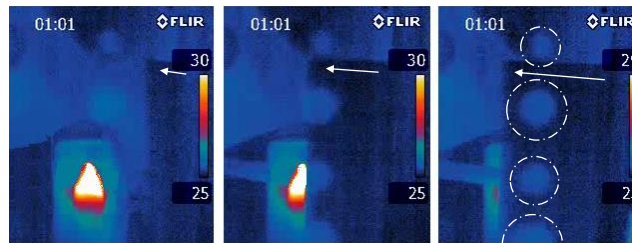
Figure 3.3: Removal of heating source reflections through a glass-silica pane

Other transparent mediums such as Plexiglas® and water baths can also be used in this case. These materials have active vibrating groups that include carbonate (CO_3^{2-}), hydroxide (OH^-) or nitrate (NO_3^-) molecules which will absorb most infrared wavelengths (Florence et al., 1950). The absorption effects are linked to material thickness and a 5 mm glass pane performed well in reducing radiation effects. The thickness of the pane made the heating time of the pane longer, which further ensured that the glass pane did not emit a large amount of its own radiation towards sample. Henke et al. (2004) proposed the suppression of thermal reflections through an infrared polariser.

3.1.4 Angled Heating Setup

The angled heating setup was a more straightforward heating setup that was designed to have a maximum power output of 4000 watt using four 1000 watt tungsten-halogen double-ended tubes. The setup consisted of two flood lamps that were angled 120° apart on either side of the target specimen. This angle produced the best distribution of heat and was wide enough to reflect any

residual infrared radiation away from the camera. The lights were positioned
0.4 m away from the sample in order to ensure most of the energy was absorbed
by the sample yet far enough to slightly reduce uneven heating effects. The
increase in heating power from 1000 watt to 4000 watt increased the overall
contrast of the defects but also introduced more pronounced irregular heat-
ing contrasts. A 5 mm glass cover was used as a filter to mitigate infrared
reflections from the heat source. Further description of this setup is given in
Appendix B.

3.1.5   Other Considerations

A wooden frame was design to hang the samples in-front of the camera by
elastic-bands to minimize direct contact losses. Direct material contact with
the sample was observed to increase contrast variance along the edge in contact.
The remaining radiation and convective losses could not be controlled.

To ensure a consistent testing environment, the experiments were per-
formed in a small and dark room that experienced minimal changes in ambient
temperature. Sources of radiation, such as lights and windows, were either
blocked or covered with a red film that prevents transmittance of infrared.
This ensured that each experiment was performed in the same conditions for
later comparison.

3.2   Software

The software can be divided into two types: camera software and advanced
signal processing software. Camera software interprets the camera's output
signal as temperature measurements and converts the data into a more con-
venient format. This software is commercially available and is specific to a
particular brand or series of the infrared camera. Each infrared camera has
its own proprietary software and image format that limits the practical use
of the camera without purchasing the necessary software. Processing software
on the other hand describes implementation of signal processing utilities. For
commercial software that is found available online the software suites do not
include advanced signal processing functionality of methods proposed in liter-
ature but may include traditional image enhancement features. This was also
found to be true for other non-commercial software suites.

The current software that is supplied with the E60 infrared camera, *FLIR®
Tools+*, is restricted to basic image viewing and in this particular case limits
one to export the raw signal as a compressed .avi file. The compressed video
(.avi) file contains normalized image frames that discards actual temperature-
time information. For this reason the extraction of the thermal sequence can
be achieved by extracting in-code data blocks. These blocks can be found by

identifying common fixed hexadecimal constants of the recorded proprietary file as described in Appendix C.

A graphical user interface (GUI) was created in Matlab® 2013 to visualize and apply both common and advanced signal processing methods. Advanced processing methods include algorithms published in thermographic literature and discussed in Chapter 4. This GUI software is made freely available. The software's functionality will be discussed throughout the thesis and is a major contribution of the research. A brief description and a download link of the GUI is provided in Appendix D.

3.3 Target Specimens

The experimental specimens chosen to be evaluated in this project fall into three categories: (1) polymethyl methacrylate (PMMA), (2) FRP composites and (3) real industry composite samples. Flat plate specimens are preferred in this study for their simple construction with multiple defects and flatness - since curved surfaces are more susceptible to irregular heating patterns (Mayr et al., 2008). All samples are described in Appendix E. The samples all had a sticker placed on the front side of the material to define a reference size for lateral sizing and a steel washer was placed on the backside to represent the emergence of the rear-wall for depth estimation.

3.3.1 Polymethyl methacylate (PMMA)

Polymethyl methacylate (PMMA/acrlyic) is generally known by its common tradenames of Perspex® or Plexiglas®. PMMA shares similar thermal properties to that of epoxy resin present in fibre-reinforced composites (see Table E.1). The material can be assumed perfectly homogeneous, making it a good starting point for defining defect characterizing procedures. Defining exact defect sizes and depths are more easily attained in PMMA than inclusions in composite laminates, which are susceptible to resin variances between plies. The uniform thermal properties of PMMA, particularly its uniform emissivity, can highlight any inconsistencies observed in the heating pattern and adjustments can be made to the setup to promote more uniform heating. Also camera noise can be better gauged from the initial cold thermograms of a uniform surface.

Two different PMMA plates were chosen and their sample layouts with flat-bottom holes are shown in Figure 3.4. The first is an opaque black PMMA plate ($220 \times 220 \times 5$ mm) chosen to approximate a high emissive body. Both square and circular flat-bottom holes were milled from this opaque plate. Each opaque sample contained three columns at surface depths of $1, 2$ and 3 mm with each column containing various lateral sizes $10 - 30$ mm.

Since not all composites are perfect emitters, a clear and transparent PMMA plate ($220 \times 220 \times 10$ mm) was chosen. The comparison will help
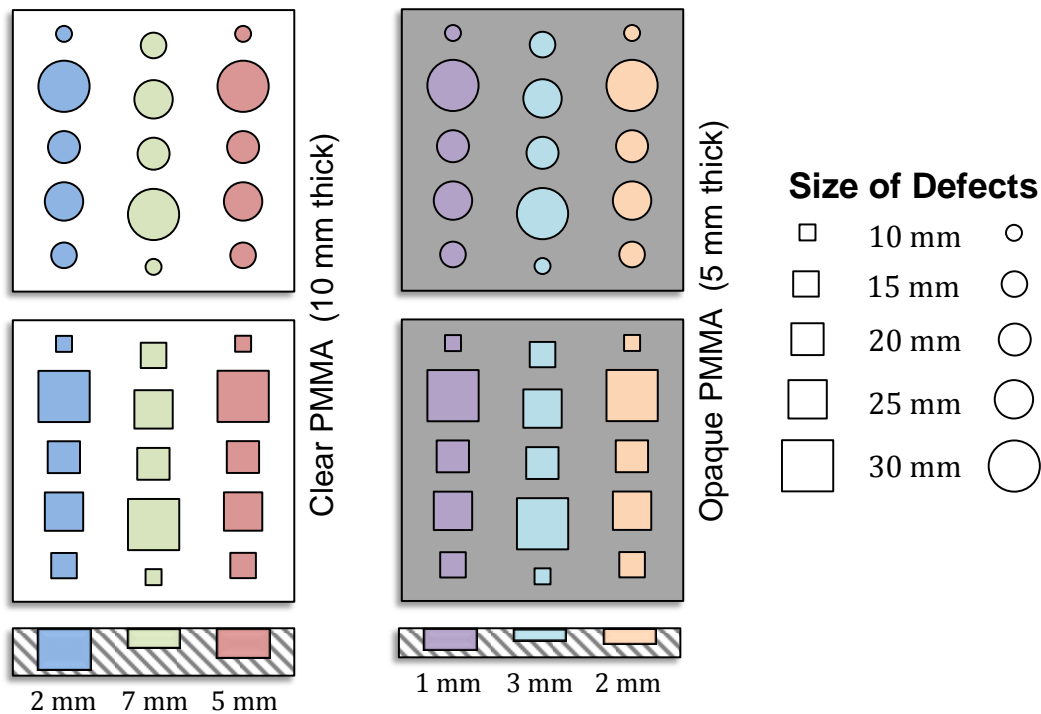
Figure 3.4: Polymethyl methacylate (PMMA) samples with defect layouts

evaluate the effects of spectral absorption and emissivity properties. These plates share the same defect organization, as seen in Figure 3.4, but with surface depths of 2, 5 and 7 mm.

The use of a 10 mm plate will aid in determining the depth limitations of transient thermography, as the aspect ratio of the deepest and smallest defect will be close to one. Clearly the clear PMMA is a non-ideal absorber or emitter but any significant outcome in depth detection will highlight the performance of transient thermography.

3.3.2 Composite

The composites selected for inspection are glass and carbon plain-weave fiber reinforced polymers. The weave is preferred in industry over unidirectional fibers for its transverse and longitudinal strength in both fibre directions and the iconic surface finish typical in carbon fiber polymer composites. Again the same plate size, 220×220 mm, was chosen. Each specimen contained 15 polytetrafluoroethylene (PTFE) square inclusions arranged in three columns at various ply depths having five lateral sizes $(10-30$ mm$)$. PTFE is also known by its trade name as Teflon®. The PTFE inserts were used to replicate finite delaminations due to its non-stick properties and its resistance to epoxy infiltration. Equally the PTFE inserts share similar properties to that of the

epoxy creating a closer approximation to delaminations that are still in contact even after debonding. The inserts are inserted at ply depths described in Figure 3.5 and approximated in Table 3.1. The ply depths are calculated from the average ply thickness determined from the total thickness of the cured composite. The material was measured with a Vernier caliper (accuracy = 0.05 mm) on all four sides of the composite before an average material thickness was calculated.
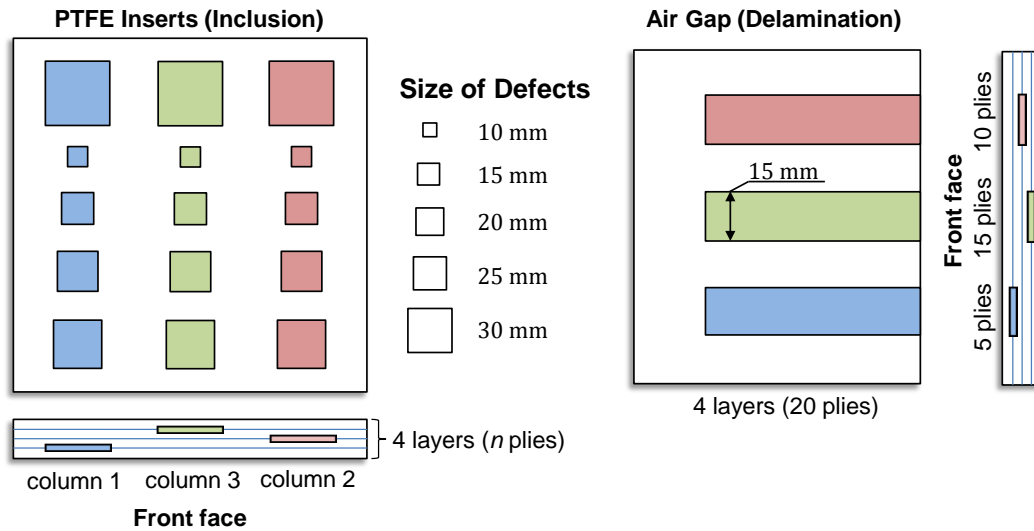
Figure 3.5: Composite samples with PTFE inclusion layouts (left) and air-gap delaminations (right)

The composites were made using an ambient curing epoxy, Ampreg 21 with Ampreg 21 Standard Hardener, and vacuum sealed on a smooth granite surface. The composites were left for 8 hours to cure at standard room temperature and pressure. Due to the PTFE inserts being much thicker than the layers of laminate-fibres, noticeable voids and bubbles were trapped in the immediate vicinity of the inserts. An observable difference in the contrast of the inclusions and voids was noted in the inspection.

The thermal mismatch factor describes the thermal reflectance of the flaw to oncoming heat and consequently on the ability of the flaw to produce a contrast (refer to Section 2.5). The factor can be calculated for the above materials and their flaws using thermal properties provided in Table E.1:

$$\Gamma_{\text{PMMA/air}} = -0.96, \qquad \Gamma_{\text{epoxy/PTFE}} = 0.1225, \qquad \Gamma_{\text{epoxy/air}} = -0.98. \quad (3.3.1)$$

The implications of a delamination separated by air and PTFE are significant. The absolute value of the thermal mismatch factor for air in PMMA and epoxy is close to one. This suggests a relatively higher contrast is expected

for an air-gap delamination than for the PTFE insert, which shows a poor thermal mismatch factor close to zero. This reinforces the idea of the PTFE resembling a closed delamination. The poor thermal mismatch factor was a problem for the carbon composite specimens. For this reason both a glass and a carbon fiber laminate was created with a PTFE strip that was removed after curing to produce an air-gap delamination. This provided the case where the delamination is fully detached from the adjacent plies. These composites are illustrated in Figure 3.5 having three depths equally spaced between 20 plies.

Table 3.1: Depth of inclusions and delaminations for the composite samples

	Fibre density	No. of plies	Insert thickness	Plate thickness	Thickness per ply	Depth			Aspect ratio
						Col. 1	Col. 2	Col. 3	
	$g\,m^{-2}$		mm	mm	mm	mm	mm	mm	
CFRP200A	200	20	0.50 (PTFE)	5.51	0.28	1.38	2.76	4.13	> 2.4
CRFP200B	200	20	0.25 (PTFE)	5.68	0.28	1.42	2.84	4.26	> 2.3
GFRP200	200	20	0.50 (PTFE)	5.40	0.27	1.35	2.70	4.05	> 2.5
GFRP106A	106	40	0.50 (PTFE)	5.24	0.13	1.31	2.62	3.93	> 2.5
GFRP106B	106	20	0.50 (PTFE)	2.41	0.12	0.60	1.21	1.81	> 5.5
CRFP200DEL	200	20	0.50 (Air)	6.58	0.33	1.65	3.29	4.94	> 2.0
GFRP200DEL	200	20	0.50 (Air)	5.10	0.26	1.28	2.55	3.83	> 2.6

Two carbon fibre samples, CFRP200A and CFRP200B, where produced using $200\,g\,mm^{-2}$ density plain-weave fibers, with the difference in the thickness of the PTFE inserts being 0.5 mm and 0.25 mm respectively. The thickness of the defects is proportional to the defect's thermal resistance which has an noticeable effect on the visibility of defects.

The importance of material variation and the effect it has on thermal contrast and defect depth, made selecting glass fibre an appropriate choice. To compare glass fibre to the carbon fiber, GFRP200 was created having a similar fiber density of $200\,g\,mm^{-2}$. Furthermore the effect of fibre density (or ply layers) was evaluated on GFRP106A glass fibre composite having a density of $106\,g\,mm^{-2}$. This fibre density consisted of a much smaller plain weave pattern and fibre thickness. For every one ply of the $200\,g\,mm^{-2}$ glass-fibre weave, two plies of the $106\,g\,mm^{-2}$ was used. Both composites can now be considered to have defects at the same depth (see Table 3.1) and share similar thermal properties.

In addition, a thin glass fibre ($106\,g\,mm^{-2}$) sample, GFRP106B, consisting of 20 plies was investigated that was unintentionally not properly vacuum-sealed. A noticeable difference in the air-pockets and the PTFE is observed that corresponds well to the thermal mismatch factor. The air pockets are more pronounced than PTFE defects at the same depth and will be further discussed in Chapter 5.

All composite layouts containing PTFE inclusions follow the typical organization shown in Figure 3.5 and have an aspect ratio greater than two.

3.3.3   Real Industry Samples

Various defective and non-defective samples were supplied by AAT Composites (Pty) Ltd. Somerset West in order to evaluate transient thermography on real composites being made in industry. The details of such defective and non-defective samples were undisclosed during the testing and processing stages to ensure there was no bias in the identification of suspected defects. This will indicate if human expertise is a critical part of the thermography system and the ability of transient methods to detect common issues in industry. Images of these samples are shown in Appendix G.

3.4   Parametric Studies

The complexity of heat transfer phenomena in transient thermography remains a key obstacle in establishing a reliable test procedure and setup. Along with limited research in transient thermography there is a desire to understand the effects of thermal response on defect detection as well as establishing methods of characterizing defects similar to those methods that have been well documented in pulsed thermography. With this in mind, a series of parametric studies were conducted, using the specimens and experimental setups described in this chapter. The main outcomes of the studies are evaluating the effectiveness of transient thermography for a change in:

- spectral absorbance - opacity and material variations,

- thermal input - duration and intensity,

- lateral defect shapes - circle versus square geometries,

- thermal properties - carbon, glass and PMMA,

- fibre content - glass fibre density, and

- thermal resistance - blind holes (flat-bottom), PTFE and air voids.

Chapter 4

Thermal Image Processing

The thermal contrast between defective and non-defective regions is normally weak and degraded by uneven distribution of heat, various noise sources, environmental reflections and optical variability in the target surface. Optical variability includes variations in local emissivity, surface cleanliness and non-planar geometries. Consequently the thermal contrast is typically poorer for flaws that represent real delaminations or voids. Therefore through the application of processing algorithms developed for thermographic inspection, the subtle anomalies can be enhanced to provide an optimal signal for qualitative and quantitative investigations.

This chapter provides the theoretical background for a variety of popular signal processing methods that are provided in the open-source software developed for this project. The methods provided here are applicable to transient heating regimes, even though most of these methods have been developed solely for flash thermography.

4.1   Organization of the Thermal Sequence

The measured thermal signal consists of a sequence of frames having a spatial resolution of $N_x \times N_y$ pixels. In order to suitably handle the thermal sequence the individual frames can be concatenated as a three-dimensional $N_x \times N_y \times N_t$ matrix where N_t defines the total number of frames in the sequence that starts the moment the heat is applied to the sample, shown in Figure 4.1. The number of frames is the product of total recording duration t_{acq} and sampling frequency f_s of the camera, i.e. $N_t = t_{acq}f_s$. The sampling frequency defines a time step Δt that describes the time resolution.

The signal can be processed as either a two-dimensional array (image) or on a pixel-wise basis of the temperature response over time. Two-dimensional processing methods are generally qualitative as they independently process each frame with no account of temporal information.
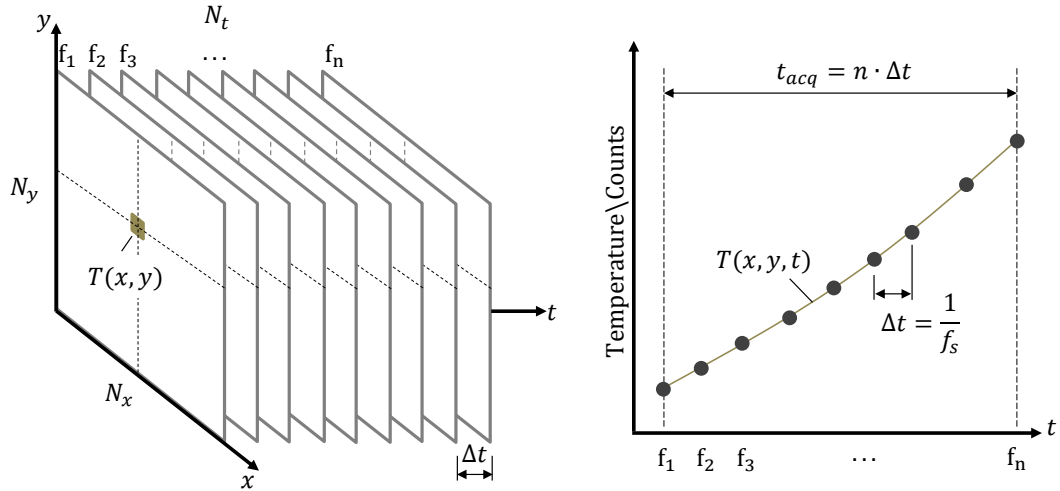
Figure 4.1: Thermal data cube and a pixel's temperature response over time

4.2   Data Normalization

The temperature can be expressed as an excess surface temperature measurement that indicates a change in surface temperature after the heat has been applied to the target sample. To display the excess temperature as a grayscale image, data normalization needs to be performed. Data normalization can be achieved by either two-dimensional or three-dimensional normalization methods defined as

$$I_{N_{2D/3D}} = (I - a)\frac{(d - c)}{(b - a)} + c, \qquad (4.2.1)$$

where I is the original data set with a data range $[a, b]$ and I_N is the normalized data set for the desired range $[c, d]$. Data normalization does not change the quality of the raw signal as the thermal data is handled as a 16-bit array and equally displayed as a 16-bit indexed image.

4.3   Spatial Enhancement Methods

Spatial enhancement methods originate from classical image processing methods and are commonly accepted as typical image enhancement methods found in most image processing handbooks (Gonzalez & Woods, 2010). These methods are performed as a post-processing procedure to enhance the quality of the image.

4.3.1   Spatial Noise Reduction

Thermograms are prone to ambient and inherent camera noise. There are many ways to de-speckle or de-noise an image using linear, non-linear or even statistical operators. Linear filters are less preferred as they generally blur detail in the images. Two non-linear noise filters, Gaussian low-pass and adaptive median filter, are used in the present work for reducing spatial noise.

4.3.2   Histogram Equalization

Histogram equalization (HE) is a common image processing technique of adjusting image contrast by redistributing the intensities of the image's histogram. HE allows the most frequent intensities to be redistributed to other intensity levels enabling lower frequency intensities such as the defect intensities to gain increased contrast. Modified HE methods have built on the classical HE method to reduce oversaturation and maintain finer detail in the image. The definitions for modified HE methods can be found elsewhere (Abdullah-Al-Wadud et al., 2007; Štruc et al., 2009; Park et al., 2008; Sheet et al., 2010).

4.3.3   Multiscale Retinex

The multiscale retinex (MSR) algorithm is a photometric normalization technique proposed by Jobson et al. (1997) from the field of facial recognition and has been used in X-ray photography (Rahman et al., 2001). The MSR performed well on enhancing detail and removal of uneven-heating compared to other photometric normalization techniques. This method is seen to resemble how our eyes (retina) perceive variations in grayscale intensities.

Photometric normalization is a technique of separating the image into two components, namely an illumination image containing low spatial frequencies and reflectance image containing high spatial frequencies. The high spatial frequencies represents edges and higher level of detail and this image will present an enhanced image with higher level of detail

4.3.4   Pseudo-Colour Images

Pseudo-colours are used to instantly highlight any irregularities in the grayscale images. This is a result of colour receptors (cones) of a human eye having a higher spatial acuity compared to that of rods, which are responsible for low light vision. Pseudocolours systematically map each grayscale intensity to a colour according to a colour table.

Figure 4.2 shows a variety of common colour maps. A new colourmap is proposed using complementary colours as seen in Figure 4.2d. When complementary colours are put together they create the strongest contrast. Therefore

(a) Grayscale   (b) Jet   (c) Logarithmic jet (d) Complementary
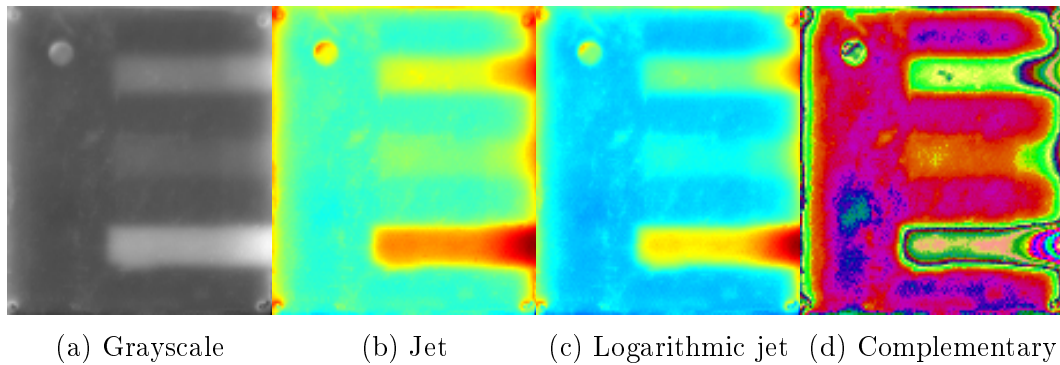
Figure 4.2: The benefits of colourmaps on thermograms

any slight change in intensity will be more pronounced with this map. The choice of colourmap depends on the image itself. Logarithmic colourmaps are more appropriate than linear colourmaps for visualizing thermograms (Klein et al., 2008) as seen in Figure 4.2c.

4.4   Thermal Contrast Enhancement

The simplest form of enhancing detail in a thermogram is through thermal contrast enhancement. Each of these methods require the selection of a sound area S_a which can be one pixel or the average of selected sound areas. The differential absolute contrast and modified differential absolute contrast methods do not require the selection of a sound area S_a but rather an image frame before defects begin to appear.

4.4.1   Absolute Contrast

Absolute contrast is the classical and most basic contrast definition describing the excess temperature over a defect-free region:

$$C_{abs}(t) = T(t) - T_{S_a}(t) \tag{4.4.1}$$

where $T(t)$ is the temperature for any pixel and $T_{S_a}(t)$ is the temperature for chosen sound area at time t.

4.4.2   Standard Contrast

Standard contrast was developed to suppress the impact of reflections produced by the surrounding environment through subtraction of an image's pixels at time t_0 before heating (Maldague, 2001):

$$C_{std}(t) = \frac{T(t) - T(t_0)}{T_{S_a}(t) - T_{S_a}(t_0)}. \tag{4.4.2}$$

4.4.3   Normalized Contrast

Variations in surface emissivity shift the amplitude of the thermal time history of each pixel making the subtraction of a sound zone less effective. Normalized contrast operates on normalizing each pixel with respect to the time of maximum temperature, t_{max} or the end of the sequence, t_{end}. The method is intended to minimize variability in optical effects that include emissivity, non-uniform heating and absorptivity lengths (Balageas et al., 1991, Balageas et al., 2012). The normalized contrast is defined as

$$C_{norm}(t) = \frac{T(t)}{T(t_{max})} - \frac{T_{S_a}(t)}{T_{S_a}(t_{max})}. \tag{4.4.3}$$

4.4.4   Running contrast

The running contrast reduces the effects of differences in surface emissivity as it normalizes each pixel with the temperature of the chosen sound area S_a at a time t. The running contrast is defined as (Maldague, 2001)

$$C_{run}(t) = \frac{T(t) - T_{S_a}(t)}{T_{S_a}(t)} = \frac{C_{abs}(t)}{T_{S_a}(t)} \tag{4.4.4}$$

4.4.5   Differential Absolute Contrast (DAC)

The differential absolute contrast (DAC) removes the need for the manual selection of a sound area S_a. The technique was originally based on the Dirac delta function for pulsed thermography (González et al., 2004a), which has now been extended to step thermography.

The differential absolute contrast is a form of extrapolated contrast based on the extrapolation of temperature at early times through the one-dimensional semi-infinite model at the surface $z = 0$ of the specimen. The contrast is formulated on the assumption that a sound zone is expected to follow the semi-infinite model for early times t:

$$\Delta T_\infty(t) \approx \Delta T_{S_a}(t), \tag{4.4.5}$$

where the half-space semi-infinite model for step heating is

$$\Delta T_\infty(t) = \frac{2Q}{e} \frac{\sqrt{t}}{\sqrt{\pi}}. \tag{4.4.6}$$

At a time t' just after heating and before an actual defect becomes visible the measured temperature at the surface of the specimen is assumed to behave

as an ideal sound area S_a, i.e. $\Delta T_{meas}(t') = \Delta T_{S_a}(t')$. At this time the surface has not been affected by the existence of a internal defect and therefore the local temperature of a defective area is exactly the same for a sound zone. A practical assumption is made that follows Equation 4.4.5 where the measured temperature ΔT_{meas} at t' is equal to the half-space semi-infinite model at t' (Klein et al., 2008). This can be defined for a step pulse at time t' as

$$\Delta T_\infty(t') = \frac{2Q}{e}\frac{\sqrt{t'}}{\sqrt{\pi}} = \Delta T_{meas}(t'), \qquad (4.4.7)$$

where $\Delta T_{meas}(t')$ and t' are known measurements from the thermal data. Now Equation 4.4.7 is expressed for Q/e as

$$\frac{Q}{e} = \Delta T_{meas}(t')\ \frac{1}{2\sqrt{\pi t'}}. \qquad (4.4.8)$$

Substituting Q/e into Equations 4.4.5 and 4.4.6, the extrapolated temperature of a sound area is defined as

$$\Delta T_{S_a}(t) \approx \sqrt{\frac{t}{t'}}\ \Delta T_{meas}(t'). \qquad (4.4.9)$$

Using the absolute contrast definition (Eq. 4.4.1), the extrapolated thermal contrast is defined using the difference of the measure temperature $\Delta T_{meas}(t)$ and extrapolated temperature $\Delta T_{S_a}(t)$:

$$\Delta T_{DAC}(t) = \Delta T_{meas}(t) - \sqrt{\frac{t}{t'}}\ \Delta T_{meas}(t'). \qquad (4.4.10)$$

The DAC method is only valid for early times as at later times the thermal response of both the sound and defective areas deviates from the semi-infinite model where $\Delta T_\infty(t) \neq \Delta T_{S_a}(t)$.

4.4.6   Interpolated Differential Absolute Contrast (IDAC)

The interpolated differential absolute contrast (IDAC) explicitly introduces the sample's thickness by means of solving the one-dimensional heat problem in the Laplace space using thermal quadrupoles, before computing the inverse Laplace transform (Benítiz et al., 2006). The IDAC is a modification to the DAC method described above, which performs temperature extrapolation of a one-dimensional model. However the extrapolation follows the one-dimensional model of finite slab thickness. This algorithm requires knowledge of the material's diffusivity and thickness.

Figure 4.3 illustrates a thermal model of an insulated slab in Laplace space with boundary and initial conditions. To describe the boundary and initial conditions let the Laplace transform of the surface temperature be defined
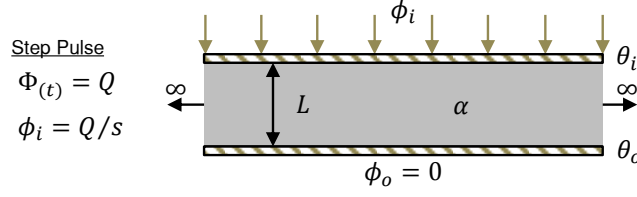
Figure 4.3: Insulated slab model in Laplace space

as $\mathcal{L}\left(\Delta T_{slab}(t)\right) = \theta_i(s)$ and let the heat flux density function be defined as $\mathcal{L}\left(\Phi(t)\right) = \phi_i(s)$ for a Laplace variable s. The rear-wall Laplace temperature, and heat flux density can be respectively defined as outputs $\theta_o(s)$ and $\phi_o(s)$. The problem can be solved through the thermal quadrupole equation knowing only the values at $z = 0$ and $z = L$:

$$\begin{pmatrix} \theta_i \\ \phi_i \end{pmatrix} = M \cdot \begin{pmatrix} \theta_o \\ \phi_o \end{pmatrix} \qquad \text{with} \qquad M = \begin{pmatrix} A & B \\ C & D \end{pmatrix}, \qquad (4.4.11)$$

where the quadrupole matrix M for a solid slab is

$$\begin{aligned} A = D &= \cosh(\kappa L), & B &= \sinh(\alpha L)/(\kappa k), \\ C &= \alpha \kappa \; \sinh(\alpha L), & \kappa &= \sqrt{s/\alpha}. \end{aligned} \qquad (4.4.12)$$

The Laplace quadrupole in Equation 4.4.11 can be alternatively expressed as:

$$\theta_i = A\theta_o + B\phi_o \qquad (4.4.13)$$

$$\phi_i = C\theta_o + D\phi_o \qquad (4.4.14)$$

The Laplace transform of surface heat flux density for step heating are $\phi_i = \mathcal{L}(\Phi_{(t)}) = Q/s$ (Maillet et al., 2000). Taking into account $\phi_o = 0$ since the plates rear-wall is assumed adiabatic and knowing ϕ_i, the Laplace surface temperature can be expressed as

$$\theta_i = \frac{QA}{sC} = \frac{Q}{e} \; \frac{\coth \sqrt{sL^2/\alpha}}{s\sqrt{s}} = \frac{Q}{e} \; \theta_i' \qquad (4.4.15)$$

Solving in a similar manner to the DAC method, the change in temperature of the sound zone can be approximated by the inverse Laplace of the the surface temperature:

$$\Delta T_{slab}(t) = \mathcal{L}^{-1}(\theta_i)|_t = \frac{Q}{e}\mathcal{L}^{-1}(\theta_i')|_t \approx \Delta T_{S_a}(t) \qquad (4.4.16)$$

where the inverse Laplace requires a numerical approximation that can be performed by either Talbot's method (Abate & Whitt, 2006) or Gaver-Stehfest algorithm (Stehfest, 1970). Because $\Delta T_{meas}(t')$ can be expressed as

$$\Delta T_{meas}(t') = \Delta T_{slab}(t') = \frac{Q}{e} \mathcal{L}^{-1}(\theta_i')|_{t'}, \qquad (4.4.17)$$

in this extrapolated contrast method, a Q/e function can be rewritten once again and introduced into Equation 4.4.16:

$$\Delta T_{S_a}(t) \approx \frac{\mathcal{L}^{-1}(\theta_i')|_t}{\mathcal{L}^{-1}(\theta_i')|_{t'}} \Delta T_{meas}(t') \qquad (4.4.18)$$

Therefore the modified DAC is calculated as the difference between the measured and extrapolated sound region:

$$\Delta T_{IDAC} = \Delta T_{meas}(t) - \frac{\mathcal{L}^{-1}(\theta_i')|_t}{\mathcal{L}^{-1}(\theta_i')|_{t'}} \Delta T_{meas}(t') \qquad (4.4.19)$$

4.4.7 Normalized DAC Methods

Both DAC methods introduced so far are insensitive to surface non-uniformities and produce relatively flat sound regions. However regions other than sound zones are still affected by surface emissivity and local heating effects producing changes in temperature amplitudes. To account for this problem, the DAC methods can be normalized as follows (Klein et al., 2008)

$$\Delta T_{normalizedDAC}(t) = \frac{\Delta T_{meas}(t)}{\Delta T_{meas}(t')} - \frac{\mathcal{L}^{-1}(\theta_i')|_t}{\mathcal{L}^{-1}(\theta_i')|_{t'}}, \qquad (4.4.20)$$

which allows better quantitative estimations even though the images may not be visually appealing.

4.4.8 Markov Error Contrast

The Markov error contrast is defined as the error between the actual and an estimated temperature T_{est} for each individual pixel's time sequence (Larson, 2011)

$$E(t) = T(t) - T_{est}(t). \qquad (4.4.21)$$

The Markov error contrast is based on a Markov chain treating each temperature in the pixel's time sequence as independent. In order to evaluate the error at time t an estimated temperature is required at the same time. Thus the estimated temperature can be calculated as a function of the previous temperature in time and repeated until each temperature has synthetically been reconstructed. Using a simplified one-dimensional response for step heating (recall (Eq. 4.4.10) the estimated temperature can be evaluated. In this case the Markov error will represent and amplify any deviation from an ideal sound area S_a response. The estimated temperature can therefore be calculated by using a modified version of Equation 4.4.10:

$$T_{est}(t) = T(t-1) \cdot \sqrt{\frac{t-1}{t}} \ , \tag{4.4.22}$$

where $T(t-1)$ is the previous temperature at a current time t in thermal sequence.

4.5 Signal Transforms

The signal transforms are based on the fact that it is possible to reconstruct any continuous function in another domain space. Two methods have been proposed to enhance overall defect detectability and provide inversion techniques for depth. These methods are known as the Fourier transform (FT) and wavelet transform (WT). Both transforms reconstruct the pixel's temperature signal in the frequency space where amplitude and phase images can be retrieved. Phase images have shown to be less affected by surface emissivity, surface features and non-uniform contrasts.

4.5.1 Fourier transform

The one-dimensional discrete Fourier transform is applied to the temperature history of each pixel $T(t)$ as (Ibarra-Castanedo, 2005)

$$F_k = \Delta t \sum_{n=0}^{N-1} T(n\Delta t) \exp^{-j2\pi nk/N}, \qquad k \in \mathbb{Z}, \tag{4.5.1}$$

where $j^2 = -1$, $n = (0, 1, 2, \cdots, N-1)$ defines the next sampling time for N sample points separated by a sampling interval Δt and k designates the frequency increment $(k = 0, 1, 2, \cdots, N)$. The Fourier transform is defined to cover infinite frequencies $k \to \infty$, but considering that there is a finite number of time samples defined by the signal of length N_t, the number of frequencies needed to adequately represent the signal is $N \geqslant N_t$. Because the signal is non-periodic, the signal is typically zero-padded and in this case $N \approx 2N_t$ which provides enough sampling frequencies.

The complex exponential term of the Fourier coefficients produces a real and complex term, $F_k = \text{Re}_k + j\text{Im}_k$, which can be separated to produce discrete amplitude A and phase ϕ data:

$$A_k = \sqrt{\text{Re}_k^2 + \text{Im}_k^2}, \tag{4.5.2}$$

$$\phi_k = \text{atan}\left(\frac{\text{Im}_k}{\text{Re}_k}\right). \tag{4.5.3}$$

The resulting one-dimensional amplitude and phase data can be separately reshaped to produce a series of amplitude and phase images.

The amplitude and phase signal produces frequencies ranging from f_1 to f_N in Hz as illustrated in Figure 4.4. The number of discrete frequency samples correspond to the number of discrete time samples N. However, only half of the frequencies needs to be considered as the amplitude and phase images are symmetrical about frequency $f_{N/2}$. The available frequency components do not represent 'real' frequencies but can be calculated directly from the time domain as (Maldague, 2001)

$$f = \frac{n}{N\Delta t} = \frac{n}{N}f_s, \tag{4.5.4}$$

where the minimum available frequency is defined as $f_{min} = f_s/N$ and the maximum available frequency is half the sampling frequency ($f_{max} = f_s/2$), also known as the Nyquist or critical frequency f_c. The available frequencies follow the Nyquist-Shannon sampling theorem where a function can be completely recovered from the sampled data without aliasing provided that the sample frequency f_s is at least twice the maximum available frequency or $f_c \geq 1/2\, f_s$ (Shannon, 1949). This feature of the Fourier transform can be used to evaluate the optimal sampling rate for transient thermography by comparing the maximum available frequency of different camera sampling frequencies. This is further discussed in Chapter 5.
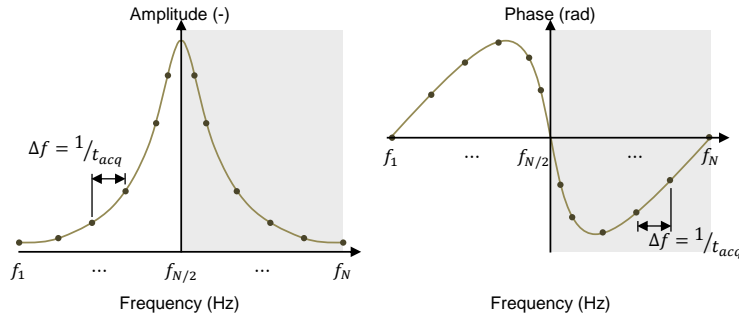
Figure 4.4: Amplitude (left) and phase (right) profiles produced by the Fourier Transform on a pixel's temperature response (adapted from Ibarra-Castanedo, 2005)

Generally the Fourier transform can be performed with little attention to the data, however under-sampling and poorly truncated data has an affect on the performance of the transform in defect estimation methods (Ibarra-Castanedo, 2005). Poorly defining the data truncation window, i.e. the beginning and end of the thermal sequence after all defects have emerged, affects the overall frequency resolution. An increase in error was observed for depth estimation for a smaller truncation window in pulsed thermography.

Zero padding does not improve the frequency resolution but improves the ability to distinguish between adjacent frequencies. The poorly truncated data

suffers from leakage in the frequency spectrum where frequency energy is distributed over a wider frequency range and thus reducing the maximum phase contrast. The FFT computation assumes the signal is periodic. In the case of transient thermography, the signal satisfies the periodic requirement as the signal starts at zero at the beginning of the time window and then rises to some maximum and decays again to zero before the end of the time window. This can be seen as a quarter wave of a periodic signal and presents no sharp changes. However the square pulse temperature response produces a sharp change between the the heating and cooling phases which may reduce the effectiveness of this method.

4.5.2 Wavelet Transform

The wavelet transform is the extension of the Fourier transform with the added benefit of preserving time information, since defect depth is a function of the square root of time. Instead of decomposing the signal by a continuous sinusoidal function, as in Fourier transform, the signal is decomposed through window functions containing a periodic waveform of limited duration, known as a wavelet. The basic wavelet transform can be seen as the convolution of the signal $f(t)$ and daughter wavelet $\psi_{S,Tr}(t)$ defined for a translation factor Tr and a scale factor S:

$$W_f(S, Tr) = \int_{-\infty}^{\infty} f(t) \; \psi^*_{S,Tr}(t) \; \mathrm{d}t, \qquad S, Tr \in \mathbb{R}_{>0} \qquad (4.5.5)$$

where * is the complex conjugate. The daughter wavelet $\psi_{S,Tr}(t)$ is expressed as a scaled and translated replica of a single base wavelet called the mother wavelet $\psi_m(t)$:

$$\psi_{S,Tr}(t) = \frac{1}{\sqrt{|S|}} \; \psi_m \; \left(\frac{t - Tr}{S} \right) \qquad (4.5.6)$$

where the scaling factor S controls the width of the wavelet and the translation factor Tr controls the position of the wavelet along the analysed signal. The wavelet transform permits the use of many different mother wavelets $\psi_m(t)$. The choice of the wavelet should be chosen to best represent the signal or possess a distinct characteristic of the signal. The choice of the wavelet for thermographic analysis is desired to share the characteristic qualities of the Fourier transform and, hence, the complex Morlet wavelet is chosen as the mother wavelet (Zauner et al., 2010; Galmiche & Maldague, 2000; Maldague et al., 2002). The Morlet mother wavelet is defined as

$$\psi(t) = \exp^{(-\jmath\omega_0 t)} \cdot \exp^{\left(-\frac{t^2}{2}\right)}, \qquad (4.5.7)$$

where $\omega_0 = 2\pi f_0$ describes the center frequency (f_0) that defines the initial scale of Morlet wavelet and number of significant oscillations within the win-

dow. Figure 4.5 shows the real and imaginary parts of two daughter wavelets of the complex Morlet wavelet at different scales. The complex Morlet wavelet can be seen to exhibit a symmetric Gaussian envelope of a sinusoidal function with a center frequency illustrated by the dashed sinusoidal function. By altering the scale of the wavelet the center frequency is changed which is the reason the wavelet can decompose the signal into various frequency components. Consequently, amplitude and phase data become available.

More importantly the Morlet wavelet has an optimal joint time-frequency concentration since it has an exponential decay in both the time and frequency domains. This means that there is an equal trade-off between frequency and time support using this wavelet and this support is not observed in many other mother wavelets.
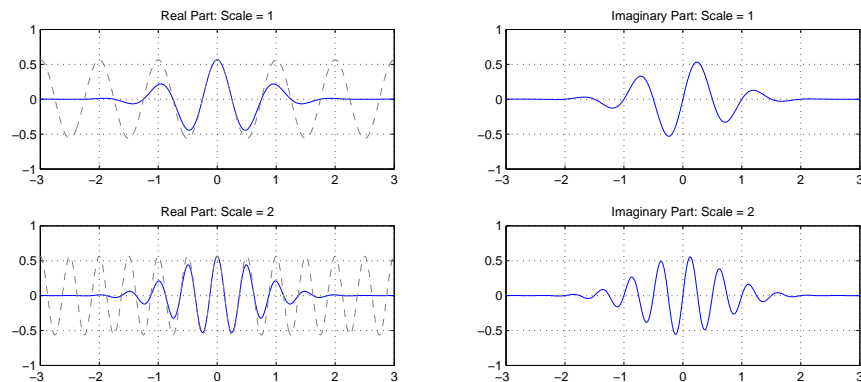
Figure 4.5: Real and imaginary parts of a Morlet wavelet for a change in scale S affecting the center frequency (dashed line)

The output of the wavelet transform produces a tiling in the translation-scale plane that corresponds to a time-frequency plane as seen in Figure 4.6. The entire set of tiles describes the decomposition of a one-dimensional data signal and can be combined to reconstruct the original signal. The relation between wavelet scale S and a pseudo-frequency can be established as (Zauner et al., 2010)

$$f_{pseudo} = \frac{f_0}{S \cdot \Delta t}, \tag{4.5.8}$$

where f_{pseudo} is in Hz corresponding to scale, center frequency and sampling period. The widths and heights of the tiles respectively define the time and frequency resolution (or support) of a wavelet at a given scale S. The width of the windowing function limits both the time and frequency resolution of the tile according to Heisenberg uncertainty principle (Zauner et al., 2010):

$$\Delta t \cdot \Delta \omega \geq \frac{1}{2}, \tag{4.5.9}$$

which describes the joint time-frequency resolution. This principle can be observed as theoretical boxes in Figure 4.6. When the scale S increases in the direction of the arrow in Figure 4.6, the time support is increased, i.e. less repeating tiles, but with a reduction in the frequency resolution. As a result lower frequency components of the thermal response are observed. The opposite is observed for a decrease in scale where the frequency resolution increases and higher frequency components have less time support. This is another interesting feature of the wavelet transform that the high frequency components can be separated as they are assumed to represent noise terms and the signal can be reconstructed without noise. The initial choice ω_0 can be observed to have a similar effect as the scaling factor on frequency and time precision, where a larger ω_0 produces a smaller frequency resolution $\Delta \omega$ and greater uncertainties over translation factor and thus over defect depth. Galmiche & Maldague (2000) selected a center frequency of $\omega_0 = 2$ to reduce uncertainties in depth estimation.
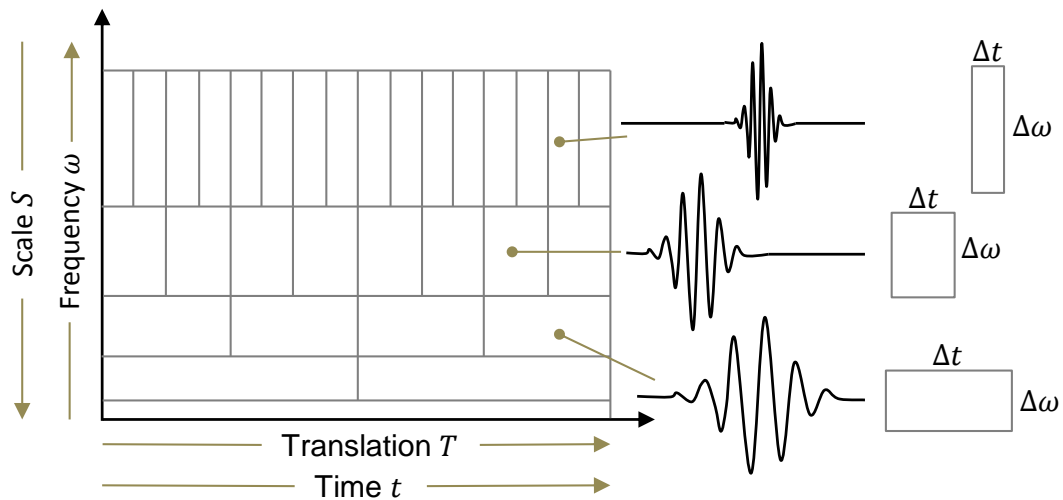
Figure 4.6: Scale-translation plane of a one-dimensional signal depicting the Heisenberg uncertainty relationship between frequency resolution and time resolution

The wavelet transform can be implemented using the fast Fourier transform (FFT) which conveniently handles the time-shift parameter, Tr, and the convolution can efficiently take place in the frequency domain - the convolution theorem states that convolution in time domain corresponds to multiplication in frequency domain. The simple multiplication of the signal and daughter wavelet can be computed and repeated for multiple scales:

$$W_f = \text{IFFT}[\text{FTT}(f(t)) \cdot \text{FFT}(\psi_S(t))] = \text{Re}_S + j\text{Im}_S \qquad (4.5.10)$$

where the translation factor Tr is controlled by the FFT algorithm and reiterated for scales $S > 0$. The inverse fast Fourier transform, IFFT, is performed to produce the real and complex parts to extract the amplitude (Eq. 4.5.2) and phase data (Eq. 4.5.3) for each scale S.

The wavelet transform produces two-dimensional time-scale data from an one-dimensional temperature signal. Even though the fast Fourier transform is relatively efficient, the wavelet transform is computational expensive and requires a considerable number of computations and storage. To reduce the dimensionality and computations, Galmiche & Maldague (2000) proposed using the characteristic time relationship of emerging defect at depth z for determining the optimal scale for each time interval. Using the approximated characteristic time

$$t = \frac{z^2}{\alpha}, \qquad (4.5.11)$$

a time as a function of frequency can be determined by equating the thermal diffusion length $\mu = \sqrt{\frac{2\alpha}{\omega}}$, which is the maximum penetration depth at each frequency, to depth z. This leads to the following relationship:

$$t = \frac{2}{\omega}. \qquad (4.5.12)$$

The scale factor can be defined as the relationship between the center frequency and scale frequency as $S = \omega_0/\omega$. Knowing that the translation factor corresponds to time, the following relation allows the calculation of one scale factor for each translation time

$$S = \frac{\omega_0}{2}Tr. \qquad (4.5.13)$$

The values of S and T are now limited by the actual acquisition time and hence the wavelet transform is (Galmiche & Maldague, 2000):

$$W_f(S, Tr) = \int_{-\infty}^{\infty} f(t) \frac{1}{\sqrt{0.5 \cdot \omega_0 \cdot Tr}} \psi\left(\frac{\frac{t}{Tr} - 1}{0.5 \cdot \omega_0}\right) \, \text{dt} \qquad (4.5.14)$$

4.6 Statistical Techniques

Descriptive statistical methods have been applied to express variability of a data set as images. The methods discussed here are automatic processing methods that require no user input. The statistical methods have been used as an image enhancement method that describes the entire thermal sequence as a single image.

4.6.1   Skewness

Skewness is the third standardized central moment that measures the asymmetry of the probability distribution in a univariate data set. Skewness is defined as (Madruga et al., 2008)

$$\text{skewness}(x_{ij}) = \frac{\sum_{k=1}^{N}(x_k - \mu)^3}{\sigma^3(N_T - 1)}, \tag{4.6.1}$$

where μ and σ are the mean and standard deviation of the temperature response of pixel x_{ij}. The subscripts i,j indicate the process is repeated for all pixel temperature sequences.

4.6.2   Kurtosis

Kurtosis is the fourth standardized moment that measures flatness of the central mean of the probability distribution in a univariate data set. Data sets with high kurtosis tend to have a distinct peak near the mean and low kurtosis have a flat top. Kurtosis is the next moment after skewness defined as (Madruga et al., 2009; Usamentiaga et al., 2012)

$$\text{kurtosis}(x_{ij}) = \frac{\sum_{k=1}^{N}(x_k - \mu)^4}{\sigma^4(N - 1)}. \tag{4.6.2}$$

4.6.3   Matched Filters

There are a few types of matched filtering algorithms but they all are based on the following model (Foy, 2009; Larson, 2011):

$$T_{meas} = \epsilon\, T_{refl} + T_{ideal}\ , \tag{4.6.3}$$

where T_{meas} is the measured temperature response that can be expressed by a temperature response caused by reflectance of defects, T_{refl}, and an ideal temperature response typical of a sound area, T_{ideal}. The strength of the reflected signal is indicated by ϵ. From Equation 4.6.3, the temperature sequences can be written in vector form:

$$\mathbf{x} = \epsilon\, \mathbf{s} + \mathbf{w}\ , \tag{4.6.4}$$

where $\mathbf{x} = T_{meas}$, $\mathbf{s} = T_{refl}$ and $\mathbf{w} = T_{ideal}$. Match filtering techniques require Equation 4.6.4 to be multiplied by a vector $\mathbf{q}$ that maximises the reflectance response and minimizes the sound area response. Hence, vector $\mathbf{q}$ can be determined by the objective function and the constraint

$$\max_{\mathbf{q}} ||\mathbf{q}^T\mathbf{s}||\ \ \text{subject to}\ \ \min_{\mathbf{q}} ||\mathbf{qw}||\ , \tag{4.6.5}$$

where the difference between the various matched filter detectors is defined by the method of determining the objective vector $\mathbf{q}$.

The match filters require the reflectance temperature sequence T_{refl} and ideal temperature sequence T_{ideal} to be known. One can obtain T_{ideal} by manually selecting a sound pixel but unfortunately T_{refl} is unknown. Therefore T_{refl} can be obtained by the following difference between the ideal and measured response assuming ϵ is one (Larson, 2011):

$$T_{refl} = T_{meas} - T_{ideal} \ . \tag{4.6.6}$$

The signal-to-noise ratio was noticed to increase for multiple selections of defective and sound pixels and taking the average respectively to represent T_{refl} and T_{ideal}.

4.6.3.1   Spectral Angle Map

The spectral angle map (SAM) is based on a simple match filter (SMF) where the T_{refl} sequence is used as $\mathbf{q}$. A resulting correlation image between the reflection and measured response is defined as

$$\text{SMF} = \mathbf{s}^{\text{T}} \mathbf{x}_{ij} \ , \tag{4.6.7}$$

where again the subscript i,j indicate the process is repeated for all pixel temperature sequences.

The spectral angle map (SAM) defines the normalized vector magnitudes as

$$\text{SAM}(x_{ij}) = \frac{\mathbf{s}^{\text{T}} \mathbf{x}_{ij}}{\sqrt{\mathbf{s}^{\text{T}}\mathbf{s}}\sqrt{\mathbf{x}_{ij}^{\text{T}}\mathbf{x}_{ij}}} \ . \tag{4.6.8}$$

The SAM image is a similar concept to correlation techniques and describes the cosine angle between the reflectance signal $\mathbf{s}$ and measured signal $\mathbf{x}$.

4.6.3.2   Adaptive Coherence Estimator (ACE)

The adaptive coherence estimator (ACE) is an extension of the clutter matched filter (CMF). The CMF includes the covariance matrix $\mathbf{C}$ of the data set, which incorporates the structural information of the target specimen. The filter is derived from the Likelihood Ratio Test which expresses the probability how many times more likely the data falls under one model than the other (Borokov, 1999). This effectively creates a unique threshold for each pixel. The CMF is defined as

$$\text{CMF} = \mathbf{s}^{\text{T}} \ \mathbf{C}^{-1}\mathbf{x}_{ij}, \tag{4.6.9}$$

where $\mathbf{C}$ is the covariance matrix of the ideal response and is determined for the total number of pixels, $MN = M \times N$:

$$\mathbf{C} = \frac{1}{MN} \sum_{k=1}^{MN} \mathbf{w}_{ij}^{\mathrm{T}} \mathbf{w}_{ij}. \tag{4.6.10}$$

The ACE matched filter for normalized vector magnitudes is

$$\mathrm{ACE}(x_{ij}) = \frac{\mathbf{s}^{\mathrm{T}} \ \mathbf{C}^{-1} \mathbf{x}_{ij}}{\sqrt{\mathbf{s}^{\mathrm{T}} \ \mathbf{C}^{-1} \mathbf{s}} \ \sqrt{\mathbf{x}_{ij}^{\mathrm{T}} \ \mathbf{C}^{-1} \mathbf{x}_{ij}}} \tag{4.6.11}$$

4.6.3.3   t-Statistic & F Statistic

The t-statistic and F statistic methods are common tools used in linear regression and their derivations can be found in literature (Foy, 2009). The definition for the t-statistic is

$$\text{t-stat} = \frac{\mathbf{s}^{\mathrm{T}} \mathbf{C}^{-1} \mathbf{x}_{ij}}{\sqrt{\mathbf{x}_{ij}^{\mathrm{T}} \mathbf{C}^{-1} \mathbf{x}_{ij} - \varrho^2 (\mathbf{s}^{\mathrm{T}} \mathbf{C}^{-1} \mathbf{x}_{ij})^2}} \varrho \sqrt{d-1} \ , \tag{4.6.12}$$

and the F statistic is the square of the t-statistic:

$$\text{Fstat} = \frac{(\mathbf{s}^{\mathrm{T}} \mathbf{C}^{-1} \mathbf{x}_{ij})^2}{\mathbf{x}_{ij}^{\mathrm{T}} \mathbf{C}^{-1} \mathbf{x}_{ij} - \varrho^2 (\mathbf{s}^{\mathrm{T}} \mathbf{C}^{-1} \mathbf{x}_{ij})^2} \varrho(d-1) \ , \tag{4.6.13}$$

where $\varrho = \frac{1}{\sqrt{\mathbf{s}^{T} \mathbf{C}^{-1} \mathbf{s}}}$.

4.7   Principal Component Thermography (PCT)

The Fourier transform is a convenient way of decomposing the thermal signals to the phase-frequency space through a set of sinusoidal basis functions, however transient signals are not periodic signals, particularly in the case of square pulse heating. Sinusoidal functions indeed may not be the best choice for representing either transient heating signals. Principal component thermography (PCT) is based on an eigenvector transform which applies an orthogonal transformation to the thermal inspection data. PCT relies on singular value decomposition (SVD) which closely matches principal component analysis and are both used to reduce high-dimensional data into fewer dimensions while retaining relevant information. The only difference is that there is no need to calculate the covariance matrix which can lead to numerical rounding errors when evaluating the eigenvalues. Eigenvectors can be portrayed as axes along which a linear transformation acts by simple compression or stretching of data on orthogonal axes. Since eigenvalues are orthonormal they represent a complete description of the spatial and temporal variability in the entire thermal sequences as a smaller set of orthogonal statistical modes.

Assuming that the thermal data is a $M \times N$ data matrix $\mathbf{A}$ $(M > N)$, then the SVD can be applied as follows (Rajic, 2002; Marinetti et al., 2004):

$$\mathbf{A} = \mathbf{U}\mathbf{R}\mathbf{V}^{\mathrm{T}} \qquad (4.7.1)$$

where $\mathbf{U}$ is a $M \times N$ matrix , $\mathbf{R}$ is a diagonal $N \times N$ matrix containing the absolute values of the eigenvalues (singular values) of $\mathbf{A}$ and $\mathbf{V}^{\mathrm{T}}$ is an $N \times N$ unitary matrix. In order to apply this to the thermal data-cube matrix, the total number of pixels are rearranged into a single vector to condense the information as a single matrix $\mathbf{A}$ having dimensions $(N_x \cdot N_y) \times N_T$ with time along the columns. Figure 4.7 shows the reorganised matrix $\mathbf{A}$ and the resulting orthogonal matrices produced by the SVD.
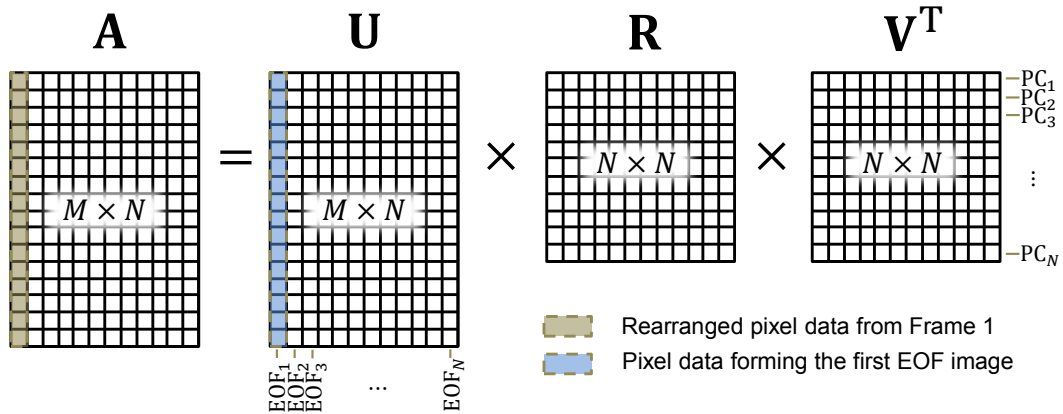
Figure 4.7: Reorganised matrix $\mathbf{A}$ of the thermal sequence and the resulting orthogonal sets using singular value decomposition depicting locations of EOFs and PCs

Each column vector of matrix $\mathbf{A}$ needs to be standardized to ensure uniform variance on a pixel-wise basis

$$\hat{\mathbf{A}}(m, n) = \frac{\mathbf{A}(m, n) - \mu_m}{\sigma_m}, \qquad (4.7.2)$$

where

$$\mu_m = \frac{1}{N} \sum_{n=1}^{N} \mathbf{A}(m, n), \qquad (4.7.3)$$

$$\sigma_m^2 = \frac{1}{N-1} \sum_{n=1}^{N} (\mathbf{A}(m, n) - \mu_n)^2. \qquad (4.7.4)$$

Now the standardized matrix $\hat{\mathbf{A}}$ can be factorized using Equation 4.7.1. Orthogonal statistical modes are present in the columns of $\mathbf{U}$ known as the

empirical orthogonal functions (EOFs) seen in Figure 4.7. The first few EOFs describe the largest variability in the thermal sequence and generally only a few EOFs contain useful images. Furthermore orthogonal statistical modes describing time variations are present in the rows of $\mathbf{V}^{\mathrm{T}}$ known as principal components (PCs). The PCs cannot be displayed as an image but have been proposed to allow defect depth estimation. This requires isolating the defective region and performing SVD separately on each identified defect. Not much work has been performed to show the accuracy of this estimation which is also an inversion method requiring knowledge of thermal diffusivity.

The matrix $\mathbf{U}$ can be rearranged as a three-dimensional matrix to produce a sequence of EOF images. Figure 4.8 illustrates the first four orthogonal statistical modes. The first EOF does not show much variability. However the second and third EOFs describe the most characteristic variability in the thermal data such as defects, vignetting effects and cooling near the sample boundaries. The third EOF remarkably shows the surface wrinkles of the composite plies near the top left corner. The forth EOF shows the introduction of noise and possible heating effects.

(a) EOF 1   (b) EOF 2   (c) EOF 3   (d) EOF 4
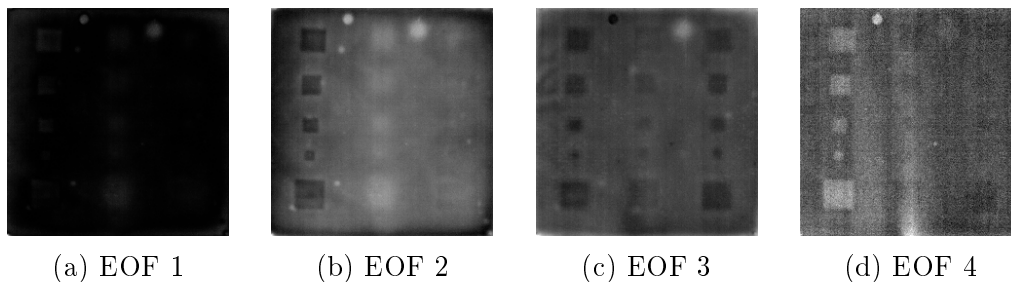
Figure 4.8: Empirical orthogonal functions describing the most variability in the thermal sequence for GFRP106A

4.8 Thermal Signal Reconstruction (TSR)

Thermal signal reconstruction fits a nth order polynomial to a logarithmic sequence of the individual pixel's thermal response. The thermal response can be linearised by transforming to a logarithmic domain before performing a least squares fit (Balageas & Roche, 2014):

$$\ln(\Delta T_{surf}(t)) = \sum_{i=0}^{n} a_i (\ln(t))^i \ . \qquad (4.8.1)$$

By using the semi-infinite solution to characterise the step-heating thermal response, the logarithmic domain can be seen to be valuable in linearising

the data regardless of thermal properties. The logarithm transform of the semi-infinite solution is

$$\ln(\Delta T_{surf}(t)) = \ln\left(\frac{2Q}{e}\right) + \frac{1}{2}\ln\left(\frac{t}{\pi}\right) \tag{4.8.2}$$

where the response will follow a positive $\frac{1}{2}$ slope and $\frac{2Q}{e}$ describes a constant off-set. Because the real temperature response does not practically follow the the semi-infinite response, the choice of order n should be small to avoid unwanted oscillations in the fit but should be large enough to capture the curvature of the data. The data can be reconstructed by taking the exponential of Equation 4.8.1. The reconstructed signal improves defect sensitivity by reducing blurring and increasing signal-to-noise ratio.

Representing the thermal response as a polynomial provides an additional feature of being able to calculate the first and second derivatives. Taking the derivatives of the raw signal is problematic when the signal possesses a high noise content. The derivatives provide an autonomous way of facilitating detection of early time of maximum contrast. The first and second derivatives of the pixel's thermal history in the logarithmic domain is respectively expressed as (Shepard et al., 2003)

$$\frac{d\ln(\Delta T_{surf}(t))}{d\ln(t)} = \sum_{n=0}^{N} na_n\ln(t)^{n-1} \tag{4.8.3}$$

$$\frac{d^2\ln(\Delta T_{surf}(t))}{d\ln(t)^2} = \sum_{n=0}^{N} n(n-1)a_n\ln(t)^{n-2} \tag{4.8.4}$$

where the resulting logarithmic time derivatives are transformed back into linear time domain by the taking the exponential. The derivatives have proven to provide higher defect contrasts and are valuable in depth estimation in pulsed thermography (see section 2.8.2).

4.9   Summary of Algorithms

The processing methods described here have been selected as the best suited for trasient thermographic data. Other processing methods, like filtered thermal contrast (Grys & Minkina, 2010) and partial least squares regression (López et al., 2014(a) & 2014(b)) have shown not to perform well. Many of the methods can be simply applied while others require a level of user interaction. The typical procedures for thermographic data can be first performed with preprocessing methods as suggested in Figure 4.9. These preprocessing methods include subtraction of a pre-flash image to remove partial inhomogeneities already present in the cold images, noise reduction through 3×3 adaptive median and Gaussian low pass filter or application of a smoothing procedure,

such as thermal signal reconstruction or polynomial fitting. The fitting speeds up the subsequent processing methods, even though the fitting method can be computationally expensive at first. Normalization and histogram adjustment have proven to be simple procedures of adjusting the visual threshold.

Choosing a processing method will depend on the thermal data itself and will require trial and error inspections of the processed image. The main goal of these methods are to enhance the overall contrast of defects, especially when the image is contaminated by reflections and non-homogeneous surface effects. Contrast methods are generally used after some preprocessing is performed so a better signal can be achieved. These methods are mainly considered for depth inversion methods where depth is a function of contrast. The derivatives, Fourier transform and wavelet transform offer an alternative depth inversion techniques.

After the image is processed the image can be further enhanced by either multiscale retinex or histogram equalization and followed by pseudocolours and contrast methods. The pseudocolours provide a better description of small variabilities.
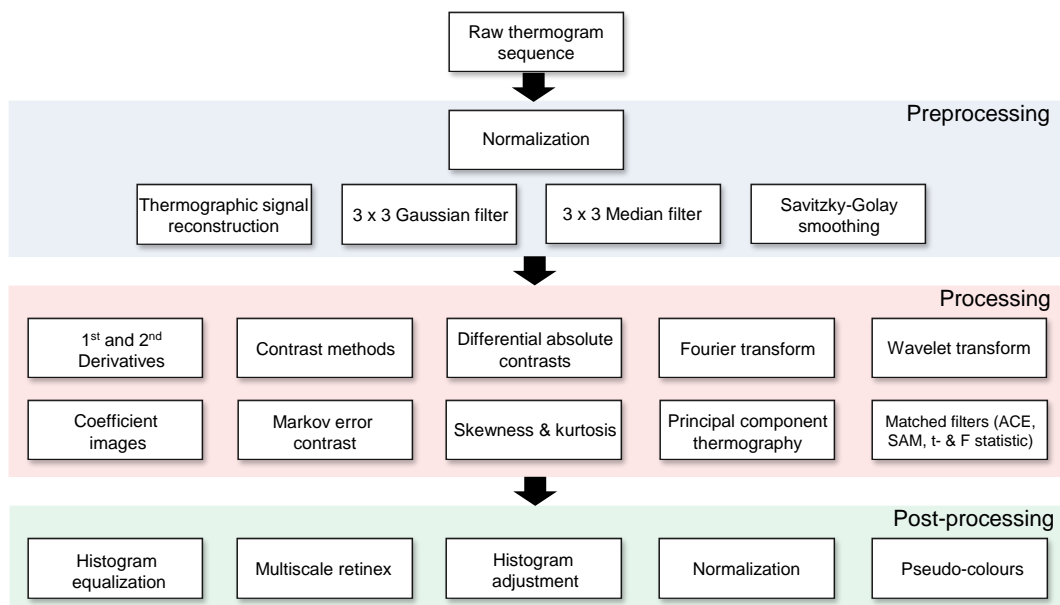

Figure 4.9: The application of signal processing methods at different processing stages

Chapter 5

Results and Discussion

The performance of step and square pulse heating are investigated on the artificial and industrial samples. Optimal heating parameters and a suitable sampling frequency for transient thermography are determined. The difference between the transient regimes are further explored by applying the signal processing methods discussed in Chapter 4. The effectiveness of each processing method will be reviewed at the same time. Furthermore, the chapter will assess the qualitative and quantitative performance of transient thermography in industry. Thermograms and figures discussed in this chapter can be found in Appendix G.

5.1   Inspection with Transient Thermography

The difference between step and square pulse heating has not been documented and there is no clear direction to which method is preferred. Equally the treatment of the heating parameters have not been explored. Therefore the effects of rated power and spectral power of the halogen lights as well as the heating duration is investigated in Appendix F. A suitable camera sampling rate is also determined.

The raw thermograms of the artificial samples are displayed in Appendix G. These thermograms present the best maximum contrast images for both step and square-pulse heating for a total acquisition time of 50 s and a power input of 4000 W.

The polymethyl-methacrylate (PMMA) samples with flat-bottom holes are seen in Figure G.2. They displayed the best overall defect contrast and definition. The different defect depths are easily noticeable by the changes in grayscale intensities. The definition of the defects' periphery is more defined in step heating than for the square-pulse heating thermograms. The dark region seen on the largest defect in the opaque (square) sample represents a breach in the surface material.

The observations are contrasting for the the polytetrafluoroethylene (PTFE)

inclusions seen in Figure G.3. The PTFE inclusions display a weaker signal strength for the same lateral size defect at similar defect depths to that of the flat-bottom hole in the opaque sample. Trapped air around the inclusions, particularly seen in Figures G.3(c-d) and G.3(i-j), display relatively higher contrasts than the PTFE inclusions. The glass fibre samples exhibit the best overall defect detectability of the sub-surface inclusions. The GFRP200 sample, with the largest fibre density (largest fibre diameter), display a slightly poorer contrast. The reduced contrast may be a combination of increased lateral diffusion and the greater interference of heat conducting normal to the surface. The carbon fiber samples present only shallow inclusions at a weaker contrast.

The air-gap delamination thermograms are seen in Figure G.1 with a greater contrast than the PTFE inclusions. Relative differences in the air-gap depth can be noticed in the glass fiber samples. Again the carbon fiber composite produced a weaker contrast for similar delamination depths, however deeper defects, up to 2.5 mm, were better distinguishable.

The results for square pulse heating were similar and sometimes better to that of step thermography, even though the total energy input was approximately a third (16 s) of the maximum energy input produced by step heating.

The flat-bottom holes represent an ideal case in thermography exhibiting a large thermal resistance which exhibits no flow of heat towards the rear surface of the inclusion. It is different to an actual delamination that experiences characteristic edge effects associated with diffusion of heat around the edges to the back surface. The infinitely large thickness and low thermal conductivity provides a high thermal resistance and a greater obstruction to flow compared to the delaminations used in this project. Table 5.1 shows the definite distinction in the thermal resistance of the reviewed artificial flaws. The thickness of the flat-bottom hole in theory extends to infinity but a one meter thickness is used for comparison.

Table 5.1: Thermal resistance of various defects types

| | | Type of Delamination Material | | | |
		PTFE	PTFE	Air	Flat-bottom hole
Thickness	mm	0.25	0.5	0.5	1
Thermal resistance R_d	$m^2\,K\,W^{-1}$	0.001	0.002	0.02084	41.66667

In spite of the low thermal resistances displayed by the PTFE inclusion, most defect positions can be identified after closer scrutiny. Even though the raw transient signal displays a high number of detectable defects, processing steps are still needed to enhance the definition and sizes of the defects. The

raw thermograms also display the effects of surface variability, emissivity and non-uniform heating that mask the low thermal contrast of deeper defects. Signal processing techniques will however not facilitate defect detection beyond experimental detection limits.

5.2   Review of Processing Techniques

Objectively assessing signal processing methods is a problematic task when each algorithm produces a single image or a unique set of images. Moreover a reliable quantitative measurement tool does not exist for thermographic imaging. Traditional photographic measurement tools are not tailored for the image performance criteria of the thermograms. Thermographic criteria can include identifying primitive features, such as defect intensity and noiselessness; logical features, such as clarity and definition of the image; and abstract attributes, such as clarity and significance of the features being enhanced.

Signal-to-noise (SNR) metrics have been the only means of evaluating an algorithms performance in thermography but do not consider other features, such as other variability and defect edge definition.

As a result, the processing methods are visually compared using the maximum contrast image from each processed data set and the original raw thermogram. A summary and the corresponding wall-times of these methods are provided at the end of this chapter in Table 5.3.

5.2.1   Noise Reduction

Temporal noise reduction methods were preferred over spatial noise filters, even though the spatial filters' processing times was a fraction of the time of the temporal methods. The spatial filters included the adaptive median filter and Gaussian low-pass filter. The temporal noise reduction methods that were evaluated include ordinary polynomial fitting, thermal signal reconstruction and Savitzky-Golay filtering. The Savitzky-Golay filter is one-dimensional convolution filter that can be applied to any one-dimensional signal. It provides noise-smoothing and an estimate of signal derivatives. The results of these methods were similar, although the thermal signal reconstruction demonstrated a faster execution time (see Table 5.3).

5.2.2   Contrast

The standard contrast methods were found to be fairly effective for uniformly heated samples and defects that produced high thermal contrasts. These methods did not perform well for the samples that contained high surface variability or PTFE inclusions. The images for absolute, normalized, running and standard contrast for both transient regimes are presented in Figure G.4. The

contrast images of the square pulse regime displayed the best results showing a better contrast for the deepest delamination not initially detectable in the raw thermogram. The contrast methods were designed to reduce emissivity and surface variations, however these features were still predominately seen in the contrast images.

5.2.3 Differential Absolute Contrast

The differential images of the differential absolute contrast (DAC) and interpolated differential absolute contrast (IDAC) showed slight success in removing non-uniform heating. These methods were only appropriate for step heating as they were formulated on the one-dimensional step heating model. A thermogram is displayed for relatively early times and at later times for both DAC and IDAC in Figure G.5. The thermograms were unfortunately contaminated with a large amount of noise but the defects became more pronounced against the background. Small dark anomalies, which were identified to be air bubbles, are more noticeable in the processed images. At later times the defect contrast was questionable but the thermograms displayed a more uniform sound region. The poor performance of both methods was anticipated as the one dimensional model is only valid for early times after heating and for homogeneous materials.

5.2.4 Skewness & Kurtosis

The skewness and kurtosis images have proved to be beneficial in enhancing defect contrast and highlighting small anomalies within the composite. These methods can be applied to any thermal sequence regardless of the shape of the heating profile. The resulting images are displayed in Figure G.6. The definition and shape of shallow defects is well defined. The kurtosis image displayed more defects for both regimes but the definition of the second deepest defect column is less pronounced than the deepest defect column located in the center. It is unclear from the original image why this is the case. All images produced relatively uniform background pixels and square pulse thermography benefited the most from this method. The darker perimeter seen near the sample's edges highlights ply thickness changes (Figure G.6(f)) and possible heat losses.

5.2.5 Matched Filters

The matched filters performed moderately well for most composite samples. Surface variability and emissivity was still prevalent in the processed thermograms of the carbon fibre composites. The four matched filters include the adaptive coherence estimate (ACE), spectral angle map (SAM), the t- and F statistic. The results are displayed in Figure G.7 for the same GFRP106A

sample previously used in the skewness and kurtosis comparison. In these images the second deepest column is more pronounced and overall the defects are less blurred compared to that in the skewness and kurtosis thermograms. However, the center defects are not seen in the t- or F statistic images.

Each filter produced similar results for both heating regimes. Only the ACE and SAM filters effectively identified all defects. The ACE and SAM filters applied to square pulse regime highlight small anomalies and air voids trapped at different ply depths. Close inspection of the sample confirmed the presence of these voids. In contrast, surface variability was more evident in t- and F statistic thermograms. A surface scratch near the top right corner coinciding with the signal of the back-wall washer became visible in these images. It was initially not visible in the digital image or raw thermogram.

All results showed a fairly uniform background and the presence of a vignetting effect on the sample periphery matched the similar effects seen in the statistical moments. A increase in contrast was observed in the matched filters when selecting deeper defect pixels.

5.2.6 Principal Component Thermography

Principal component thermography (PCT) performed effectively for all samples and slightly better for square pulse thermal data. Selecting a particular empirical orthogonal function (EOF) allowed one to inspect different variabilities in the sequence. Most of the variability in the thermal set is contained in the first few EOFs and the second EOF accounted for the highest variance that is associated with the thermal contrast of the defects.

The second EOF is presented in Figure G.8 for the CFRP 200B composite and was able to enhance the weak contrast produced by the 0.25 mm thick PTFE inclusion. PCT was able to increase defect definition as well as increase the contrast of other variabilities, such as ply features and surface finish.

The change in the acquisition time of the thermal sequence was observed to have an effect on the EOFs' variability. The change of acquisition time is shown in Figure G.9. When decreasing the total acquisition time of the data the contrast of the defects improved for the second EOF. Decreasing the total time however reduced the number of EOFs that contained meaningful information.

5.2.7 Markov Error Contrast

The Markov error contrast (MEC) did not perform as well as reported for pulsed thermography data. Figure G.10 illustrates the MEC images for carbon and glass fibre composites with air-gap delaminations (CFRP 200DEL and GFRP 200DEL). The MEC performed poorly on samples with PTFE inclusions and particularly badly for the carbon fibre samples that exhibited weaker contrasts. The MEC image for the CFRP 200DEL showed a slight increase in

contrast for the deepest (middle) delamination. The shallow delamination's lateral size was notably larger than the original raw image. The MEC image for the GFRP200DEL produced a more uniform background when a colourmap is applied. This was consistently observed for all glass fibre composite samples.

5.2.8 Thermal Signal Reconstruction

The thermal signal reconstruction (TSR) technique presents favourable performance in pulsed thermography, however TSR has proven to not offer the same benefits for transient thermography. The few benefits of using the TSR method include the overall reduction of noise, efficient storage and processing of a few polynomial coefficients. The effectiveness of each algorithm increased when preprocessed by the TSR method. Even though the TSR method has a relatively long computational time, the speed of additional processing afterwards increased.

The TSR polynomial fit is observed for a step heating case in Figure 5.1 for a carbon fibre sample (CRFP200A). The carbon fibre samples exhibit a faster thermal diffusivity than the other reviewed samples. The polynomial is fitted using a 5th order polynomial to the temperature response of a defective pixel corresponding to the shallowest and largest lateral size defect. For completeness, a sound pixel is also plotted. The surface temperature of the shallowest and largest defect experiences a faster rate of change than deeper and small defects. The enlarged section plots reveal a better description of the fit and the discontinuities in the recorded signal. The discontinuities are a result of the infrared camera pausing during the recording to automatically recalibrate the sensor. This is observed in most of the thermal sequences but was considered to have negligible impact on the results.

The polynomial fit is not performed entirely on the square heating response as the temperature curve possess a sharp point between the heating and cooling phase. The TSR method can however be individually applied to each phase of the square pulse response. For the cooling phase, which is analogous to the decay of pulsed thermography, the TSR method was observed to improve the signal-to-noise ratio of the raw thermal sequence as seen in Figure G.11. Alternatively, the Savitzky-Golay filter can be used to reduce the temporal noise of the entire response with no added benefit of data reduction through coefficient images.

Furthermore, the coefficient images produced by TSR do not possess any noticeable enhancement over the raw thermograms as shown in Figure G.13. The coefficient images are highly contaminated with noise and the defect definitions are less noticeable. The decay coefficients of the square pulse response are not shown as they display no significant difference to the coefficients of the step response. Nevertheless a coloured image was constructed using the best three coefficient images that describe the most visible defects. The three coefficients were arranged as the red, blue and green channels of an RGB image

using the best RGB-colour combination. The RGB image can be constructed by

$$I_{RGB}(x, y) = \text{concatenate}(R_a, G_a, B_a), \qquad (5.2.1)$$

where R_a, G_a and B_a represent the three polynomial coefficients (a_n) that defines the red, blue and green colour channels. The combination of channel intensities create an unique colour for a particular depth, where the depth can be estimated through an inversion technique. Pixels that share common depths should have similar coefficients, and should produce a unique colour for a particular depth. Figure G.12 displays the RGB images for step and the decay of square pulse coefficients. A slight change in colour is observed for different depths but the reconstructed RGB image is considered to be worse than the raw signal. The unique image of the square pulse coefficients shows a slight improvement to the visualization of defect depth.
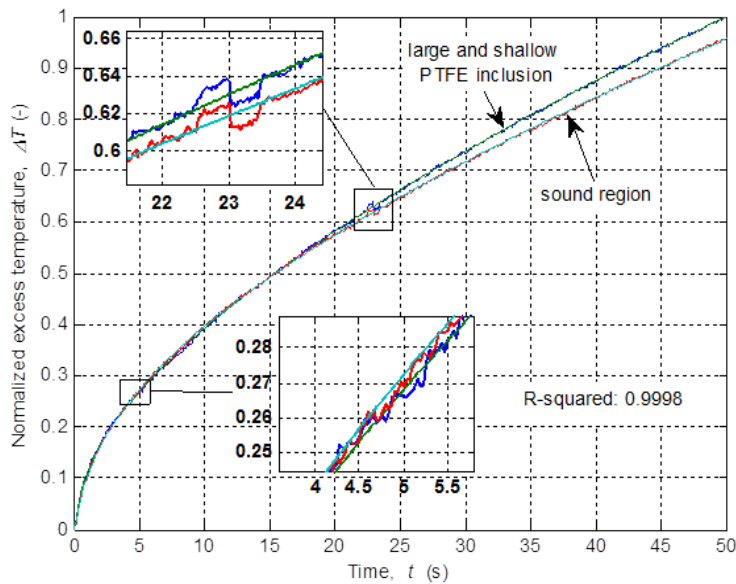

Figure 5.1: A 5th order polynomial fit using TSR method on a carbon sample with PTFE inclusions

5.2.9 Fourier Transform

The amplitude and phase images of the Fourier transform proved to be an effective method for defect enhancement in step thermography and moderately effective for square pulse thermography. Figure G.15 and G.16 present the amplitude and phase images for both transient regimes on the CFRP200A sample. For step heating, the phase images revealed deeper defects at lower frequencies and a better description of the shallow defects at slightly higher

frequencies. The lower frequencies where preferred as they contained most of the sub-surface defects in a single image. Higher frequency images mostly described noise. The phase images enhanced surface and internal variabilities. The amplitude images provide some enhancement features by being less affected by surface variability.

The Fourier transform on a square pulse response is less favourable as the defect definition is poorer than step and the second deepest defects are not visible in the phase images. In addition the phase images offer less detail which may be a consequence of the non-periodic nature of the signal containing a sharp peak. The amplitude images proved to showed better qualities for square pulse heating.

The effect of sampling frequency is observed on the Fourier transform for flat-bottom holes in the opaque PMMA sample. Reducing the sampling frequency f_s from 30 to 5 Hz produced a slight drop in defect contrast as revealed by the phase difference plot in Figure G.14. The phase difference defines the difference in phase between a defective and non-defective region. The frequency position describes the image containing those frequencies. The contrast is the highest for the second and third available frequency (0.04 Hz and 0.06 Hz). The slight drop in frequency also confirms that choosing a sampling rate between 5-30 Hz is suitable in capturing the transient behaviour of the target surface. The choice of a 1 Hz sampling frequency reveals a change in phase information shifting to lower frequencies that further highlights that the data may be undersampled.

5.2.10   Wavelet Transform

The wavelet transform proved to be effective in revealing most defects in the samples for both heating regimes. Again the phase images proved to be preferred over the amplitude image. The phase images allowed the inspection of defects emerging over time while sharing the defect enhancement qualities of the Fourier transform's phase image. The amplitude and phase images of the wavelet transform are seen in Figure G.17 for step heating and Figure G.18 for square pulse heating. The amplitude images show no improvement to the raw images.

5.2.11   Spatial Image Enhancement

The effectiveness of histogram equalization on thermograms is shown in Figure G.19. The appropriate application of the histogram equalization method depends on the image and the purpose of using the method. Admittedly, the multiscale retinex method has proven to be more suitable for the enhancement of both raw and processed thermograms. Figure G.20 displays the multiscale retinex method on raw thermograms.

5.3   Analysis of Industry samples

Samples from industry where inspected using step and square pulse thermography. The thermal data was preprocessed with thermal signal reconstruction before other processing methods were applied. After the experimental findings were made, the actual material flaws were revealed. Some of the main findings are discussed below.

The first sample describes a 1.5 mm thick, two-ply thermoplastic laminate that was heat bonded. The sample was provided to investigate a possible bondline failure in a new technique of heat-joining two plastic plies together. Figure G.21 presents the digital image and processed thermograms of the front and rear surface of the thermoplastic laminate. Interestingly the arrow in Figure G.21(a) and G.21(e) shows a line drawn by a permanent marker on the front surface. On inspection of the rear surface the line was partially observed. The label positioned on the rear surface is similarly seen in the thermogram of the front side as shown by a line in Figure G.21(b) and G.21(d). In addition, the thermogram showed some variability in the front and back thermograms using the adaptive coherence estimator (ACE) matched filter. A particular region of interest is marked by a dashed rectangle on both thermograms. By further inspection using the principal component thermography technique, the same features were identified. The cause of variability is unknown as the cropped thermograms of the front and back side do not display identical features.

The effect of core crushing was investigated in the third sample set. The sample set consisted of a two ply glass-epoxy laminate on five plies of uni-directional carbon-epoxy forming the skin of a foam sandwich composite. The core was made of 10 mm thick polyethylene terephthalate (PET) foam. The samples again represent a control and a sample deformed by a hammer, which are presented in Figure G.22. There is no distinct indication of any deformation between the two samples, which is displayed by the best frequency images of step and square pulse heating using the Fourier transform. After the images were post-processed with contrast-limited adaptive histogram equalization (CLAHE), the thermograms revealed the boundaries of the foam panels. In particular, the deformed sample thermogram shows a brick-like pattern (Figure G.22(e)). The square pulse heating method presents a better description of the foam slabs using the Fourier transform.

A honeycomb sandwich with potted inserts is inspected in Figure G.23. The front and rear surface is inspected with both transient regimes and various processing methods are applied. The sandwich composite is inspected for bondline failure between the potted insert and surrounding material. Both the front and rear thermograms depict the uneven distribution of the potting compound, which equally shows the variability in the reamed holes. The only conclusion that can be made is the pattern produced by the potting compound and the insert. Both sides display the same thermal pattern suggesting that the potting resin extents through the entire core to both ply skins.

The next sample evaluates the integrity of a thick honeycomb sandwich spliced to Tufnol®. The resulting thermograms are seen in Figure G.24 using the first empirical orthogonal function in principal component thermography. The definition of the bondline and other variability in the spliced Tufnol® is evaluated for both heating regimes. There is a clear indication that step heating produces a better precision of detail, whereas square pulse heating produces a more smoothed feature but with an increase in contrast. The variability in the thermograms are consistent to the digital image. One may argue that the variability in the composite can be observed without the need of thermography, however this would not be the case if an opaque resin is used. This comparison is intended to show the accuracy of transient thermography.

A 2.3 mm thick sample was created that exhibited voids throughout the material. Figure G.25 displays the front and rear side of the ten-ply glass-phenolic laminate. The thermograms represent the best empirical orthogonal function (EOF) for the step and square pulse heating methods that are able to detect these voids. Two relatively large voids are seen on the left hand-side of the Figure G.25(e) and Figure G.25(f), which also corresponds to the right-hand side voids seen in Figure G.25(c). Other smaller voids are seen in all the thermograms as different grayscale intensities, suggesting that the anomaly is a different type of inclusion or at another depth. The smallest detectable defect is approximately 1 mm wide - a spatial resolution limit of the infrared camera. This time the inclusions and voids are not visible in the digital images. Another large anomaly is evident on the far right hand-side of Figure G.25(b) and Figure G.25(c), stretching from the top to bottom in the front surface thermograms.

Lastly, four samples were obtained from different regions of a rejected Spaceflex product that experienced a loss in vacuum during curing. The glass-sandwich composites can be seen in Figures G.26 to G.29. Figure G.26(b) illustrates the ability to detect anomalies and expose subsurface ply features with discernible detail with the wavelet transform. Instead of selecting an image from the large data set of the wavelet transform the use of the skewness processing method is able to display the variability from the data set as a signal image. The skewness image is presented as Figure G.26(c). Figure G.27 to Figure G.29 display large variability of resin build-up throughout the skin plies. This is expected for composites that are not properly vaccum-sealed. Most of the processed thermograms display small, dark variabilities that can be regarded as resin build-up in the honeycomb cells. Lighter circular regions in Figure G.28 may be due to resin deficiency, or air-voids. The dark region near the bottom of this figure shows a possible accumulation of resin.

There is an obvious uncertainty in characterising defect flaw types of some of the anomalies. An anomaly may produce different grayscale intensities depending on its material properties or thickness. Despite these uncertainties surface, sub-surface, ply and core variability was clearly distinguishable. The flaws in the samples were unfortunately limited to small variability in this study

and no delaminations were identified. The detected lateral size of anomalies in the thermograms also matched closely to the variability observed in some of the digital images.

5.4 Defect Characterization

Defect characterization has been a popular topic in question for thermography. The convenience of thermograms provide straightforward descriptions of lateral size but depth estimation techniques have been limited to inversion methods.

5.4.1 Lateral Defect Sizing

The lateral size and shape of a defect can be estimated directly from the thermogram by knowing a reference size, such as the size of the sample's width or an adhesive label. The concern in pulse thermography is that the observed defect's definition becomes more blurred with time and no distinct defect periphery can be observed. For step thermography this was found to not be the case, but similar blur effects are seen in the cooling phase of square-pulse thermography. As a consequence step thermography is preferred in lateral size estimation.

The shear magnitude method is presented as an automatic estimation of lateral size. This method eliminates the biases in the selection of a defect periphery. This method requires the shifting of a thermogram by a few pixels in any direction over a non-shifted copy of the thermogram. Figure 5.2 represents a sheared thermogram shifted by three pixels both vertically and horizontally. The shifted image produces a maximum and a minimum peak close to the perceived defect edges and the defect size can be determined by measuring the opposite peaks as illustrated in Figure 5.2. The shifting of the image both laterally and horizontally allows one to measure either the width or height of the defect. A pixel-shift factor of three was selected as it produced the best representation of defect lateral size.
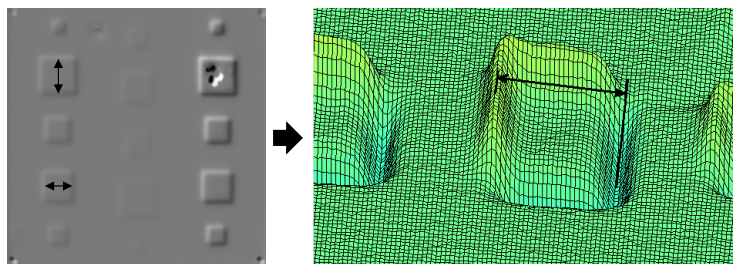

Figure 5.2: Shear magnitude image (left) and corresponding surface plot (right) representing the width between peaks

The shearing image method was iterated over the entire sequence of the opaque PMMA sample to produce a plot of measured pixel length over time as seen in Figure 5.3(a). This figure shows for early times the defect has not yet emerged and only after ten seconds does the contrast of the defect become more pronounced in the thermal sequence. After 30 seconds the signal-to-noise ratio has improved and the uncertainty in defect sizes has reduced. To demonstrate the reliability of this method on composite materials, the shear magnitude image is repeated for the entire sequence of the GFRP200DEL sample, seen in Figure 5.3(b). The composite sample revealed that the spread of the measured defect size was much larger than that of the PMMA sample. The shear magnitude method was found to be a problem in the composite materials that exhibited other inclusions and weaker contrasts, even after processing.

A simple line measurement on the thermograms was found to be more useful than the shear magnitude method. The thermograms were processed with the wavelet transform and post-processed with the multiscale retinex method before the lateral size was measured. The lateral size measurements and error in the actual defect size can be seen in Table G.1. Lateral size measurement errors were below 20 % for high contrast defects and below 40 % for low contrast or deeper defects. The large errors can be attributed to the spatial resolution of the camera, user bias and poor thermal contrast of particular samples, i.e. clear PMMA. Nevertheless for most of the estimations, the error was relatively smaller. The reference adhesive label was used to calibrate the width of a pixel.
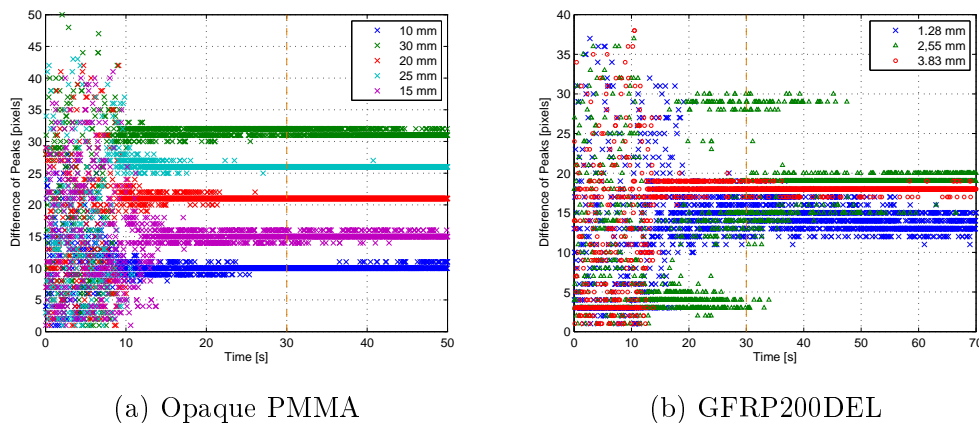

(a) Opaque PMMA

(b) GFRP200DEL

Figure 5.3: Measured difference between peaks for a (a) 2 millimeter deep flat-bottom holes with lateral sizes of 10-30 mm in the PMMA sample and (b) a 15 mm wide air-gap delamination at depths 1.28, 2.55 and 3.83 mm

5.4.2 Depth Estimation

The main methods in literature to estimate defect depth have been performed through the use of an inversion method. The inversion method is usually formulated by the inspection of a calibration sample that exhibits three or more defects at known depths that share similar thickness and thermal properties. The common use of inversion methods highlight that there is no intrinsic feature of heat flow that can be exploited when estimating an unknown defect.

The application of depth inversion methods is an inherent problem for samples that pose variable and unpredictable defects. Firstly, the calibration samples cannot be practical employed in industry to model the variability when the depth of the anomalies are clearly unknown. Secondly, there remains some uncertainty in describing the exact flaw types that are observed, such as an inclusion or delamination. Thirdly, most of the industrial samples reviewed are relativity thin (1 - 15 ply thick), which argues the fact whether exact depth information is indeed necessary.

Figure 5.4 illustrates the relative contrasts between flaws with different thermal resistances. The thermal contrast of an air-void and PTFE inclusion are located at approximately the same depth, yet they are seen to display a unique thermal response. Even if the air-gaps presented in Figure 5.4 are deeper or have a larger thickness than the PTFE inclusion, there is still no correlation of depth seen between the two defects' thermal response. This comparison highlights that even if the defects are located at the same depth, a change in thickness, thermal properties or depth of the inclusion will display a unique thermal response. Hence a defect with a higher thermal resistance will produce a higher contrast which will be observed at an earlier time than a defect with a low thermal resistance.
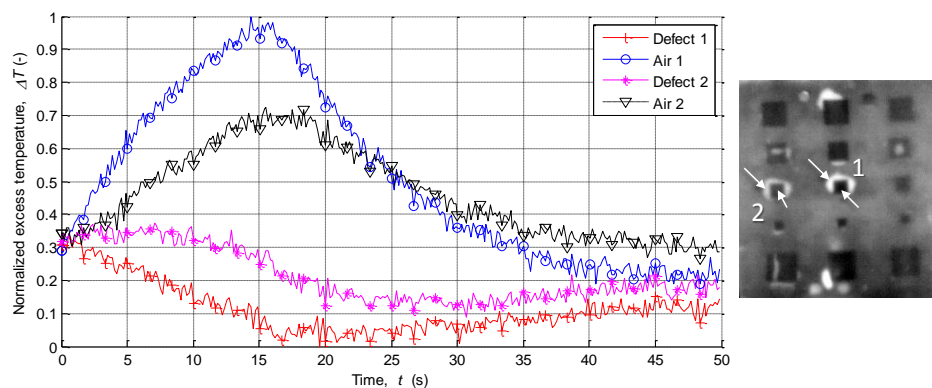

Figure 5.4: Normalized contrast for GFRP106B sample for two PTFE and air-gaps inclusions

In order to determine the depth of a defect without an inversion method, one would need to determine the initial time that the heat has reached the

defect. At this time the defect material properties and size is considered to have no effect on the heat flow. However since the surface can only be observed and the surface does not display this information yet, the heat needs to travel back towards the surface. The degree of the heat reflected back towards the surface is dependant on the thermal resistance ratio of the host material and the inclusion (recall the thermal mismatch factor). The speed at which the defect induces a contrast on the surface of the sample is a function of the amount of heat reflected, the travelling distance defined by the depth and the attenuation of the heat flow by lateral diffusion.

5.5 Summary

Transient thermography has shown to display a fairly accurate representation of low thermal resistance anomalies in both artificial and industrial samples. Step thermography displays a better representation of flaws while square pulse thermography allows weaker thermal contrasts to gain higher levels. Square pulse heating is preferred for the inspection of deeper defects and low emissivity materials. The defect depths that were detectable in the artificial samples after signal processing are provided in Table 5.2. The maximum detectable depth in many of the artificial samples was limited to the deepest defect created in the sample.

Table 5.2: Maximum detectable defect depth in the artificial samples

	Clear PMMA	Opaque PMMA	CRFP200DEL	GFRP200	GFRP106A	GFRP200DEL	CFRP200A	GFRP106B	CRFP200B
Depth (mm)	$7^\dagger$	$5^\dagger$	$4.9^\dagger$	$4^\dagger$	$3.9^\dagger$	$3.8^\dagger$	$2.7^\dagger$	1.8	1.4

$\dagger$ indicates the deepest defect in the material has been detected

Transient thermography offers a method of highlighting exact locations of degradation or variability in composite laminates in industry. Exact details of the type of flaw, such as a delamination, inclusion or air-void, cannot be determined at this point. However differences in signal intensities may help differentiate between differences in flaw types, for example the air-voids are seen to produce a higher signal than the resin build-up.

Processing methods have shown to be useful in enhancing low contrast defects and variability in the thermal sequence. Particular methods have reduced data redundancy by displayed the entire thermal sequence as a smaller set of images or image. Finally, a summary of the processing methods is provided in Table 5.3.

Table 5.3: Summary of reviewed processing methods

Processing Technique[1]	Effectiveness Rating[2]	Execution Time (s)	Comments
Savitzky-Golay Filter	1	786.26	Best technique that can denoise the square pulse response.
Dynamic Thermal Tomography	1	168.50	Only practical for square pulse thermography.
Matched Filters (SAM, ACE, t/F stat)	2	107.57	The selection of defective and non-defective pixels affects effectiveness.
Fourier Transform	3	94.67	Performs well for all samples.
Polynomial Fitting	1	89.76	An increased computational expense than thermal signal reconstruction.
Principle Component Thermography	3	80.25	Enhances all features and variability. Performs effectively with multiscale retinex.
Wavelet Transform	3	69.15	Displays different flaw variabilities in each frame.
2nd Derivative	0	59.80	No enhancement in contrast is observed.
Multiscale Retinex	3	57.31	Consistently performs well as a post-processing technique and reduces illumination effects.
TSR	2	52.76	Can be used as preprocessing method and data can be stored efficiently.
Skewness & Kurtosis	2	21.85	Presents the entire variability of the sequence as a single image.
1st derivative	0	9.78	No contrast enhancement increase is observed.
Markov Error Constant	1	8.21	Generally has a limited performance on composites.
Absolute Contrast	1	1.05	Requires high signal-to-noise ratios and uniform properties. Rather used as postprocessor.
Running Contrast	1	0.96	Requires high signal-to-noise ratios, does not remove surface variability.
Modified Differential Absolute Contrast	1	0.78	No increase is observed than classical differential absolute contrast. Requires thermal diffusivity and thickness parameters.
Normalized Contrast	2	0.69	Best performing contrast method on high signal-to-noise ratios.
Standard Contrast	1	0.67	Requires high signal-to-noise ratios.
Differential Absolute Contrast	1	0.63	Performs poorly for composites, however the sound region is fairly flat.
Histogram Equalization	1	1.9 - 0.05	Limited visual enhancement technique.

[1] Performed for 1500 frames with a total number of 76800 pixels per frame

[2] User Rating: 3 - Highly Recommended, 2 - Recommended, 1 - Neutral and 0 - Not Recommended

Chapter 6

Conclusion and Recommendations

The main aim of this work reviewed two transient thermography methods, step and square-pulse heating, for their application into industry as a simple NDT method for the inspection of composites. The effects of the heating parameters are firstly outlined before the performance and limitations of transient thermography are concluded. The signal processing methods are summarized and significant contributions are highlighted. To conclude, recommendations for future work are proposed.

6.1   Optical Heating Setup

An affordable heating system was evaluated for transient thermography. The investigations confirmed that the basic apparatus can include an entry-level infrared camera with a maximum sampling frequency of 15 Hz and a spatial resolution matching the smallest detectable feature; and the use of two common halogen floodlights with a power rating greater than 1000 W. The following optimal heating parameters are recommended:

Heating Setup: The halogen lights used in transient heating provide a wide absorption spectrum for many target materials that have diverse absorption bands. In addition, the ability to control the maximum heating power and the many varieties of halogen lamps allow the design of the heating system to be customized for inspection of curved geometry and large surfaces. Placing the halogen lamps to the side of the sample demonstrated the best method of mitigating the adverse reflections caused by heating system. A glass pane of 5 mm thick proved to be beneficial in removing infrared reflections from all environmental sources.

Heating Power: Four tungsten-halogen lamps producing a total power of 4000 W was seen to produce enough heat for short inspection times. Caution however must be taken when heating heat-sensitive items.

Heating Duration: A total duration of 16 s or greater was sufficient in detecting low resistance defects in fibre-reinforced composites. Long duration times did not increase maximum depth limit and defect visibility was seen to become worse for the polytetrafluoroethylene (PTFE) inclusions in the carbon fibre reinforced polymer (CRFP) samples.

An increase in both heating power and duration was observed to have a proportional effect on the thermal contrast for a limited depth detection range. The depth detection range was defined by the material's thermal diffusivity and is more constrained for higher diffusivity materials, such as CRFP.

6.2 Performance of Transient Thermography

Transient thermography is proposed as an effective alternative to other popular thermographic inspection methods, such as pulsed and lock-in thermography. The short inspection times of 50 s demonstrated better inspection times opposed to lock-in. The relatively high contrast of the defects in the raw thermograms highlights a possible advantage over pulsed thermography.

Experimental procedures were performed to evaluate defect detection limits of flat-bottom holes in Plexiglas® and delaminations in a variety of glass and carbon fibre laminates (GFRP & CFRP). This work evaluated the differences between contacting and fully-separated delaminations, which were respectively simulated by a PTFE inclusion and an air-gap. The PTFE delamination that exhibited the lowest thermal resitance was shown to produce a weaker thermal contrast compared to both the air-gap and flat-bottom hole. Detection limits were clearly limited to the host material's thermal diffusivity, thickness and thermal material properties of the inclusion.

The combination of transient methods and the advanced signal processing techniques have been able to detect defects depths up to 7 mm for flat-bottom holes in clear Plexiglas® and up to 5 mm in both CRFP and GRFP composites for 0.5 mm thick PTFE inclusions. In contrast, the depth detection limit of pulsed thermography reported up to 6.5 mm in Plexiglas® (Ishikawa et al., 2013; Ibarra-Castanedo & Maldague, 2004c) and 1 mm in FRP composites (Benítez et al. 2008; Hidalgo-Gato et al. 2013; Theodorakeas et al., 2014).

Overall, all defects in the GFRP samples were identified. Only a few defects became observable for the CFRP samples exhibiting similar defect depths. Interestingly the inspection of "glass/epoxy samples has always been a challenge [in thermography]" (Ghadermazi et al., 2015). This concludes that transient thermography performs better for materials with low thermal diffusivity.

The measured lateral size was consistently stable for step thermography with errors below 40 %. This accounts for the user-selection bias, camera's limited optical resolution and the low defect contrast. Furthermore, there is no

comparative difference in error between circular and square defects. A higher fibre-density composite also experienced a slightly weaker defect contrast.

Step and square pulse heating were seen to present particular advantages towards one another:

- step thermography showed better defect definition and contrast

- square-pulse thermography offers similar defect detectability to step thermography for a lower energy input and relatively lower surface temperature, and

- square pulse thermography was advantageous in the detection of weaker defects, or lower emissivity samples, that displayed higher contrasts during the thermal decay.

6.3 Processing Methods

The thermal signal in thermography is well-known to be weak and requires a level of pre- or post-processing. In the same way, the effects of non-uniform heating and emissivity are a common problem that reduces defect detection.

Various traditional and advanced signal processing methods were reviewed. The processing methods that showed best overall performance for transient thermography included multiscale retinex, principal component thermography and the wavelet transform. Multiscale retinex showed to be an effective method for both pre- and post-processing. The matched filters and contrast methods all required some user input for the optimal selection of defective or sound zones. The statistical and thermal signal reconstruction methods were valuable in reducing the redundancy in the thermal data and the storage requirements. Popular processing techniques used in pulsed thermography did not perform well for transient thermography, such as the derivative images, polynomial coefficients, Markov error contrast and the differential absolute contrast methods.

6.4 Limitations

A major problem in thermography is that there are no international standards or guidelines when performing an inspection. The general conception in thermography is that depth information can be determined. However the current inversion methods proposed for depth estimation of flaws are proven to be not practical for real delaminations exhibiting low thermal resistances. The fundamental problem in thermographic inspection is that structural information is derived from the diffusion of heat that is influenced by finite defect size, thickness and thermal properties. There is also no intrinsic feature of heat flow that can be used to define a reference depth.

6.5   Industrial Application

In summary, transient thermography has shown to be a straightforward non-destructive testing method for its use in industry for various polymer composites. It provides a clear description of the location of variability that requires little or no signal interpretation. Quantitative measurements of defect size has shown to be accurate and can be immediately approximated in the thermograms. Transient thermography has the ability to identify resin variation, core structural geometry, and ply information in the industrial samples and anomalies as small as 1 mm wide was identified. The structural integrity of sandwich composites that present core-shear and impact damage have displayed unclear results. Knowing the depth of defects can be considered less critical than the lateral size of a defect when thermography is limited to inspection of relatively thin composites.

6.6   Significant Contributions

The relevant contributions described in this research are summarized.

1. Displayed the significant potential that transient thermography has for the detection of low resistance defects.

2. Demonstrated the successes and limitations of transient thermography for the application in industry

3. Defined optimal heating parameters and sampling frequency

4. Showed that explicit detail of variability in industrial samples for defects as small as 1 mm wide can be detected.

5. Developed an opensource thermographic processing software to aid in future inspections of pulsed and transient thermography.

6. Assessed current and new processing methods on transient thermography data applied to both artificial and industrial samples.

6.7   Future Recommendations

Future recommendations may investigate alternative transient heating methods, such as ultrasonic or microwave heating. A better infrared camera could be deployed to display better spatial accuracy of smaller anomalies.

An investigation to define the limitations of transient thermography will be beneficial. The defect detectable limit can be evaluated for smaller and thinner inclusions made from a variety of materials. Further studies should investigate the application of transient thermography in other engineering fields and materials.

Appendices

Appendix A

Optical Considerations

Energy transfer and conversion takes place throughout different stages of optical thermography. At the same time the available energy is continuously being attenuated through absorption in mediums, such as air and solids and dispersed by photo-thermal effects and thermal losses. The thermal losses describe transport of heat out of system by thermal conduction, radiation and convection.

A.1   Electromagnetic Radiation

Electromagnetic radiation is the predominant energy transport mechanism in optical thermography. It provides a means of detecting surface temperature as well as transporting energy towards the sample surface. Even though some energy from the heating source can be transported through convection, the distance between the light source and the target sample is assumed large enough for the effects to be negligible. Specifically when the sample is heated vertically, the heat in the surrounding air can be assumed to be dissipated through natural convection currents.

Figure A.1 illustrates that electromagnetic radiation is a oscillating wave varying in wavelength and frequency. In quantum theory, electromagnetic radiation can be seen to emit packets of energy known as photons, though treated as a a particle, possess energy that is proportional to its frequency (or wavelength). Basically a higher frequency is associated with a photon of higher energy. The combination of these two ideas is known as wave-particle duality as light has properties of both a wave and a particle. A photon can be seen as the microscale heat carrier that can be created or destroyed when radiation is emitted or absorbed respectively.

Despite the electromagnetic spectrum covering a vast number of wavelengths, in thermography a particular waveband is only of concern, known as the thermal radiation waveband. Thermal radiation describes a small portion of the ultraviolet, visual and infrared range of the electromagnetic spectrum
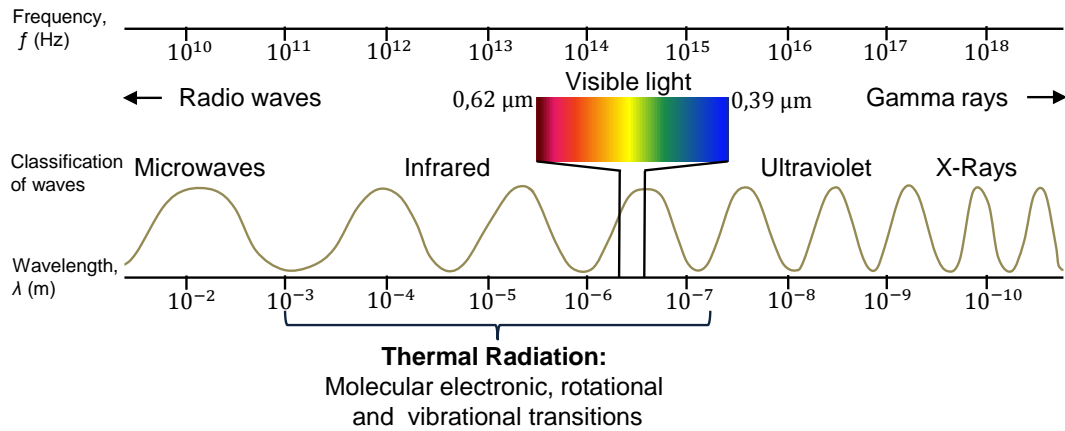
83

Figure A.1: Classification of electromagnetic radiation (adapted from Kaviany, 2002)

having a wavelength λ between 2×10^{-7} to 10^{-3} m (Kaviany, 2002), defined in Figure A.1. Strictly speaking, infrared and thermal radiation should not be used interchangeably.

All objects at temperatures above absolute zero (0 K) emit infrared radiation. Objects at room temperature predominantly emit infrared wavelengths. When these objects become hot they will begin to emit more radiation and at shorter wavelengths, such as visible and ultraviolet light. The spectral distribution of radiation energy is described by Planck's Law where the radiation from a black-body in thermal equilibrium is a function of surface temperature and wavelength (Planck, 1914). This distribution is explained using Figure A.2 and the total emitted radiation energy is a function of the area under the curve. The emitted radiation increases with increasing body temperature and the emitted radiation peaks at shorter wavelengths, i.e. more energy is available at shorter wavelengths. Hence why heated objects are observed to change from red to yellow to blue as the peak moves along the visible wavelengths.

Planck's law can be explained by microscale mechanisms of energy transport. For example, incandescent lights, such as hot filament bulbs, emit thermal radiation when electrical resistive heating causes thermally excited atoms to move to a higher energy state (orbital) which then falls back to its stable ground state. The excited states produce photonic emissions when relieved to this lower energy level. Photon theory describes three mechanisms by which molecules emit and absorb light: electronic transitions that happen for visible and ultraviolet wavelengths, vibrational transitions that happen for infra-red wavelengths and rotational transitions that happen for microwave wavelengths.

Electronic transitions describe a relatively higher energy state capable of exciting electrons of molecules that produce heating. Only higher energy per photon wavelengths, such as visible and ultrasonic wavelengths exhibit this mechanism. Infrared wavelengths contain less energy per photon and can only
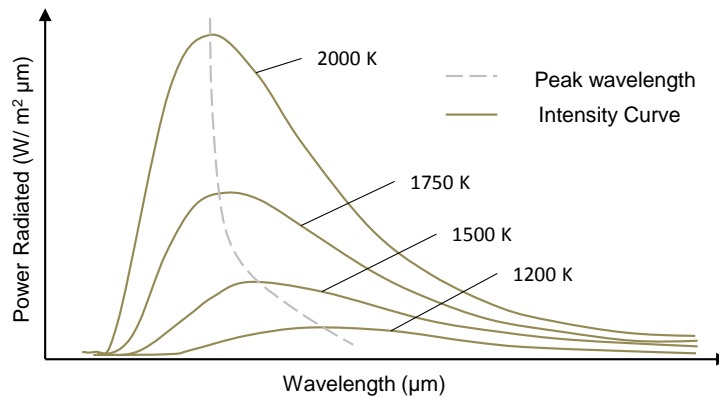
Figure A.2: Black-body radiation described by Planck's law for changes in temperature (adapted from Planck, 1914)

cause molecular vibrations between bonds of molecules, also known as bond stretching. Microwave wavelengths introduce rotational vibrations which are often not described in solids as the molecules are not free to move without interacting with the lattice. In particular, electromagnetic radiation emitted from a light source and irradiation that falls on a composite specimen tend to be linked to electronic and vibrational transitions. Interestingly, microwave wavelength transitions are able to introduce thermal energy into a solid body by the water content within that body. For this reason microwave heating could necessitate in the localized detection of water ingress in thick honeycomb composites.

Although a hot filament or warm target specimen emits wavelengths in the infrared band, not all the wavelengths respectively reach another surface or the infrared camera. This is because the transporting medium, air, has its own absorption wavelengths and does not behave like a transparent medium. As seen in Figure A.3, the air molecules are transparent to certain wavebands allowing most radiation to be transmitted in three infrared windows in the $1-3$ µm, $3-5$ µm and $8-15$ µm ranges. One can see that these transmittance windows are still not fully transparent and most of the thermal radiation emitted by a surface is attenuated.

An infrared camera is often defined by its operating wavelength range as either a short-wave infrared camera (SWIR), medium-wave infrared camera (MWIR) or long-wave infrared camera (LWIR). Table A.1 describes the applications of the infrared cameras operating at different infrared spectral bands.

Most photography cameras are partially sensitive to the near-infrared (NIR) band which is not typically used for thermographic inspection. Short-wavelength infrared (SWIR) cameras measure infrared radiation close to the visible light spectrum and is seen to deliver high resolution in contrast and detail. Mid-wavelength (MWIR) cameras produce more detailed resolution and accurate readings but are less detailed than long-wavelength (LWIR) as atmospheric

Table A.1: Camera spectral bands (Ibarra-Castanedo, 2005)

Spectral Bands	Range (µm)	Common Detector Materials	Applications
NIR	$0.74 - 1$	Si	Telecommunications
SWIR	$1 - 3$	InGaAs, PbS	Remote Sensing
MWIR	$3 - 5$	InSb, PbSe, PtSi, HgCdTe	High temperature inspections (indoors, scientific research)
LWIR	$8 - 14$	HgCdTe	Ambient temperature (outdoor, industrial inspection)
VLWIR	$14 - 1000$	–	Spectrometry, astronomy

absorption is increased in the MW band. The most common infrared camera is the LWIR cameras and along with mid-wavelength cameras provide accurate temperature measurements and spatial detail for a variety of temperature ranges (Ibarra-Castanedo, 2005).
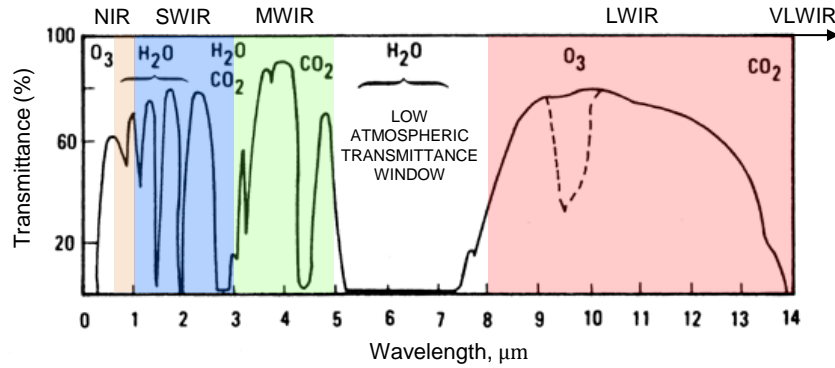
Figure A.3: Atmospheric windows and the absorption of radiation by particular molecules (adapted from Butler et al., 1988)

A.2   Photo-thermal Properties

Photo-thermal effects can be seen as optical properties that influence the amount of energy absorbed by the target specimen and the radiation observed by the infrared camera. The total incident thermal radiation that has reached the target surface is absorbed (A), reflected (ρ) and transmitted (τ) as shown in Figure A.4. The portion of the radiation absorbed is defined by the conservation of energy principle (Çengal & Ghajar, 2011):

$$A(\lambda, \theta, T) + \rho(\lambda, \theta, T) + \tau(\lambda, \theta, T) = 1, \qquad (A.2.1)$$

where radiation is a function of temperature T, direction θ and wavelength λ of the incident radiation. Therefore objects selectively absorb, reflect or transmit light of different frequencies. One commonly assumes τ is zero for opaque materials but this is only true in the visible waveband as the material may be transparent in other wavebands. Opaque materials generally perform better in optical thermography as they tend to absorb more energy from the visual wavelengths as most of emitted energy is contained in these wavelengths. With this in mind, an ideal heat source would need to emit wavelengths that match the absorption bands of the target specimen and thus reducing the effects of reflection and transmission.
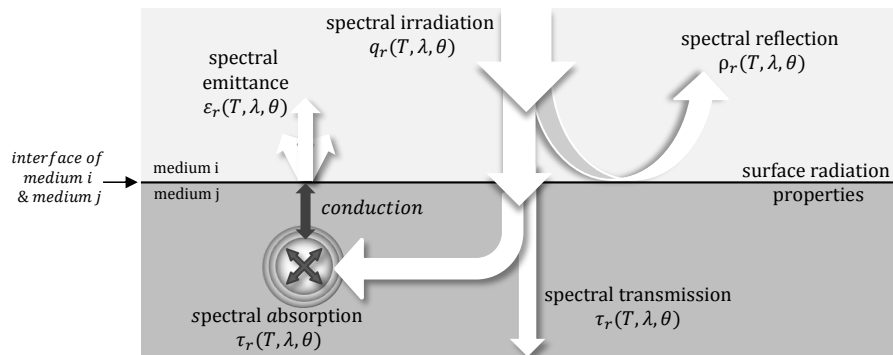
Figure A.4: Energy conversion of electromagnetic wave defined for two mediums with constant thermal properties (adapted from Çengal & Ghajar, 2011)

Thereafter the absorbed energy will eventually be transported to the surface by conduction. The surface will emit its own spectral distribution of radiation in all directions as a function of temperature.

A.2.1   Spectral Absorption

Thermal absorption is an simple idea of energy being absorbed from incident electromagnetic energy or photons. All materials have their own absorption spectrum and will heat up differently for the same incident radiation. The term *black-body* is used in heat transfer that describes a theoretical body that is a perfect emitter and absorber. It is considered to be opaque, non-reflective and absorbs all wavelengths of thermal radiation.

Optical absorption of energy does not happen instantly on the surface and occurs in a layer of negligible thickness as it is generally perceived. However the absorption depth of a material is defined by the penetration depth of the incident radiation. The penetration depth describes the attenuation of intensity of the radiation with increasing depth through the material and is

a function of wavelength. According to Beer-Lambert's law the exponential decay of wavelength intensity is defined as (Schuöcker, 1999)

$$I(z) = I_0 \exp\left(-\frac{z}{\delta_p(\lambda)}\right), \qquad\qquad (A.2.2)$$

where I_0 expresses the intensity at the interface of the absorbing material, z is the distance travelled beneath the surface and $\delta_p(\lambda)$ is the penetration depth as a function of wavelength λ. Larger wavelengths, which produce relatively large penetration depths, transmit deeper into the material or are less attenuated by initial thickness. Here penetration depth can be expressed as the transmittance of radiation defined by the sample thickness and wavelength, which affects the absorptivity of the material. For the material to be transparent the penetration depth must be large in comparison to its thickness. Infrared radiation has a larger wavelength than visible and ultraviolet radiation and is considered to have a larger penetration depth that allows the energy to travel further into the material before being totally absorbed. Interestingly, microwave wavelengths have the highest penetration depths or transmittance through materials (Maierhofer et al., 2010).

At very short times the thermal diffusion length μ_{eff} may be smaller than the penetration depth, see Figure A.5. At later times when $\mu_{eff} > \delta_p$ the effect of δ_p will have little influence on the time analysis. The time analysis will be typically taken at these later times when $t > 1$ s for transient thermography of relatively low diffusivity materials.
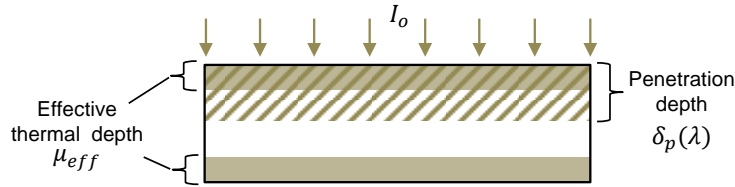

Figure A.5: Penetration depth and effective thermal diffusion length (adapted from Maierhofer et al., 2010)

A.2.2 Spectral Emissivity

Kirchoff's law of thermal radiation states that the emissivity and absorption properties of a surface must be equal to ensure maintenance of thermal equilibrium, i.e. a good absorber is also a good emitter (Rybicki & Lightman, 1979). Therefore spectral emissivity is a function of temperature, wavelength and inspection angle. Most objects are selective radiators and their emissivity varies strongly with wavelength. Stefan-Boltzmann's law states the power of

radiated energy from a black-body is proportional to the fourth power of its absolute temperature as (Çengal & Ghajar, 2011)

$$H = \sigma T^4, \tag{A.2.3}$$

where H is the heat radiated per unit area per unit time, $\sigma = 5.67 \times 10^8 \,\mathrm{W\,m^2\,K^4}$ is Stefan-Boltzmann constant and T is the body temperature in Kelvin. This law only holds true for a black-body. In order to apply this law to a real body another parameter was introduced to quantitatively specify the ratio of energy emitted by the real body ($H_{real-body}$) at a given temperature to an ideal black-body ($H_{black-body}$) at the same temperature. This is known as emissivity ϵ:

$$\varepsilon = \frac{H_{real-body}}{H_{black-body}}, \tag{A.2.4}$$

where $\varepsilon < 1$ is typical for a real body and $\varepsilon = 1$ describes an ideal black-body. Emissivity influences the amplitude of radiation that reaches the infrared camera and effectively describes the emitted radiation as a temperature measurement. If the material has a low emissivity the quality of the signal reaching the camera is weaker and the energy is equivalent to ambient reflections. One can apply a thin layer of black paint to a low emissivity target surface as this layer will experience the same effects as that of the body and the overall body will act like a black-body. However the application of black paint to the sample surface may not be possible when inspecting components in industry.

A.2.3   Spectral Reflectivity

Reflectivity describes the remaining radiation. A low thermal reflectivity indicates higher amounts of energy is absorbed or transmitted from the initial incident thermal source. High surface reflectivity of the surface introduces unwanted reflections that include ambient and radiating bodies surrounding the target sample.

Appendix B

Setup Design

The designs of the front-on and angled heating setups are provided here for their use in transient thermography. The light controller and the power specifications are also presented.

B.1   Experimental Setup

The front-on and angled heating setup are shown in Figure B.1 and B.2. The physical systems are exhibited in Figure B.3 and B.4.
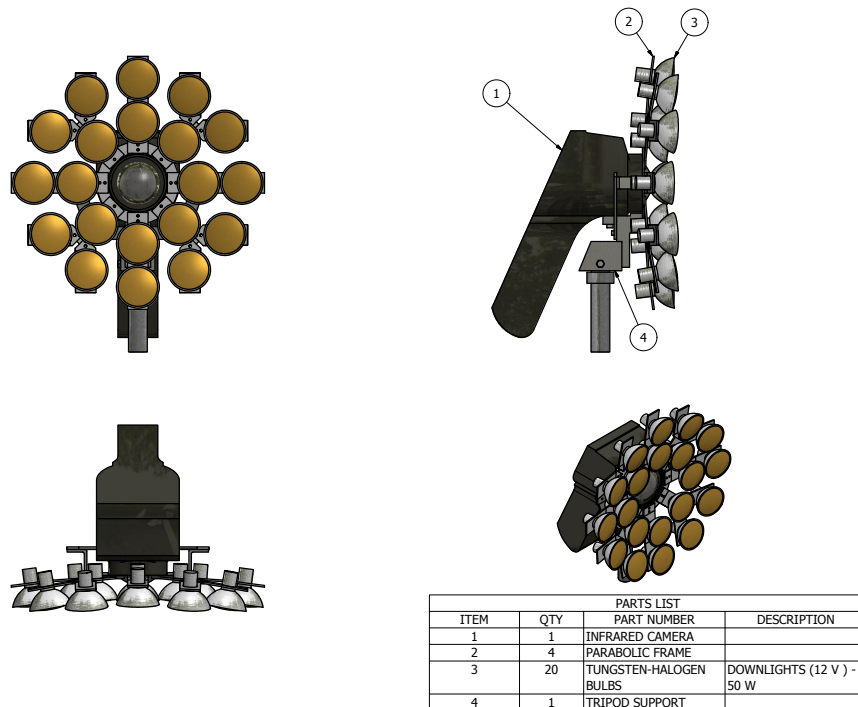
PARTS LIST			
ITEM	QTY	PART NUMBER	DESCRIPTION
1	1	INFRARED CAMERA	
2	4	PARABOLIC FRAME	
3	20	TUNGSTEN-HALOGEN BULBS	DOWNLIGHTS (12 V) - 50 W
4	1	TRIPOD SUPPORT	

Figure B.1: Front-on heating setup: maximum power of 1000 W (20×50 W)

PARTS LIST			
ITEM	QTY	PART NUMBER	DESCRIPTION
1	1	TEMPERED GLASS	5 mm THICK
2	1	REFLECTOR	DUAL-PARABOLA
3	2	TUNGSTEN-HALOGEN BULB	DOUBLE ENDED (254 mm) - 1000 W
4	2	INSULATED BULB PORT	SPRING LOADED CONNECTOR PINS
5	2	SILCONE HEATPAD	2 mm SILICONE RUBBER
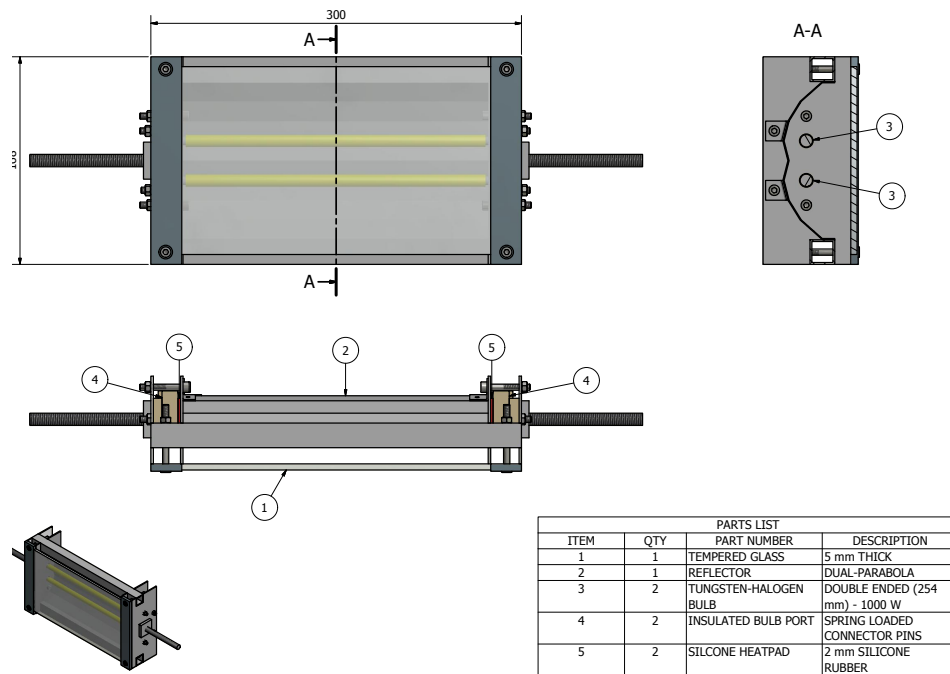
Figure B.2: Angled heating setup: maximum power of 4000 W (4×1000 W)

Figure B.3: Front-on heating setup in operation

B.2   Light control

The two light setups are controlled through a relay module and a Raspberry Pi B single-board computer. The Raspberry Pi has general input and output pins ('GPIO') that can interface the relay module through connections as seen

Figure B.4: Angled heating setup in operation

in Figure B.5. The relay module is used to isolate the high power of the light system and the low power Raspberry Pi. The Raspberry Pi is controlled through a laptop via an ethernet port using VNC-tight virtual desktop. Both the camera and lights can be operated through a python script to ensure testing times are constant. The simultaneous capture initiated the start of thermal sequence and further reduces storage of unnecessary cold images.
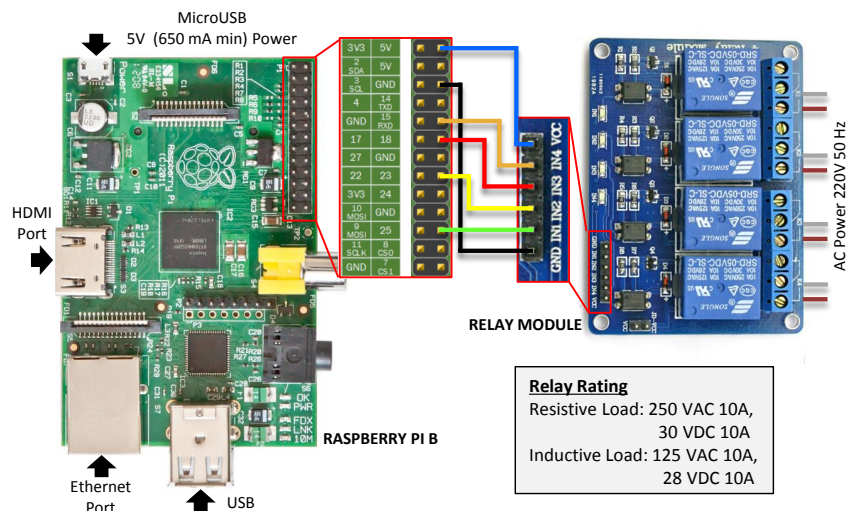
Figure B.5: Interface between Raspberry Pi and relay board

Since a high current DC power supply ($I > 3$ A) was not available, the use of alternating voltage from the electricity grid was utilized. A maximum drawing current of 4.54 A was calculated ($I = P/V$), knowing the combined power rating of the lights in series (1000 W) and the line voltage (220 VAC). Caution was taken wiring and connecting the setup to ensure both the relay and connections are rated over 5 A. The chosen relay is rated for 250 VAC 10 A for the resistive load. Another precaution was to ground the setup to reduce any chances of damage to the infrared camera or light system and further reducing the risk of an electrical injury.

A blackbox was designed to encase both the Raspberry Pi and relay module and isolate the high voltage connections, shown in Figure B.6. The black box is powered by a 5 V 700 mA microUSB phone charger. To power the four relays simultaneously the 5 V power supply should be rated higher than 500 mA.

Figure B.6: Black box light controller

The python code executed by the Raspberry Pi to initiate the lamp relay switches is given here:

Listing B.1: Relay Switch Control Script

```
\# Light On/Off Script for 4 Relays
import RPi.GPIO as GPIO
import time
GPIO.cleanup()
GPIO.setmode(GPIO.BOARD)

# Define Sleep Constant
        x = 60; # x seconds
# Setup Relay #1-4
        GPIO.setup(15,GPIO.OUT)
        GPIO.setup(18,GPIO.OUT)
        GPIO.setup(23,GPIO.OUT)
        GPIO.setup(25,GPIO.OUT)

# Switch "ON" Relay #1-4
        GPIO.setup(15,true)
        GPIO.setup(18,true)
        GPIO.setup(23,true)
        GPIO.setup(25,true)

        time.sleep(x) # Sleep For x seconds

# Switch "OFF" Relay #1-4
        GPIO.setup(15,false)
        GPIO.setup(18,false)
        GPIO.setup(23,false)
        GPIO.setup(25,false)
```

Appendix C

Extraction of the Thermal Sequence

The raw thermal sequence is obtained by desconstructing the recorded *FLIR®* *Tools+* file. The file can be identified by the .seq file extension which is a proprietary archive file containing: a sequence of 16-bit uncompressed frames of analog-to-digital (A/D) sensor counts; image metadata, such as image dimensions, frame rate, type of camera, time stamp of image, etc.; user-defined thermal parameters, such as emissivity; and user-defined atmospheric parameters that include reflective temperature and ambient temperature

The contents of the archive are conveniently represented by hexadecimal digits. Simply by knowing the dimensions of the image, i.e. number of bytes per image which is constant for the entire sequence, one can extract the images by finding a repetition or pattern in the hexadecimal code (Eevblog, 2014). In programming this pattern is controlled by hard-coded hexadecimal number which are in-code flags (constants or letters) that provide an effective way for the software to easily distinguish and find the different frames. There was no software development kit (SDK) package so each image was identified by a hexadecimal pattern. With the aid of a Perl script, as provided in Figure C.1, the image and metadata of each frame can be separated into individual images in a FLIR file format (.FFF). To use a Perl script, one can download *ActivePerl* which is available for all operating system platforms. Since Windows is the chosen operating system, command prompt was used to execute the script 'split.pl' on the sequnce file 'thermaldata.seq' as seen in Figure C.2. The current directory of the script will now contain the entire thermal sequence as a separate sequence of .FFF files. An individual .FFF file contains the radiometric image containing temperature counts and metadata information for a particular frame. The metadata contains camera constants that is needed for calculation of absolute temperature values.

An open-source metadata editor known as *ExifTool*[1] can be used to sepa-

---

[1] http://www.sno.phy.queensu.ca/~phil/exiftool/

rate the metadata from the radiometric image. This image is saved as a 16-bit uncompressed *TIFF* image containing A/D counts.

```perl
1 #!/usr/bin/perl
2 undef $/;
3 $_ = <>;
4 $n = 1;
5
6 # Flir Tools Output
7 $pat = "\x46\x46\x46\x00\x43\x41\x50";
8
9 for $content (split(/(?=$pat)/)) {
10     open(OUT, ">seq" . ++$n . ".fff");
11     binmode OUT;
12     print OUT $content;
13     close(OUT);
14 }
```

Figure C.1: Perl script to split up FLIR® sequence metadata (.seq) into individual FLIR File Format (.FFF) images

```
C:\Users\Jay> perl -f split.pl thermaldata.seq
```

Figure C.2: Executing the Perl script: 'split.pl'

To summarise, the recorded .seq file is first deconstructed to multiple .FFF files that is automatically extract to TIFF images through a batch file. The sequence of extracted images is subsequently imported into Matlab and combined as a three dimensional data matrix creating the thermal image sequence containing analog-to-digital counts.

C.1 Treatment of Thermal Data

The thermal signal used in the processing methods is obtained from the analog-to-digital (A/D) counts rather than actual temperature measurements. The main difference between them is illustrated in Figure C.3. The infrared camera's sensor produces a change in voltage for a change in absorbed radiation which is converted into digital information, known A/D counts. Figure C.3 describes the total radiation E_{tot} is the sum of the radiation of the target body E_{body}, the surrounding radiation reflected by the object E_{refl} and the atmospheric contribution to the measured radiation, E_{atm}. The radiative terms, E_{refl} and E_{atm}, are removed from the total incident radiation through user defined constants such as ambient temperature, ambient reflection temperature and the temperature of the optics. Knowing or estimating these values is not straightforward. Furthermore the radiation entering the camera needs to account for the attenuation of radiation in the atmosphere and a value of the
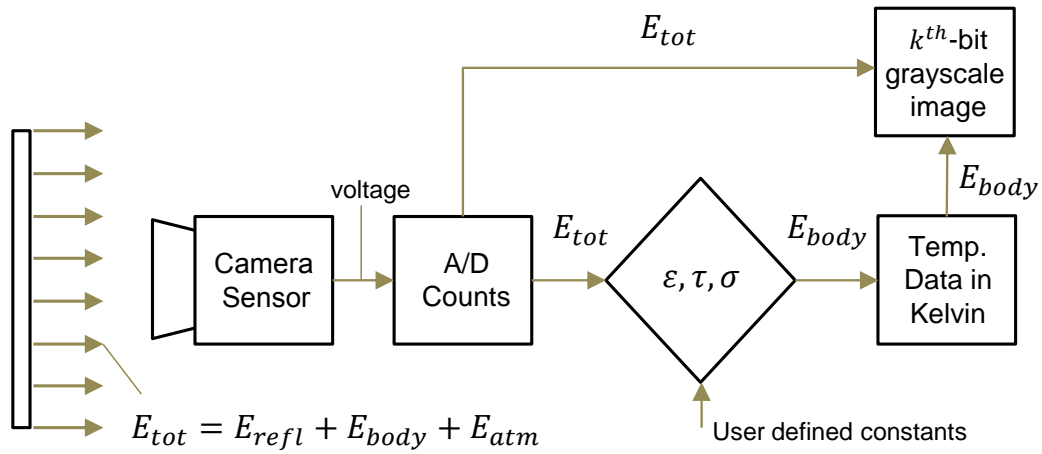
Figure C.3: Defining the raw signal of an infrared camera

transmittance τ of radiation is assumed. Before the body temperature measurements can be calculated the bulk emissivity value is defined by the user between 0 and 1. Even though the constants can be determine through proper calibration (linear transformation function) of the temperatures with a blackbody apparatus, the need for absolute temperature is considered redundant. For defect inspection with thermography, only a relative contrast between defective and non defective regions in the thermogram is required. This permits the use of A/D counts which are linearly proportional to incident radiation (FLIR Systems, 2008). Furthermore, the temperature information is calculated through a set of linear equations which again warrants the use of the A/D counts.

Appendix D

Thermographic Graphical User Interface

A graphical user interface (GUI) was developed to aid in the application of processing methods to thermographic sequences. The GUI can be found here: http://tinyurl.com/ptu25n7. The GUI provides the variety of algorithms mentioned in Chapter 4 applicable for both transient and pulsed thermal sequences. The GUI was developed in Matlab® R2013b and requires little support from additional toolboxes or implementations of newer Matlab® versions. The main GUI interface is shown in Figure D.1. The various panels designated by the numbers in the figure will be discussed below.

D.1   Import and Export Sequence

The import panel provides import and export of raw or processed thermal sequences. The GUI supports the import of the following two data types: Matlab® binary (.mat) file and tagged image file format (.tiff). If the sequence consists of multiple files with in the selected directory, the files will be imported and reformatted into a single three-dimensional matrix in the order of date created.

A screenshot and a three-dimensional surface plot of the current process image can be produced by the appropriate buttons underneath the processed image.

D.2   Debug Panel

The debug panel provides assistance when using the GUI and displays when an algorithm is completed. Each algorithm will initiate its own wait-bar that will provide an estimated time of completion. The panel also displays the recording and image properties of the sequence.
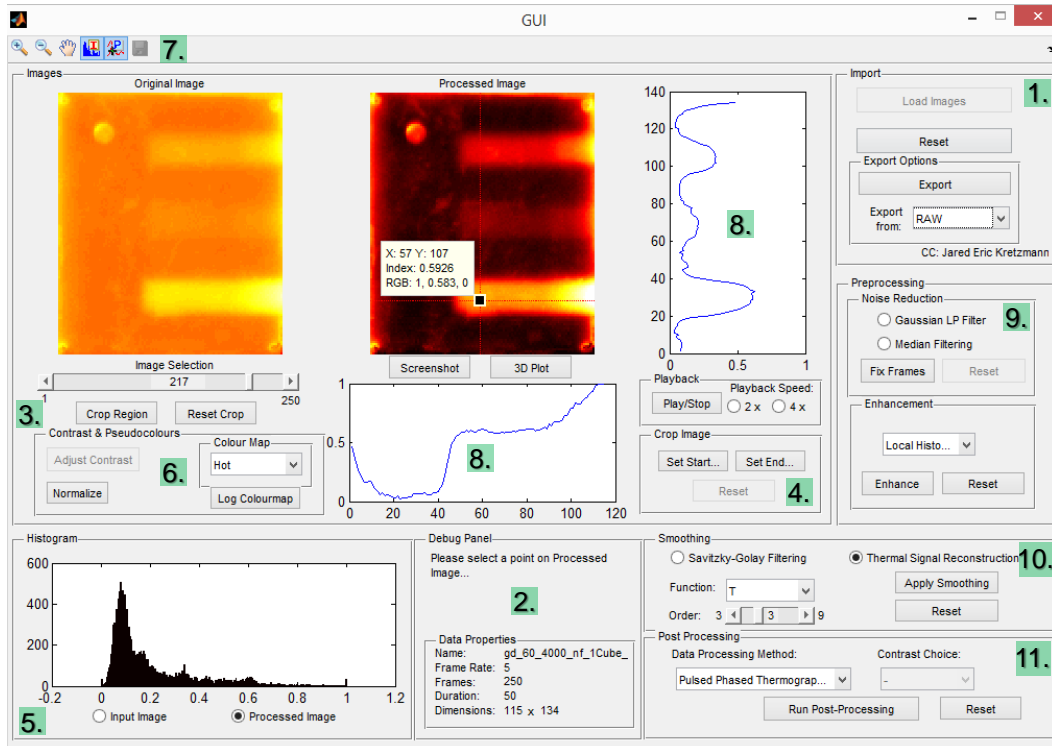
Figure D.1: Graphical user interface (GUI) for thermography

D.3   Crop Image Region

The crop region button triggers a rectangular window that appears on the processed image allowing a user to crop the image dimensions for the entire sequence. This is beneficial for focusing in on a particular region of interest, which can subsequently increase the visual contrast of the cropped region. The reset crop button will reset the image dimensions to its previous state.

D.4   Crop Thermal Sequence

The crop image panel offers the ability to redefine the truncation window of the thermal sequence, or the number of frames. The image selection slider is used in conjunction with the appropriate push button to crop from the current image. The reset button will reset the image to its previous frame length.

D.5   Histogram Plot

The histogram panel provides both the original and processed image histogram options. The histogram allows inspection of the dynamic range where 0 and 1

respectively represent black and white intensities. Alternatively the histogram represents the distribution of the temperature range in the selected image.

D.6   Adjust Visualization

The contrast and pseudocolours panel enhances the visualization of the thermal sequence. Multiple colourmaps can be chosen along with logarithmic colourmap options. The adjust contrast tab allows manual clipping of high or low frequency bins to enhance the thermogram. The normalize button ensures that the dynamic range of an image has been fully utilized by the thermal data.

D.7   Image Tools

The toolbar panel provides common image tools, such as zoom and pan. Additional features include selection of an image pixel for displaying the temperature history (P) or the vertical and horizontal spatial profiles (I).

D.8   Display Axes

The two display axes plot either the temperature sequence (P) or the vertical and horizontal spatial profiles (I) of the selected pixel. The vertical and horizontal lines on the image designate the spatial profiles of the pixels of interest and are plotted on the corresponding display axes, seen in Figure D.1.

D.9   Pre-processing

The pre-processing panel provides noise filters and spatial image enhancement algorithms, such as histogram equalization. The selected method is iterated over the entire sequence.

D.10   Signal Smoothing

The signal smoothing panel is an important tool for thermographic signals contaminated with noise. This can be used as another pre-processing method to reduce temporal noise. Both the smoothing methods provide first and second derivatives that can be selected by the drop-down box. The order slider provides the fitting polynomial order.

D.11   Post-processing

The post-processing panel provides a drop-down menu of the processing methods discussed in Chapter 4. Particularly when the thermal contrast processing method is selected the contrast choice drop-down box is enabled and provides a further selection of contrast options, such as absolute contrast and interpolated differential absolute contrast.

Appendix E

Samples

The samples used for this project include: polymethyl methacrylate (PMMA also known as Plexiglas®), carbon and glass fibre reinforced polymers (CFRP & GFRP) with fiber densities of either 106 or 200 $\mathrm{g\,m^{-2}}$. The flaws include: polytetrafluoroethylene (PTFE also known as Teflon®) inclusions, air-gap inclusions and flat-bottom holes.

The approximated thermal properties of the materials are provided in Table E.1, which are obtained from literature.

Table E.1: Thermal properties of the sample materials

		Ampreg 21 Epoxy[1]	PMMA[2]	PTFE[3]	CFRP[4]	GFRP[4]	Air[5]
Density, ρ	$\mathrm{kg\,m^{-3}}$	1180	1200	970	1600	1900	1.2
Conductivity, k	$\mathrm{W\,m^{-1}\,K^{-1}}$	0.18	0.20	0.25	0.80	0.30	0.02
Specific heat, c_p	$\mathrm{J\,kg^{-1}\,K^{-1}}$	1450	1470	916	1200	1200	1005
Diffusivity, α	$\mathrm{m^2\,s^{-1}} \times 10^{-7}$	1.05	1.13	1.24	4.2	1.3	2210
Effusivity, e	$\mathrm{J\,m^{-2}\,K^{-1}\,s^{-1}}$	555	594	710	1239	827	5.6

[1] AMT Composites (2015);   [2] Grys & Minkina (2010);   [3] Blumm et al. (2010);
[4] Ibarra-Castanedo (2005);   [5] Çengel & Ghajar (2011)

(a) Opaque: Square   (b) Opaque: Circle
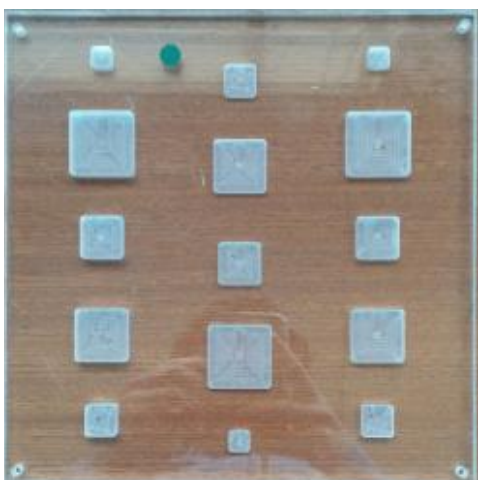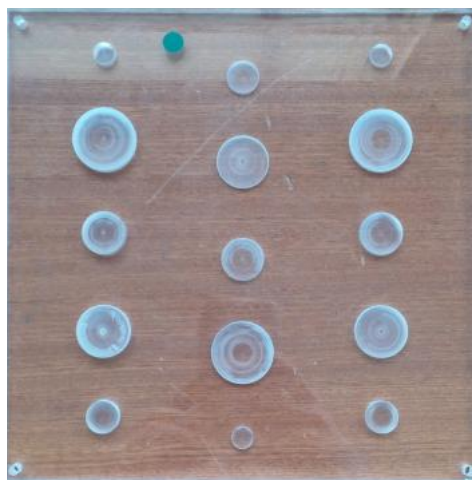
(c) Clear: Square   (d) Clear: Circle

Figure E.1: Surface of PMMA samples with flat-bottom holes

(a) CRFP200A   (b) CRFP200B   (c) GRFP200

(d) GRFP106A   (e) GRFP106B   (f) CRFP200DEL

(g) CRFP200DEL
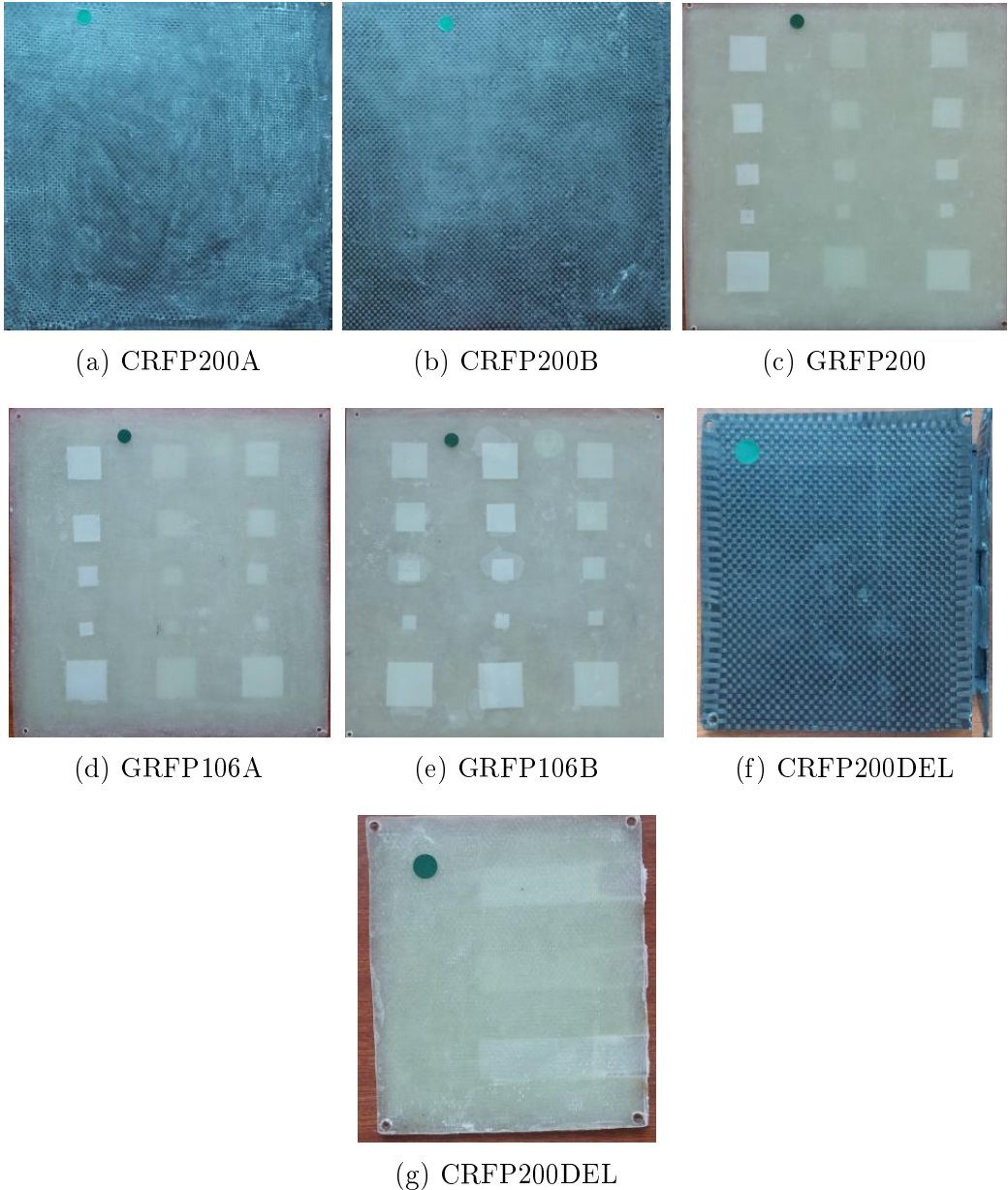
Figure E.2: Front surface composite PTFE (a - e) and air (f - g) delaminations

Appendix F

Optical Heating in Transient Thermography

F.1   Effects of Optical Heating

The heating power, duration and type of heating regime (step or square-pulse) have an influence on the defect contrast and thus on the number of observable defects. Heating power describes both the rated power of the lights and the spectral energy of the emission. These effects are evaluated with the angled heating setup to provide a preferred scenario for transient inspection.

F.1.1   Heating Power

Two different heating powers were compared to highlight the effects of heat input. Figure F.1 displays the differences between using a 2000 and a 4000 W rated power halogen light system. For a double increase in the rated power a double increase in contrast is observed. Lower heating powers was seen to produce similar contrast levels at a much later inspection time. Therefore a higher heating power was preferred to keep inspection times short.

F.1.2   Thermal Duration

The detection and contrast strength of deeper defects is related to the total heating duration and total heating power. It was already seen that an increase in heating power had a corresponding effect on defect contrast. The effect of thermal duration is investigated for the maximum available rated power of 4000 W.

The time of emerging defect contrast is related to the speed of thermal diffusivity. For that reason the effect of thermal duration is investigated for the material with the slowest thermal diffusion rate, namely the PMMA sample (see Appendix E). The defect contrast for thermal duration times of 10, 25 and

104
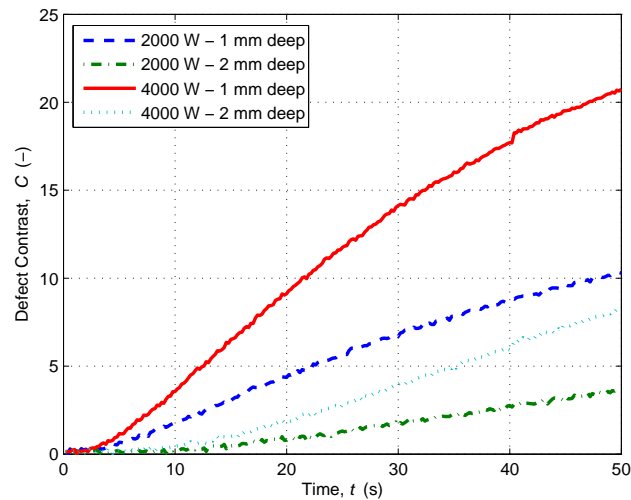
Figure F.1: Effect of heating power on the thermal contrast of a 20 mm defect

50 s are plotted for the smallest flat bottom hole (10 mm) in the clear PMMA sample.

A maximum time of 50 s was selected to prevent over-heating the sample surface above 70 °C, which is close to the glass transition temperature of the Ampreg epoxy resin (AMT Composites, 2015). This can be seen as a limiting factor in the selection of an appropriate heating power and duration. This is a problem for low diffusivity materials that experience a larger rise in surface temperature as the material is incapable of transferring the absorbed heat fast enough away from the heated surface. Similarly, the 50 s duration provides a short inspection scenario that is fairly competitive to pulsed thermography and surpasses the long heating times of lock-in. Interestingly, long heating times ($t > 30$ s) for the CFRP 200A sample revealed a reduction in defect contrast as illustrated by Figure F.2.
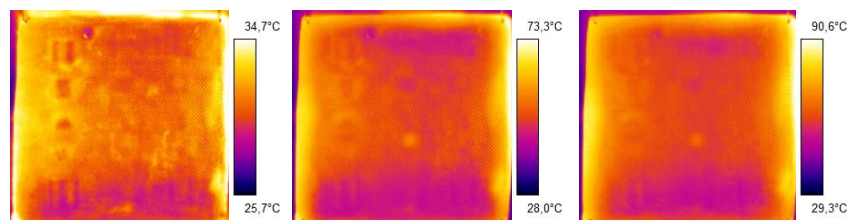
Figure F.2: The reduction in defect contrast for heating times longer than 30 s for CFRP 200A

For square pulse heating, a heating time of 16 s was selected through trial and error to deliver enough heat to the sample but also short enough to allow

the thermal decay to be observed within the 50 s duration. Usamentiaga et al. (2012) describe that the cooling phase of square pulse thermography shows more significant information than the heating phase.

The depth probing limitations of transient thermography are evaluated for the thick clear PMMA sample. The clear PMMA sample describes the least optimal material heating case, which is transparent to most of the optical energy and has a low surface emissivity. Figure F.3 shows that a double increase in heating duration, from 25 to 50 s, for the 2 and 5 mm deep defect produces a double increase in defect contrast. For a defect depth of 7 mm the contrast is comparable to the thermal sensitivity of the thermal camera (NETD = 0.05). Regardless of the poor contrast for a 7 mm deep defect, Figure F.3(b) reveals that a contrast is vaguely observable. The maximum depth of the artificial defects in the composites are between 1 and 5 mm deep, a heating duration of 50 seconds is considered to be adequate in identifying these defects at these depths.

(a) Maximum contrast

(b) Defect choice
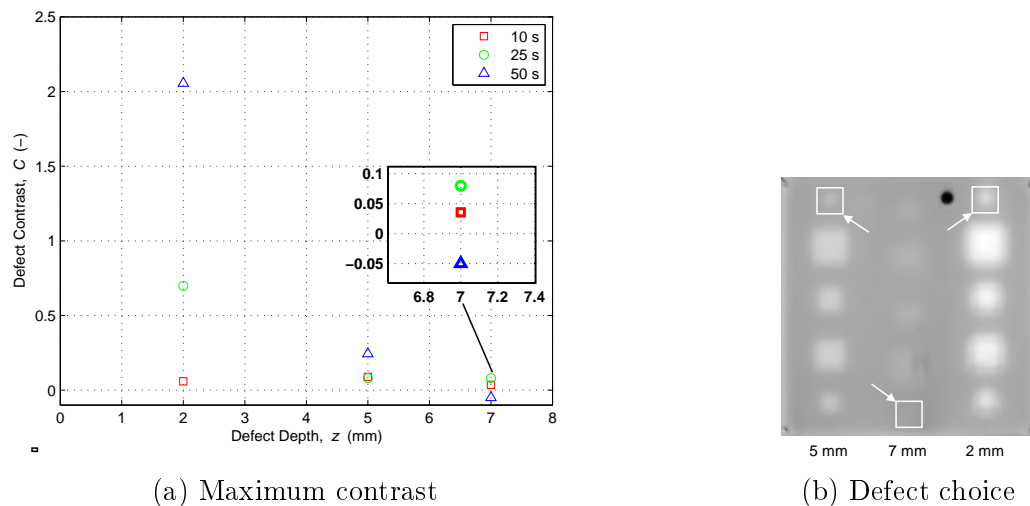
Figure F.3: Defect contrast for different heating durations in the clear PMMA

F.1.3   Spectral Power

The amount of energy absorbed by a sample is also related to both the spectral emissions produced by the halogen lamp and the absorption spectrum of the target sample. Since the material absorption properties cannot be controlled, the effect of the infrared energy is investigated. Infrared wavelengths are an anticipated problem in thermography especially when the wavelength matches the spectral range of the thermal camera, which introduces adverse reflections. One can easily filter out infrared radiation through a glass-silica pane and this

has already been observed in reducing the effects of infrared reflections. Yet
infrared energy may be beneficial when inspecting materials that are not fully
opaque, such as epoxy resins in composites.

The opaque and clear PMMA samples describe two contrasting materials
that differ in thermal absorption characteristics but share the same thermal
diffusivity. The clear PMMA acts as a low pass filter allowing most visible light
(and UV) to transmit but absorbs infrared wavelengths. The black opaque
PMMA sample acts as a high pass filter allowing visual light to be absorbed,
while transmitting most of the infrared wavelengths. These absorption effects
are consistent in sample thicknesses between 3 and 24 mm (Sebastian, 2011).

Consequently two heating factors are simultaneously investigated: the ef-
fects of infrared wavelengths and the effects of the transient heating regime.
The excess temperature responses are plotted side-by-side in Figure F.4 for a
total heating duration of 50 s. The plots describe the temperature response
of a center pixel of a 20 mm defect at a depth of 2 mm in both the clear and
opaque PMMA samples. Each plot displays the effect of infrared on the total
temperature rise.

(a) Step heating   (b) Square pulse heating
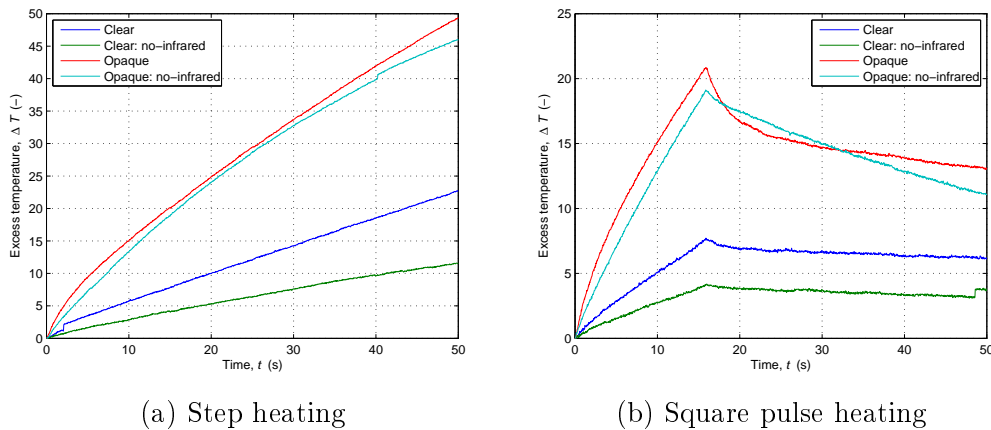
Figure F.4: Excess temperature response for transient heating

The samples that were exposed to infrared wavelengths produced a higher
excess temperature in both step and square pulse heating responses. The
temperature was typically higher as more energy becomes available from the
introduction of additional infrared wavelengths - assuming the absorption spec-
trum can absorb these wavelengths. The clear PMMA sample displays a more
noticeable shift between heating the sample with and without the infrared
wavelengths. The smaller change between the thermal response of opaque
PMMA sample could be linked to the sample being transparent to most in-
frared wavelengths.

The defect contrast is of more importance in the inspection of inclusions, however Figure F.4 will highlight if the increase in excess surface temperature produces an equal increase in contrast. Figure F.5 and F.6 reveal the relative thermal contrast over time for 15 mm defect at various known depths. The defect contrasts of both the step and square pulse heating responses are plotted together with and without infrared.
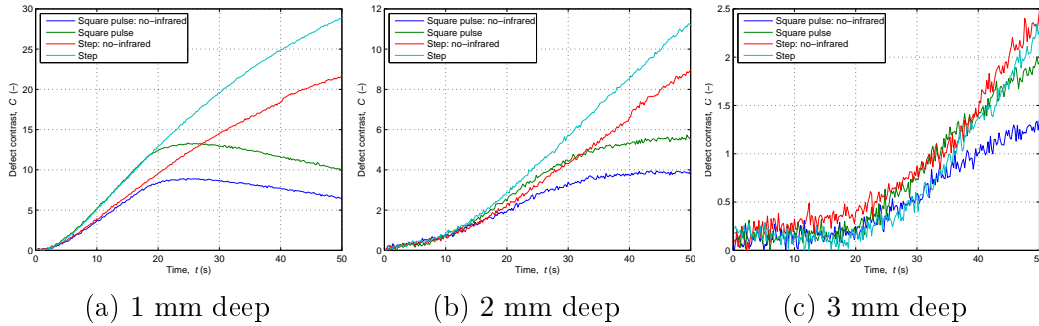

| (a) 1 mm deep | (b) 2 mm deep | (c) 3 mm deep |

Figure F.5: Thermal contrast of flat-bottom holes in the opaque PMMA sample

| (a) 2 mm deep | (b) 5 mm deep | (c) 7 mm deep |
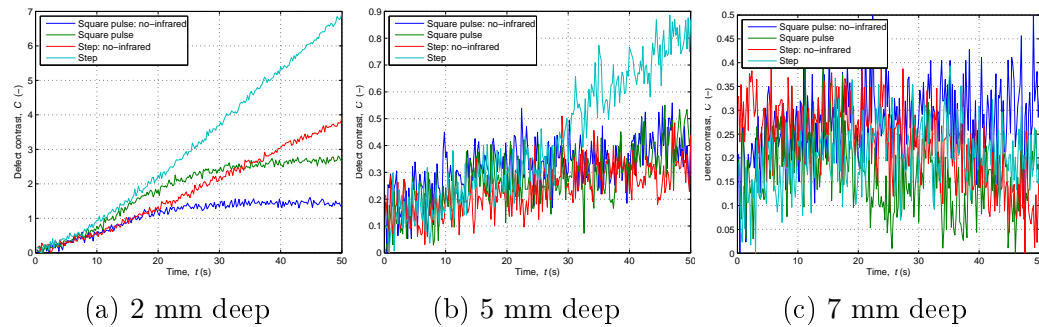
Figure F.6: Thermal contrast of flat-bottom holes in the clear PMMA sample

Step heating with infrared wavelengths produces the highest overall contrast. The effects of energy input and thermal heating regime appear to have a negligible effect on the contrast for defects deeper than 3 mm. The thermal contrast of the 5 and 7 mm deep defect are weak and contaminated with a high noise component and no exact conclusion can be formed. For this reason the overall defect detectability is rather visualised as image using statistical moments, such as kurtosis or skewness. Kurtosis was chosen to collate all the information into one single image to highlight any differences in the results.

The kurtosis images are displayed in Figure F.7 showing the effects of infrared wavelengths for a corresponding thermal regime. No increase in the

algorithm's performance is seen in the opaque sample while the clear sample shows increased contrast with the additional infrared wavelength energy. One can observed higher reflections in the clear PMMA sample, which has a lower surface emissivity. Interestingly, the square pulse heating displayed a better detection of the 5 mm deep defect in the clear PMMA, however the defect contrast was more rounded for the shallow defects.
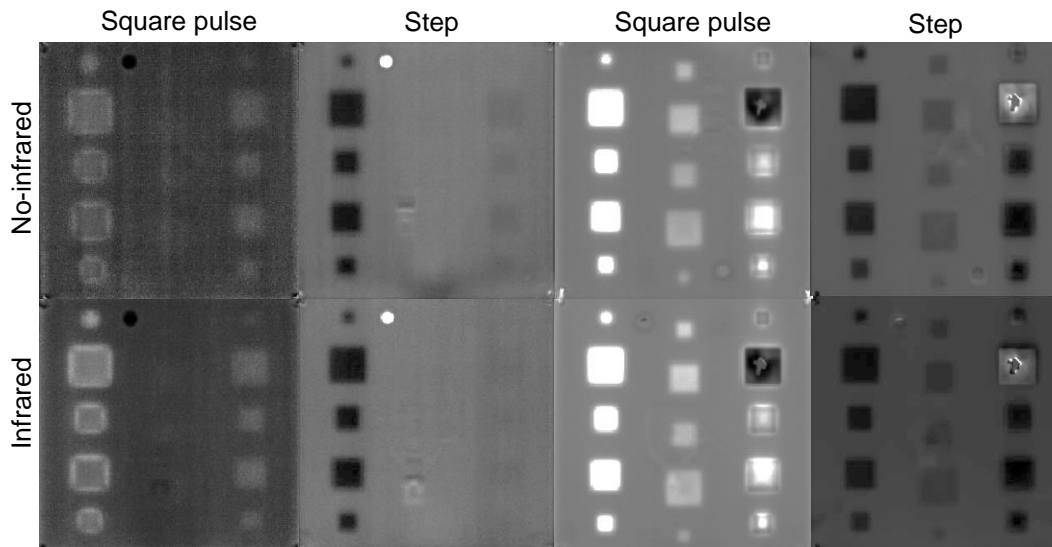

Figure F.7: Kurtosis image showing the effects of infrared wavelengths on defect contrast for the clear (left) and opaque (right) PMMA samples

F.2   Sampling Frequency

The sampling frequency of the infrared camera is important when estimating defect depth using inversion methods. The appropriate sampling frequency depends on thermal diffusivity of the material and shallowest detectable defect. Even though composites are considered low diffusivity materials, an optimal frame rate has not been disclosed in literature.

The effect of the sampling frequency is evaluated on a shallow defect in a carbon fibre sample. The carbon fibre sample is expected to experience a faster thermal response as it exhibits the highest thermal diffusivity out of all the samples. Figure F.8 illustrates the recorded thermal response of the shallow defect in the carbon sample for sampling frequencies between 1 and 30 Hz, which is the maximum available sampling frequency. The optimal frame rate for transient thermography can be expected to be lower than that for pulsed thermography, which is performed at sampling frequencies of $f_s > 30$ Hz. This can be predicted by the breakpoint of the one-dimensional step response that

occurs at a later Fourier number (Fo = 1.27) than for the pulsed thermography (Fo = 0.318) in the Fourier domain (Balageas & Roche, 2014). To clarify, the dimensionless Fourier number defines the thermal response as a function of thickness, time and material properties, $Fo = \alpha t/L$.

The thermal response in Figure F.8(a) has been fitted using a 5th order polynomial with thermal signal reconstruction method to make the differences clear. A sampling frequency between 15 and 30 Hz is observed to produce similar results. A sampling frequency of 5 Hz shows a slight deviation from the higher sampling frequencies but this difference is comparable to the noise of the response. However a sampling frequency of 1 Hz shows a poor choice for measuring the initial thermal response of the defect. For the slower sampling frequencies, there is a favourable reduction in signal noise as illustrated in Figure F.8(b). For that reason a frame rate of 15 Hz is selected to minimize the noise in thermal data without compromising precision of the thermal response.

(a) Surface Temperature Response   (b) Noise Presence
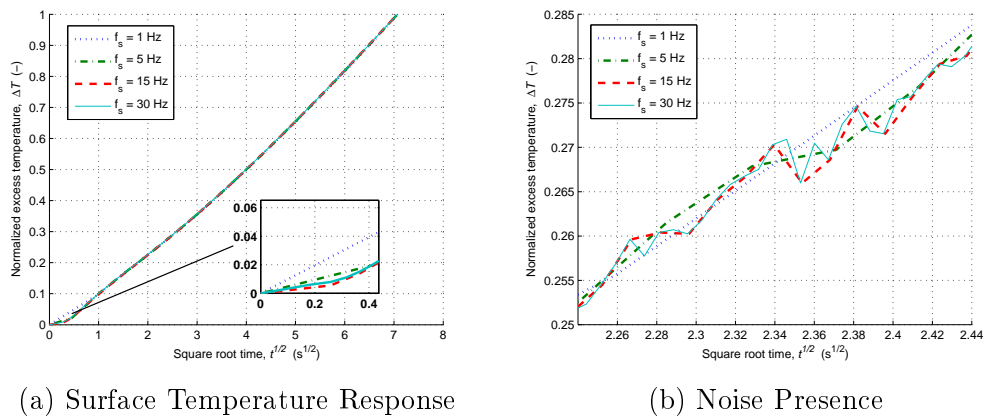
Figure F.8: Effect of sampling frequency on a shallow 20 mm defect (1.38 mm deep) in CFRP200A

F.3   Conclusion

An increase in heating power, spectral power and duration for both transient regimes produced a proportional increase in defect contrast. There exists a limit where an increase in energy no longer produces an increase in contrast, which is defined by the material's thermal diffusivity. This describes the depth limitations of transient thermography. Step heating displayed a sharper defect definition that better resembled the actual defect shape. Square pulse heating was able to detect the same number of defects with better or similar image contrast for a lower total energy input. The square pulse heating also exhibited better defect detectability for low emissivity materials.

Appendix G

Results

G.1   Raw Thermograms
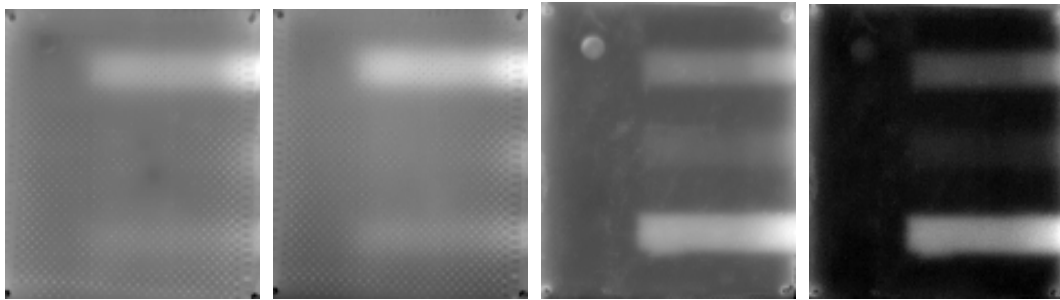
(a) CFRP200DEL: S   (b) CFRP200DEL: SQ   (c) GFRP200DEL: S   (d) GFRP200DEL: SQ

Figure G.1: Unprocessed (raw) thermograms of the artificial air-gap delaminations for step (S) and square-pulse (SQ) heating
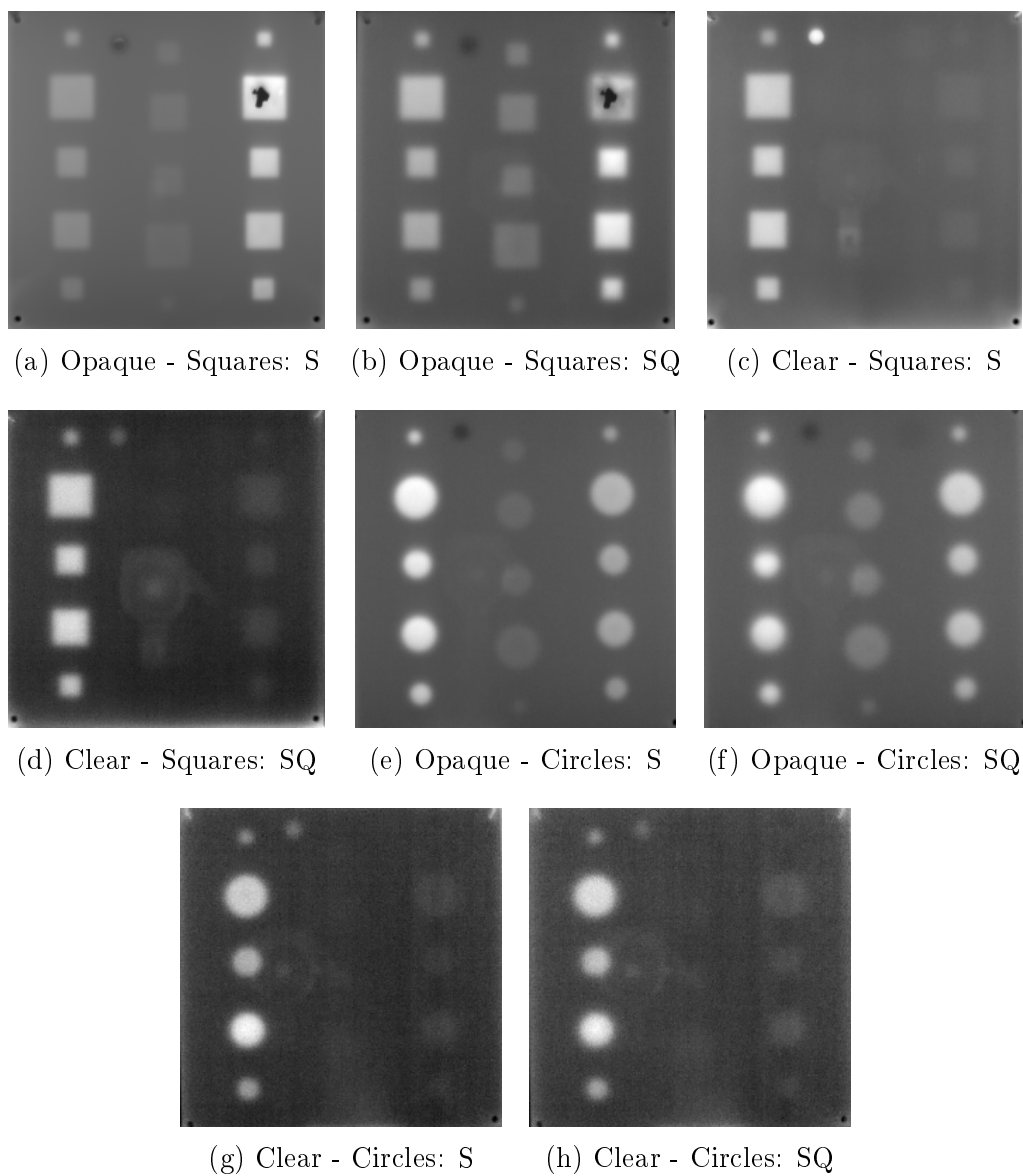
(a) Opaque - Squares: S   (b) Opaque - Squares: SQ   (c) Clear - Squares: S

(d) Clear - Squares: SQ   (e) Opaque - Circles: S   (f) Opaque - Circles: SQ

(g) Clear - Circles: S   (h) Clear - Circles: SQ

Figure G.2: Unprocessed (raw) thermograms of the flat-bottom holes in PMMA for step (S) and square-pulse (SQ) heating

(a) CFRP200A: S

(b) CFRP200A: SQ

(c) CFRP200B: S

(d) CFRP200B: SQ

(e) GFRP200: S

(f) GFRP200: SQ

(g) GFRP106A: S

(h) GFRP106A: SQ

(i) GFRP106B: S

(j) GFRP106B: SQ
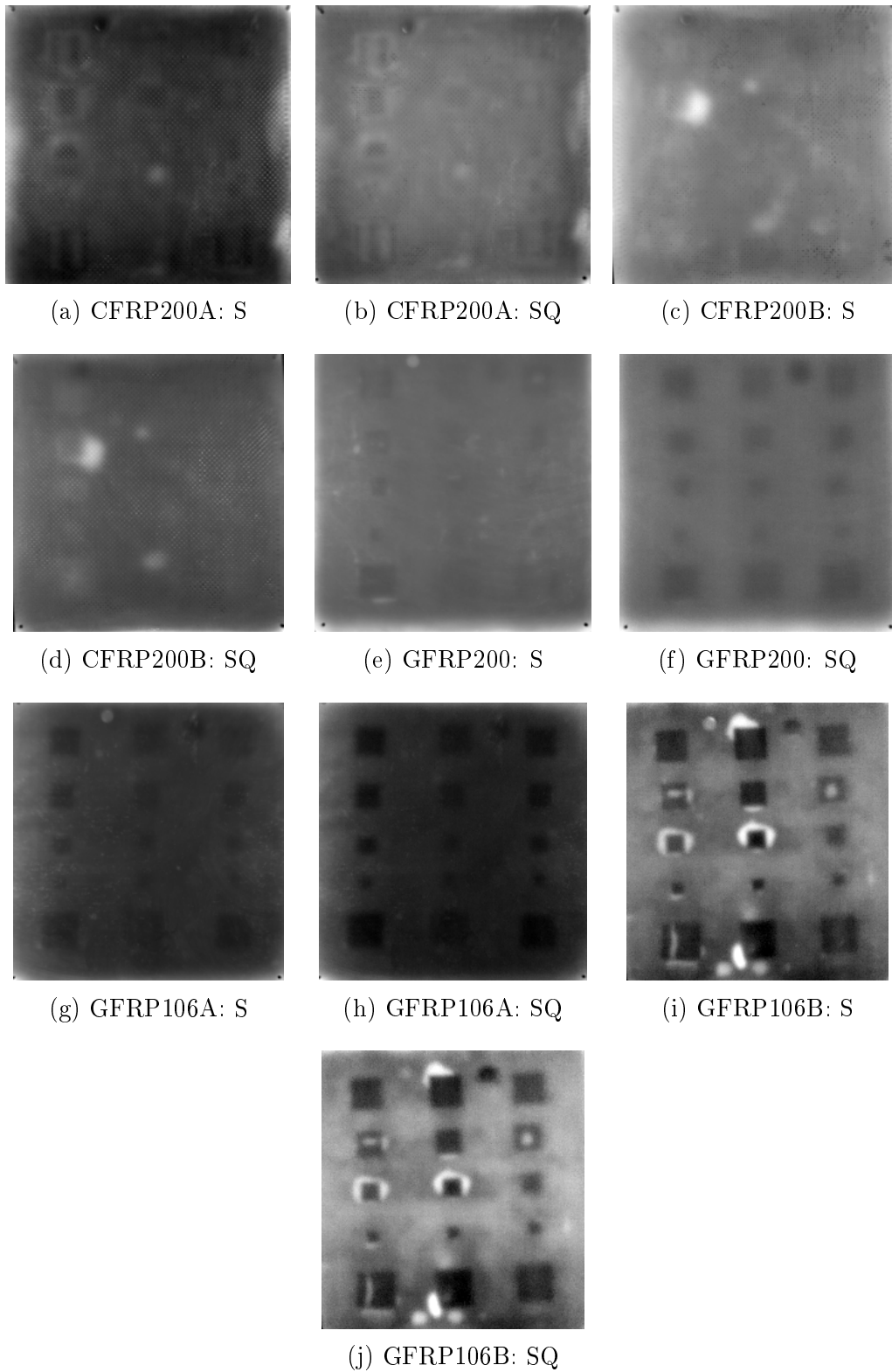
Figure G.3: Unprocessed (raw) thermograms of the artificial PTFE inclusions for step (S) and square-pulse (SQ) heating

G.2   Artificial Samples
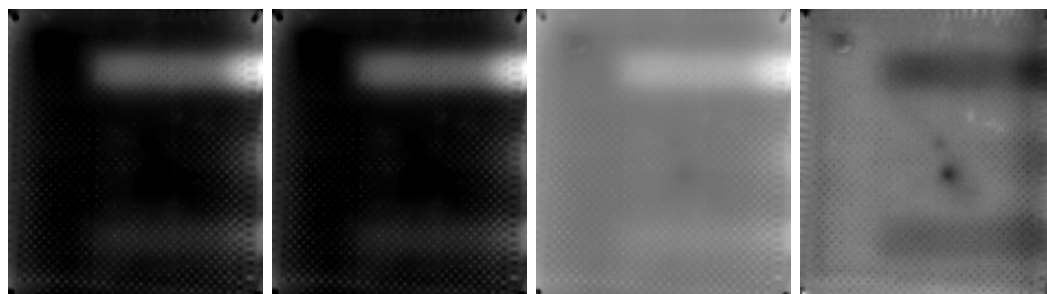
(a) Absolute: step   (b) Running: step   (c) Standard: step   (d) Normalized: step
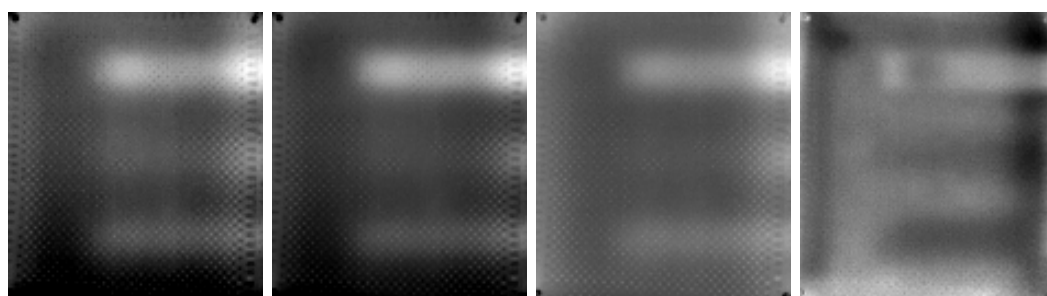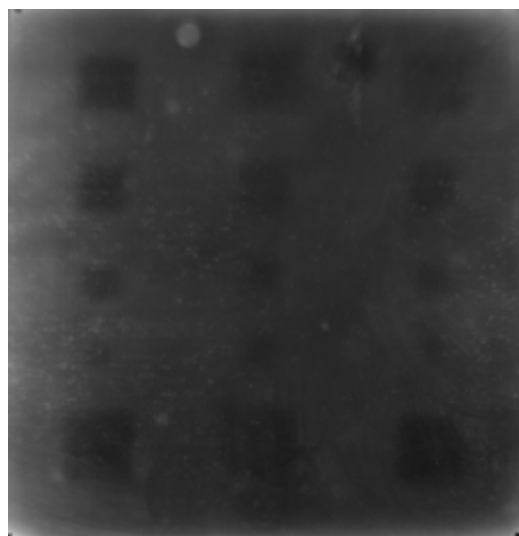
(e) Absolute: square pulse   (f) Running: square pulse   (g) Standard: square pulse   (h) Normalized: square pulse

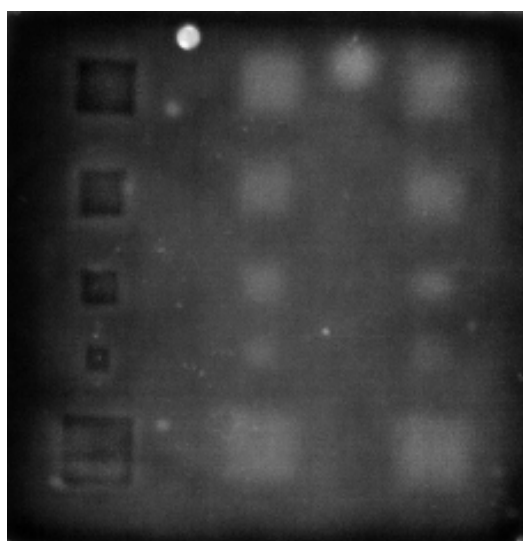Figure G.4: Contrast Definitions for CFRP200DEL
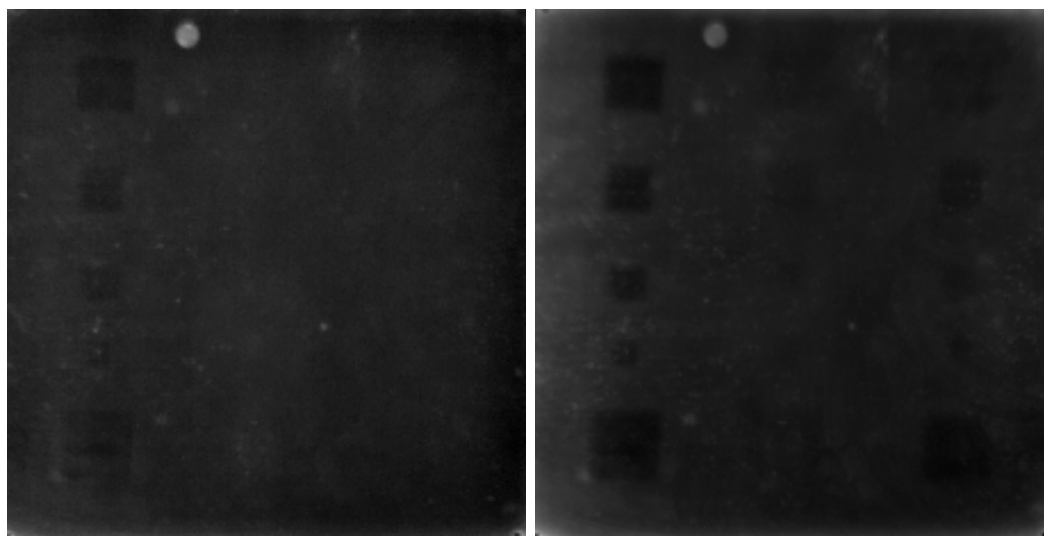
(a) Original image at $t = 6.6$ s

(b) Original image at $t = 25$ s
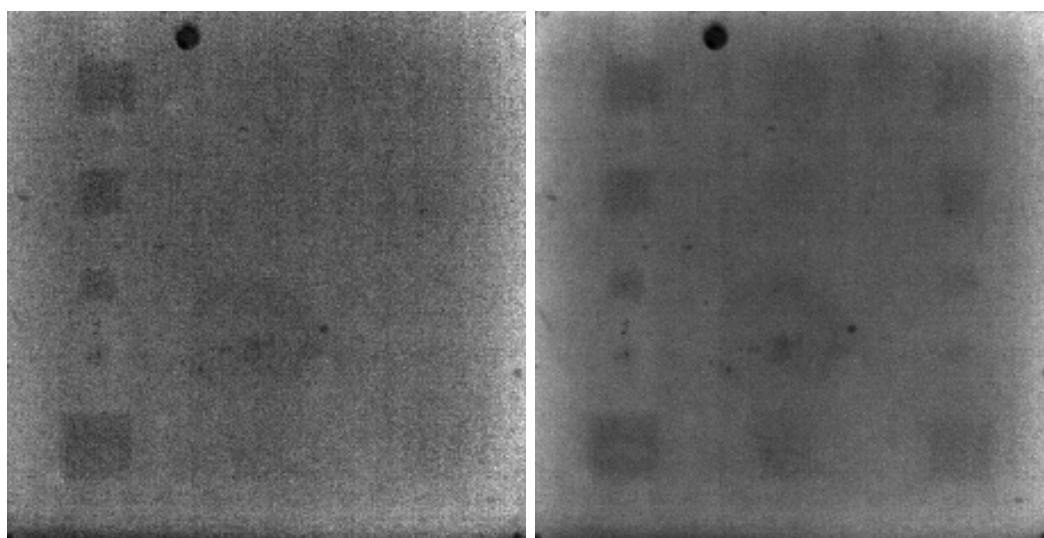
(c) DAC image at $t = 6.6$ s

(d) DAC image at $t = 25$ s
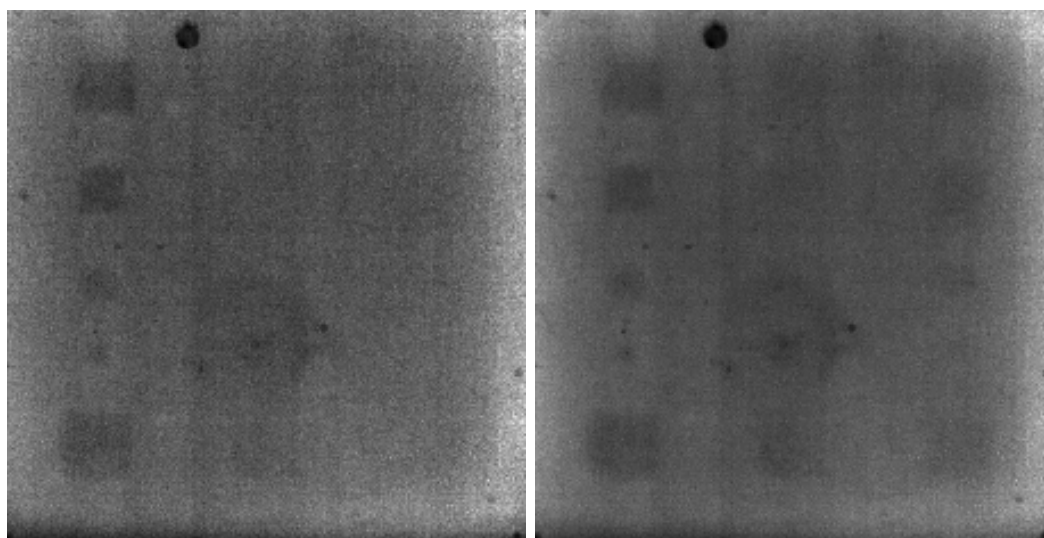
(e) IDAC image at $t = 6.6$ s

(f) IDAC image at $t = 25$ s

Figure G.5: Differential images using DAC on GFRP106A at $t' = 2$ s
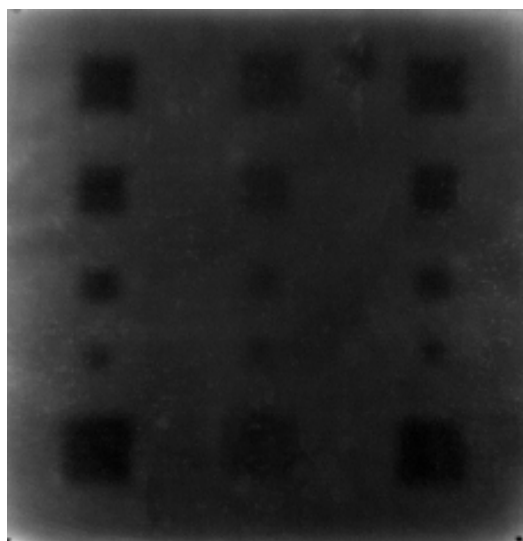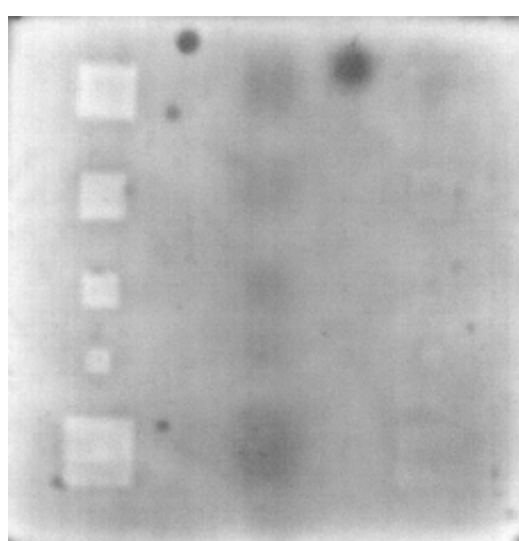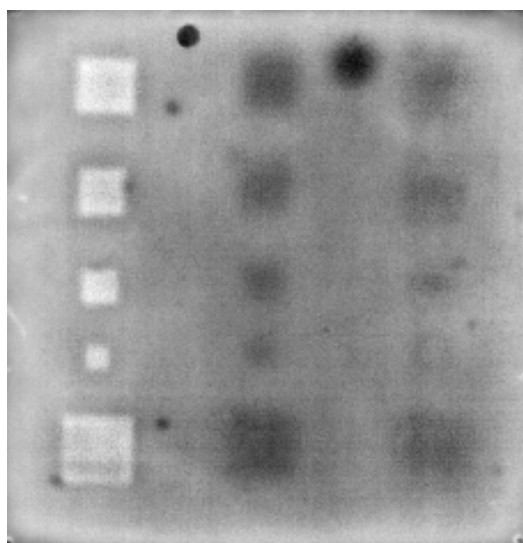
(a) Original images: square pulse
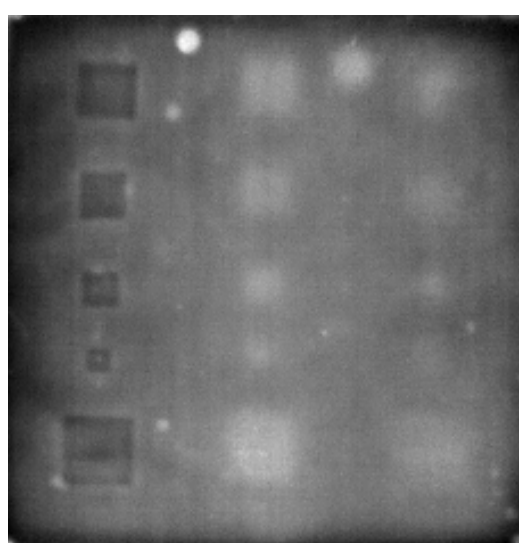
(b) Original images: step

(c) Skewness: square pulse
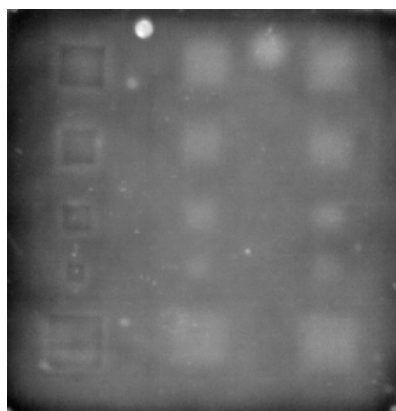
(d) Skewness: step

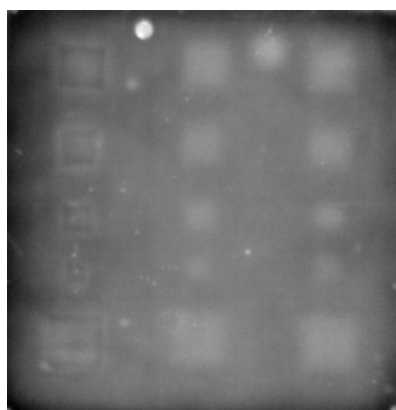(e) Kurtosis: square pulse

(f) Kurtosis: step

Figure G.6: Skewness and Kurtosis Images on GFRP 106A

(a) ACE: square pulse

(b) ACE: step

(c) SAM: square pulse

(d) SAM: step
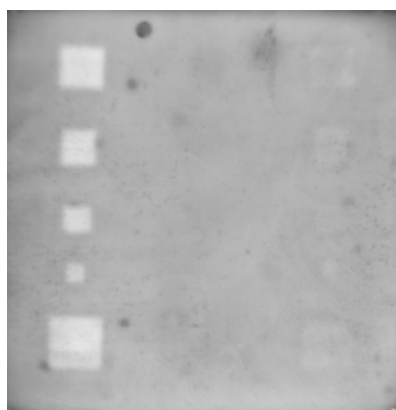
(e) t-statistic: square pulse
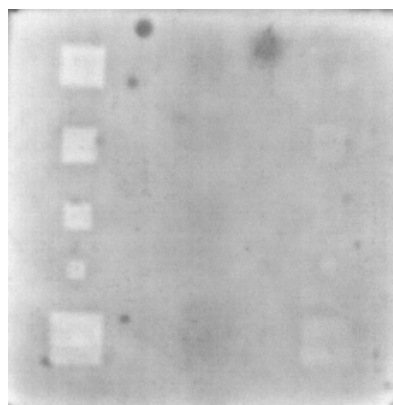
(f) t-statistic: step
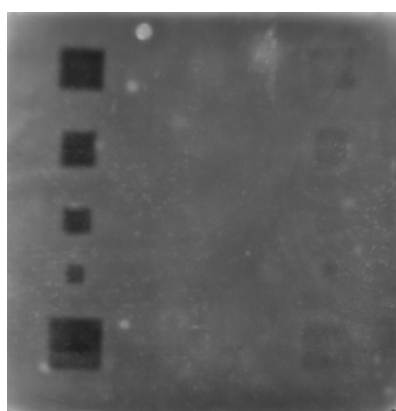
(g) F statistic: square pulse
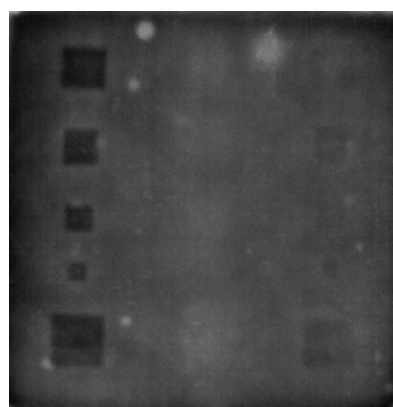
(h) F statistic: step

Figure G.7: Matched Filters on GFRP106A

(a) Original image: square pulse   (b) Original image: step

(c) EOF 2: square pulse   (d) EOF 2: step
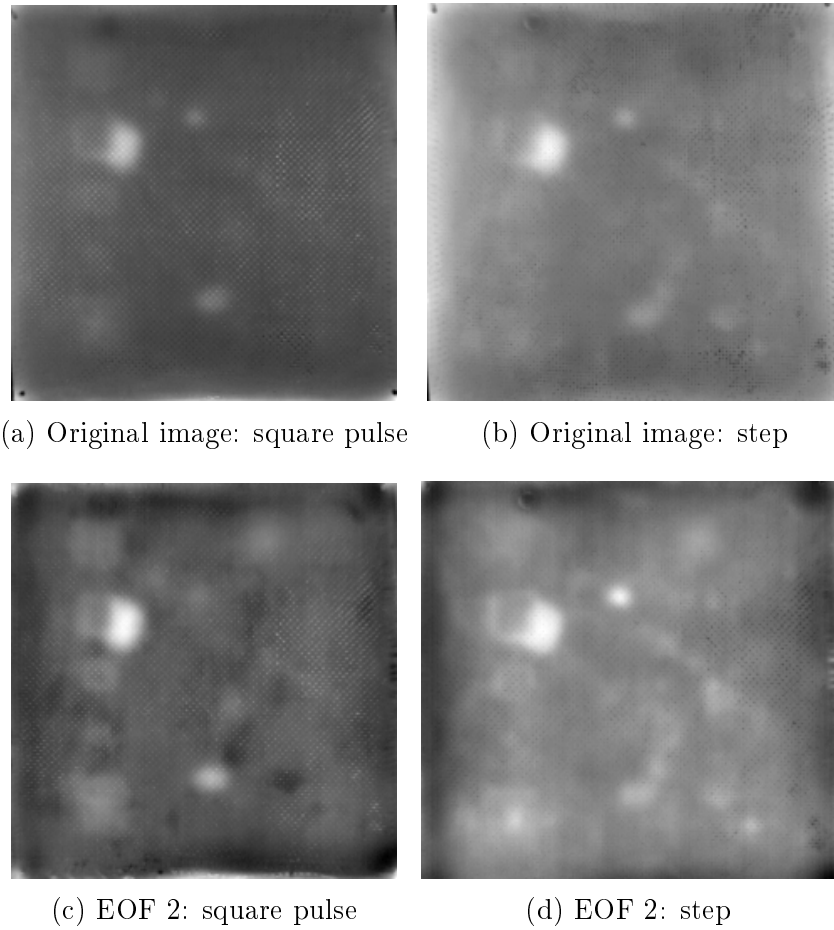
Figure G.8:   Empirical orthogonal functions (EOFs) on CFRP200B

(a) $t_{acq} = 12.5$ s   (b) $t_{acq} = 25$ s   (c) $t_{acq} = 50$ s
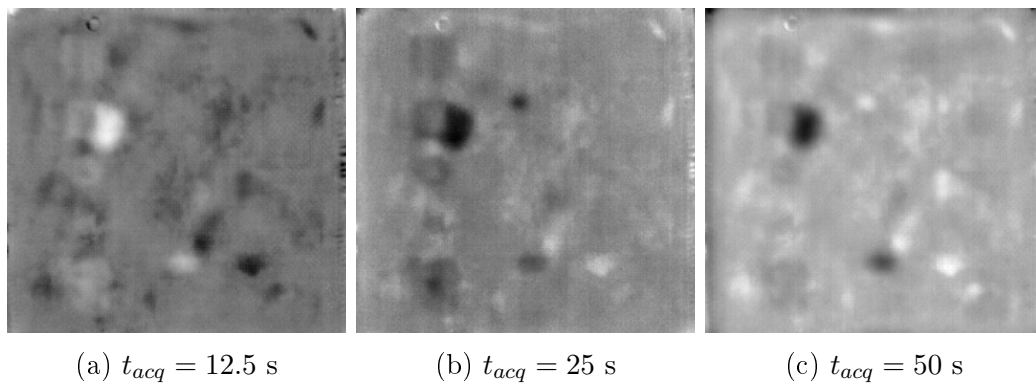
Figure G.9: The effects of acquisition time (t_{acq}) on the second empirical orthogonal function (EOF 2) on CFRP200B for step heating
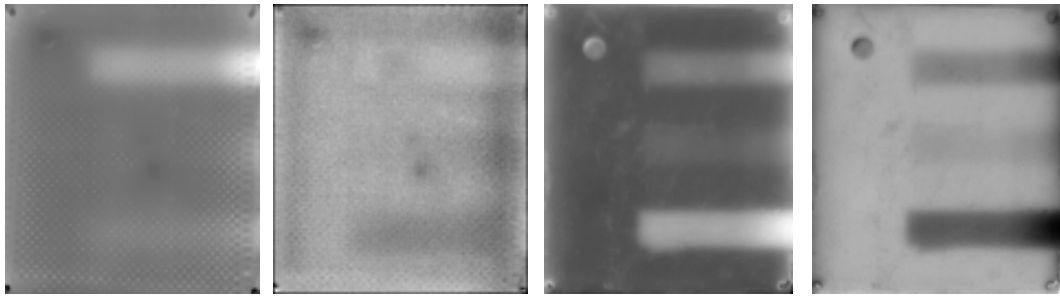
(a) Original image: CFRP200DEL

(b) MEC image: CFRP200DEL

(c) Original image: GFRP200DEL

(d) MEC image: GFRP200DEL

Figure G.10: Markov error contrast (MEC) on air-gap delaminations using step heating
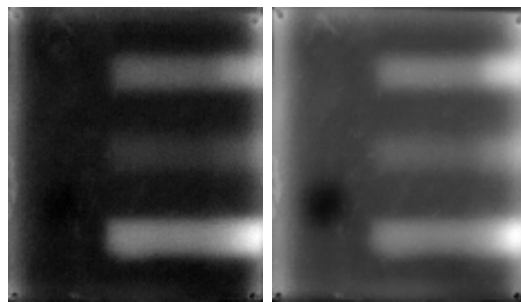
(a) Original Image: $t = 50$ s

(b) TSR Image: $t = 50$ s

Figure G.11: Thermal signal reconstruction (TSR) for the decay of square-pulse heating for a 5th order polynomial
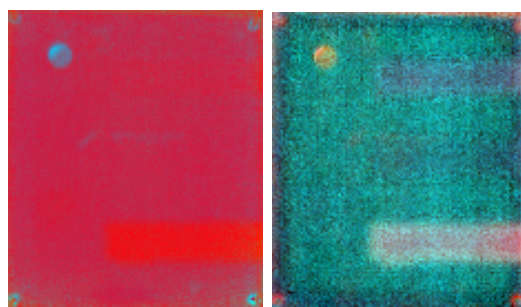
(a) Step

(b) Square Pulse: Decay

Figure G.12: Unique RGB Image for GFRP200DEL

(a) Coeff. a_1 (b) Coeff. a_2 (c) Coeff. a_3

(d) Coeff. a_4 (e) Coeff. a_5 (f) Coeff. a_6
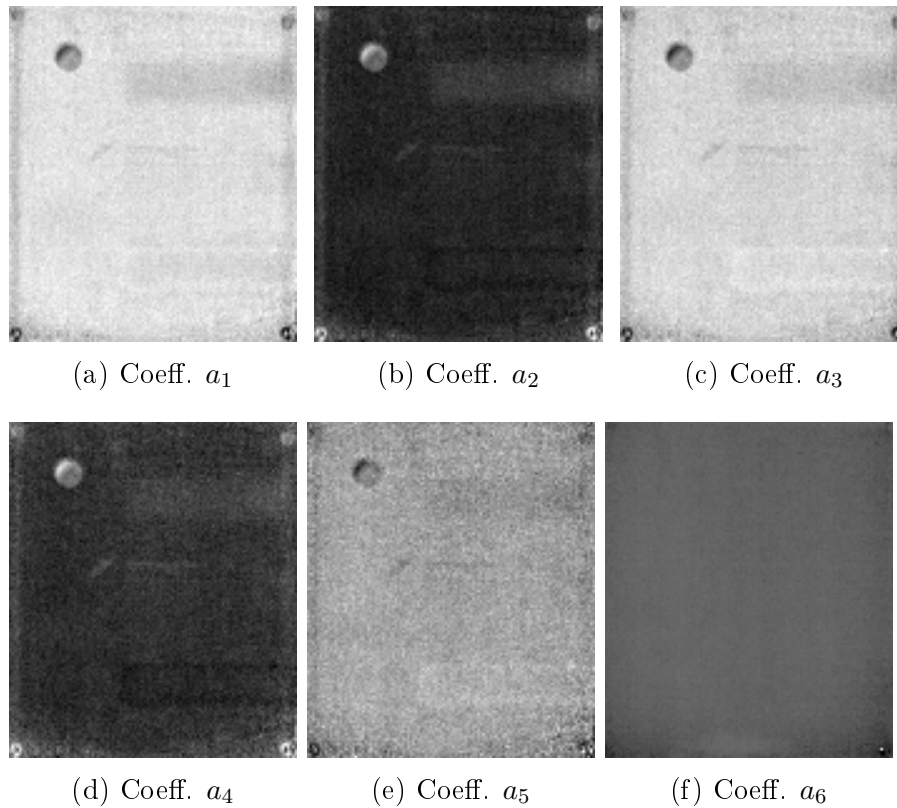
Figure G.13: Thermal signal reconstruction coefficients of a 5th order polynomial: Step heating for GFRP 200DEL
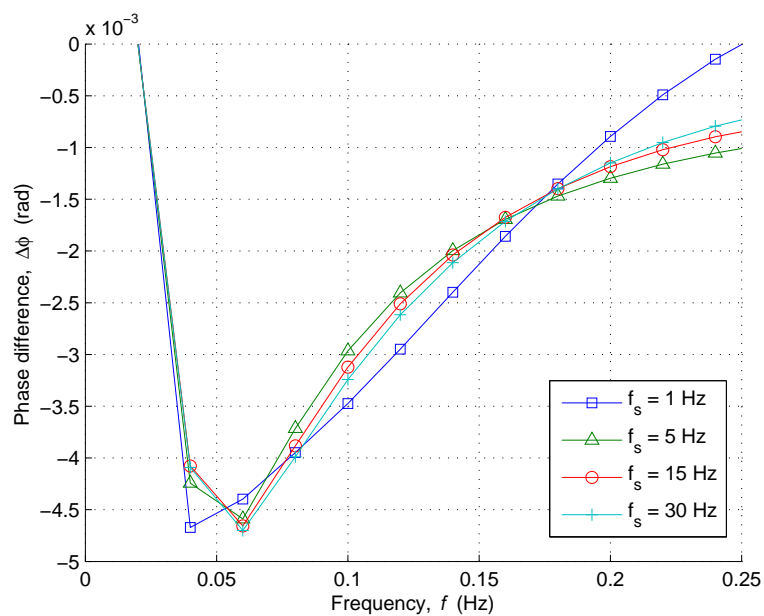
Figure G.14: Phase difference in opaque PMMA sample for a change in sampling frequency f_s

(a) Original image

(b) Amplitude image: $f = 0.04$ Hz

(c) Amplitude image: $f = 0.06$ Hz

(d) Phase image: $f = 0.04$ Hz

(e) Phase image: $f = 0.06$ Hz

(f) Phase image: $f = 0.08$ Hz
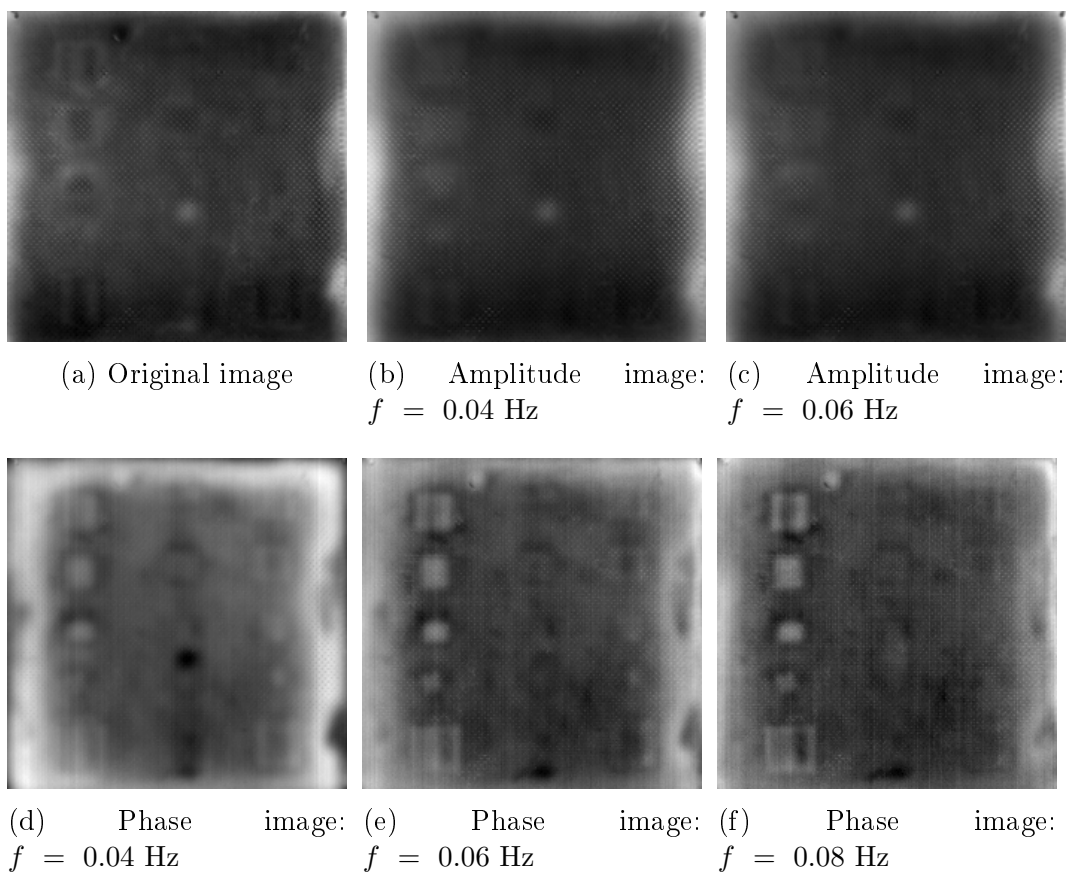
Figure G.15: Fourier transform (FT) on CFRP200A: Step heating

(a) Original image

(b) Amplitude image: $f = 0.04$ Hz

(c) Amplitude image: $f = 0.06$ Hz

(d) Phase image: $f = 0.04$ Hz

(e) Phase image: $f = 0.06$ Hz

(f) Phase image: $f = 0.08$ Hz
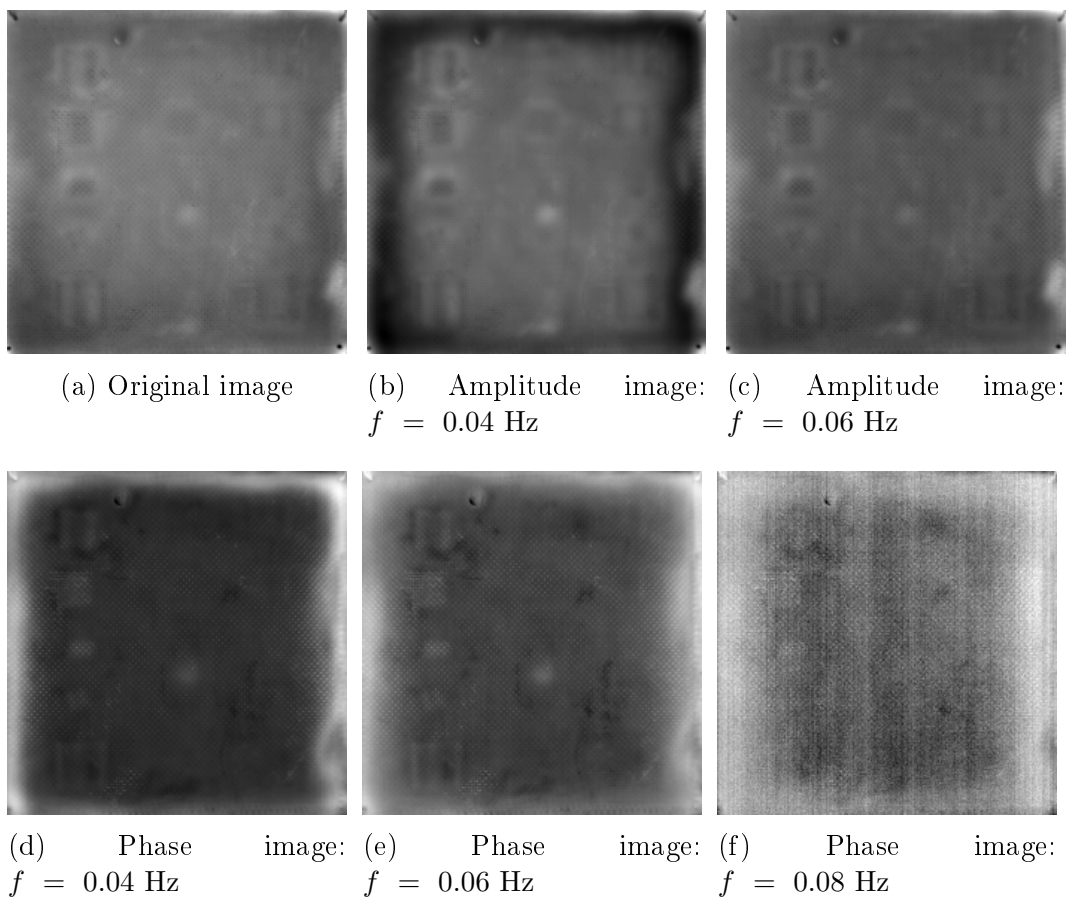
Figure G.16: Fourier transform (FT) on CFRP200A: Square pulse heating
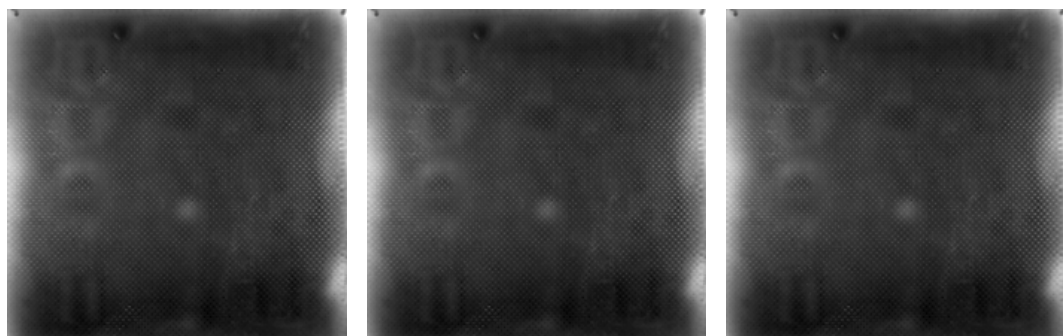
(a) Amplitude image: $t = 18.6$ s

(b) Amplitude image: $t = 24.0$ s

(c) Amplitude image: $t = 33.3$ s
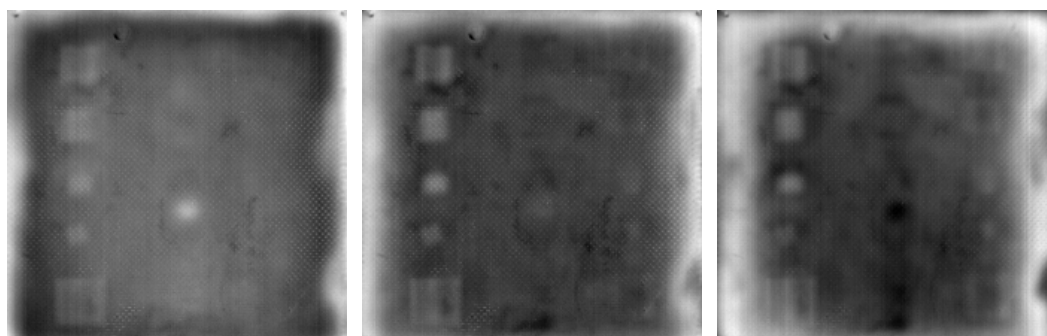
(d) Phase image: $t = 18.6$ s

(e) Phase image: $t = 24.0$ s

(f) Phase image: $t = 33.3$ s

Figure G.17: Wavelet transform (WT) on CFRP 200A: Step heating
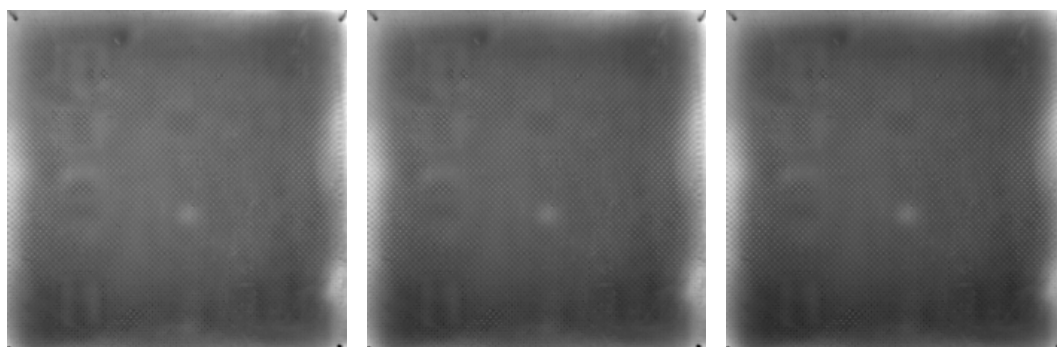
(a) Amplitude image: $t = 18.6$ s

(b) Amplitude image: $t = 24.0$ s

(c) Amplitude image: $t = 33.3$ s
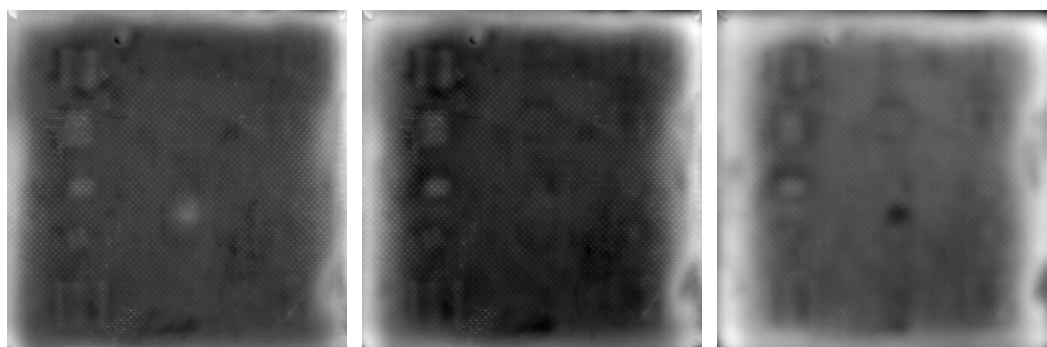
(d) Phase image: $t = 18.6$ s

(e) Phase image: $t = 24.0$ s

(f) Phase image: $t = 33.3$ s

Figure G.18: Wavelet transform (WT) on CFRP 200A: Square pulse heating

(a) Global HE   (b) Adaptive HE   (c) Contrast limited adaptive HE

(d)   Brightness Preserving Dynamic Fuzzy HE

(e)   Quadrant Dynamic HE

(f) Recursive mean-separate HE
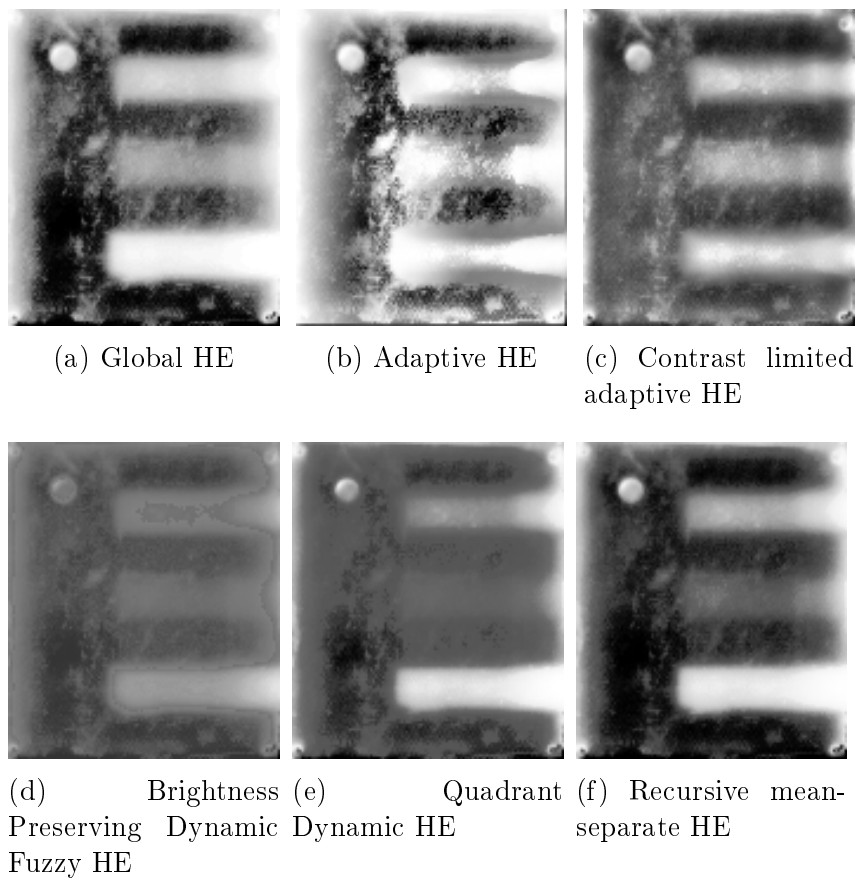
Figure G.19:   Histogram equalization (HE) methods on GFRP 200DEL

(a) Raw: CFRP200B   (b) MSR: CFRP200B

(c) Raw: CFRP200DEL   (d) MSR: CFRP200DEL
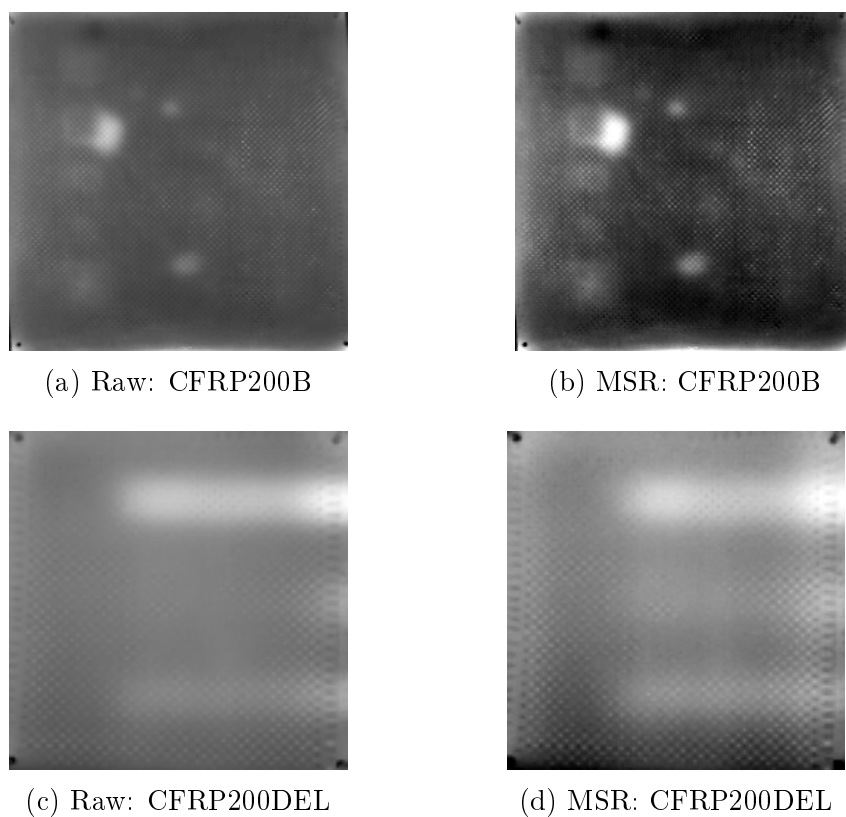
Figure G.20: Multiscale retinex (MSR)

G.3   Industry Samples
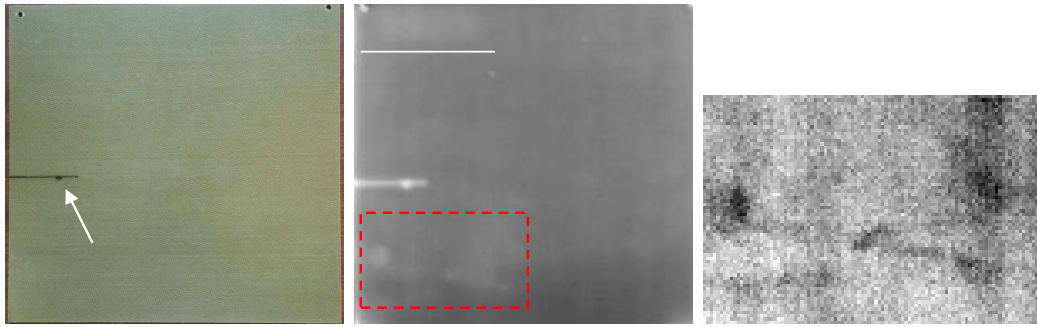
(a) Digital image: Front Side

(b) ACE image: Front Side

(c) Cropped region:PCT
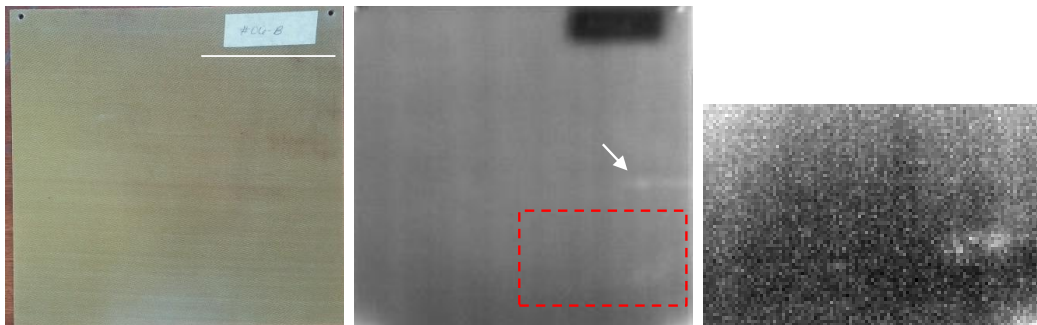
(d) Digital image: Rear Side

(e) ACE image: Rear Side

(f) Cropped region:PCT

Figure G.21: Inspection of welded thermoplastic laminate: Step heating

(a) Digital Image: Control

(b) $f = 0.06$ Hz for square pulse heating: Control

(c) $f = 0.04$ Hz for step heating: Control

(d) Digital Image: Deformed

(e) $f = 0.06$ Hz for square pulse heating: Deformed

(f) $f = 0.04$ Hz for step heating: Deformed
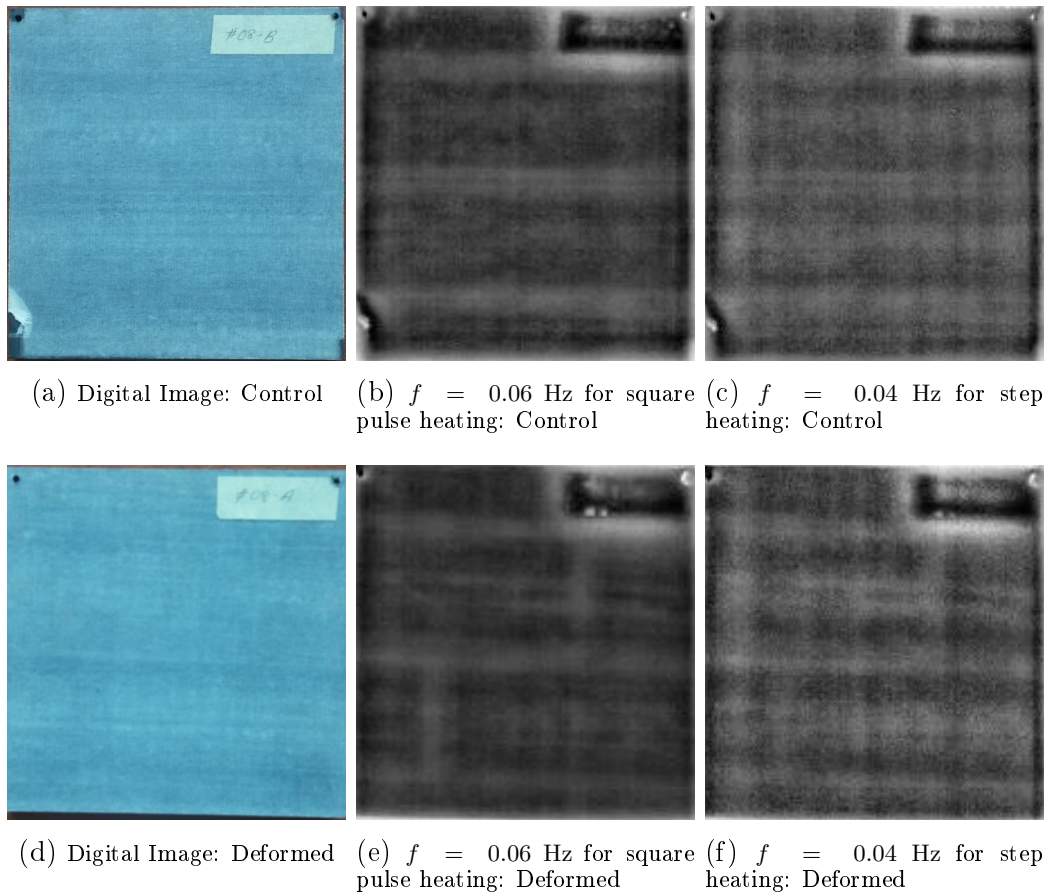
Figure G.22: Fourier transform images post-processed with multiscale retinex for the multi-laminated foam sandwich (2-ply glass & 5-ply unidirectional carbon epoxy with PET foam core)

(a) Digital Image: Front

(b) F statistic: Step heating

(c) EOF 2 in principal component thermography: Square pulse heating

(d) Digital Image: Rear

(e) Skewness: Step heating

(f) Skewness: Square pulse heating
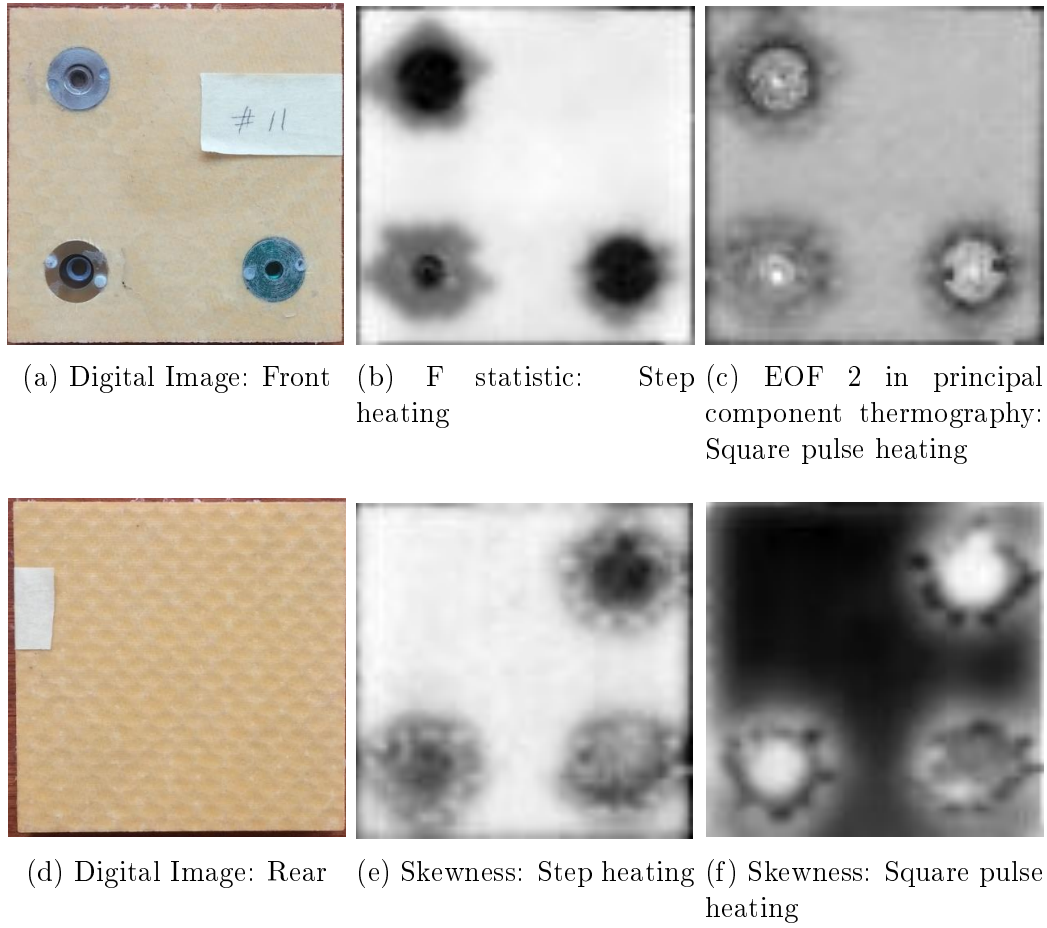
Figure G.23: Various potted inserts in glass-epoxy sandwich composite

(a) Digital Image

(b) Step heating

(c) Square pulse heating
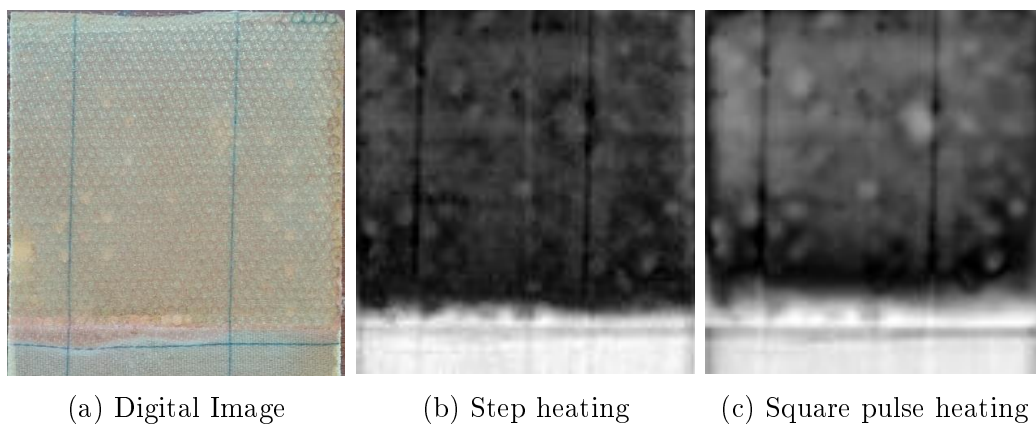
Figure G.24: First empirical orthogonal function (EOF 1) using principle component thermography on 1-ply glass-epoxy spliced composite

(a) Digital Image: Front   (b) EOF 1 using step   (c) EOF 3 using square
                            heating: Front   pulse heating: Front

(d) Digital Image: Rear   (e) EOF 2 using step   (f) EOF 3 using square
                            heating: Rear   pulse heating: Rear
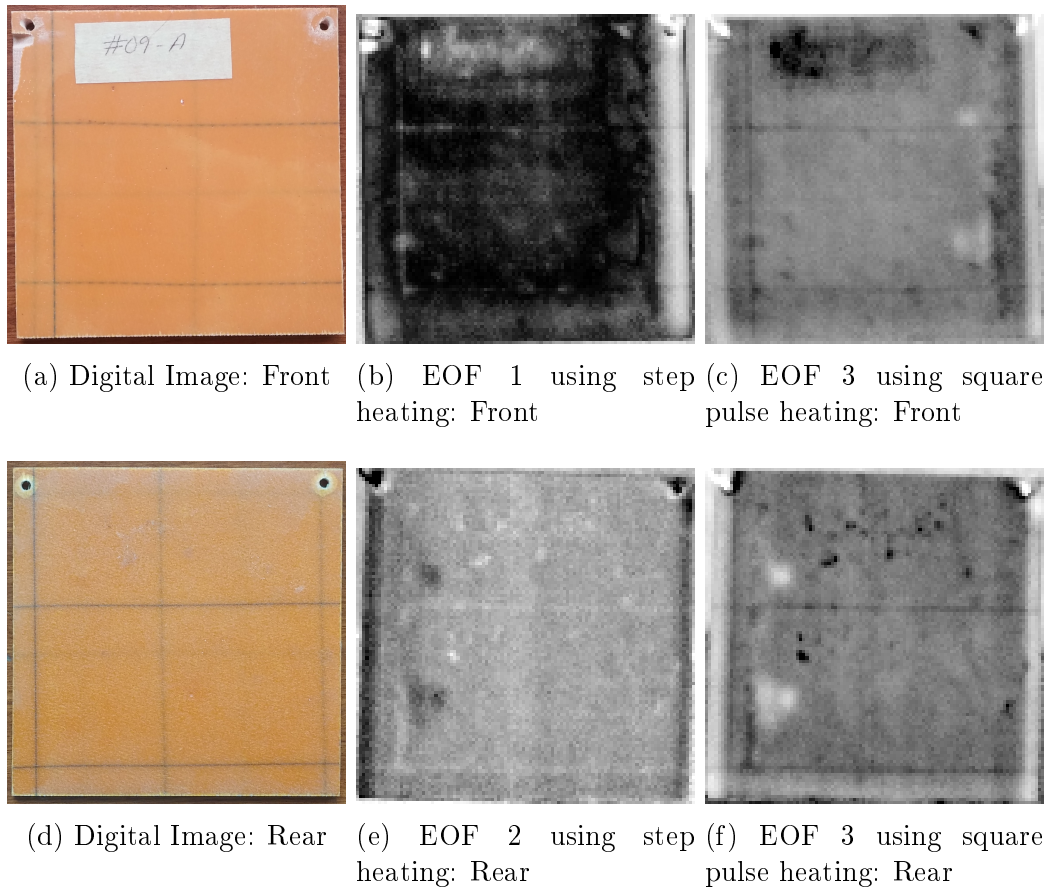
Figure G.25: Void formation in 10-ply glass-phenolic laminate (2.3 mm thick) using best empirical orthogonal function (EOF) in principal component thermography

(a) Digital Image   (b)   Wavelet   transform: (c) Skewness image of the
                          $t = 16$ s   wavelet transform data
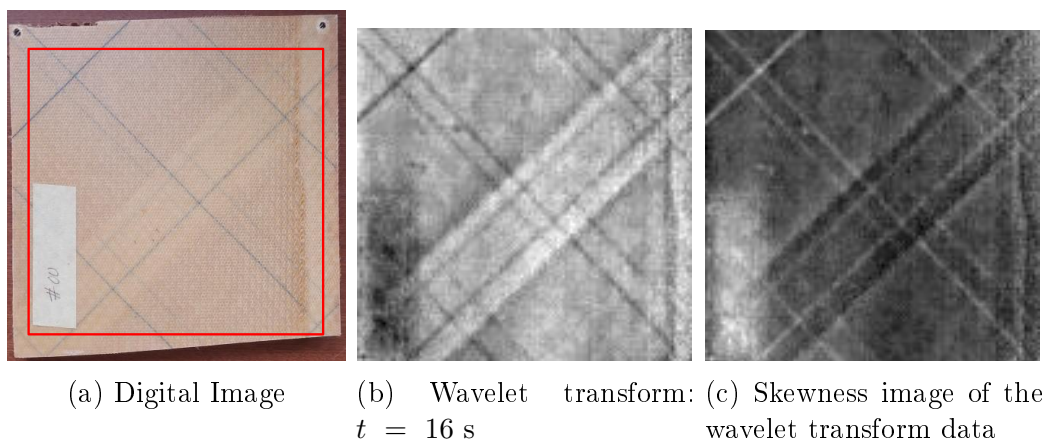
Figure G.26: Rejected Spaceflex part 1: Step heating

(a) Digital Image

(b) Fourier transform image: $f = 0.04$ Hz
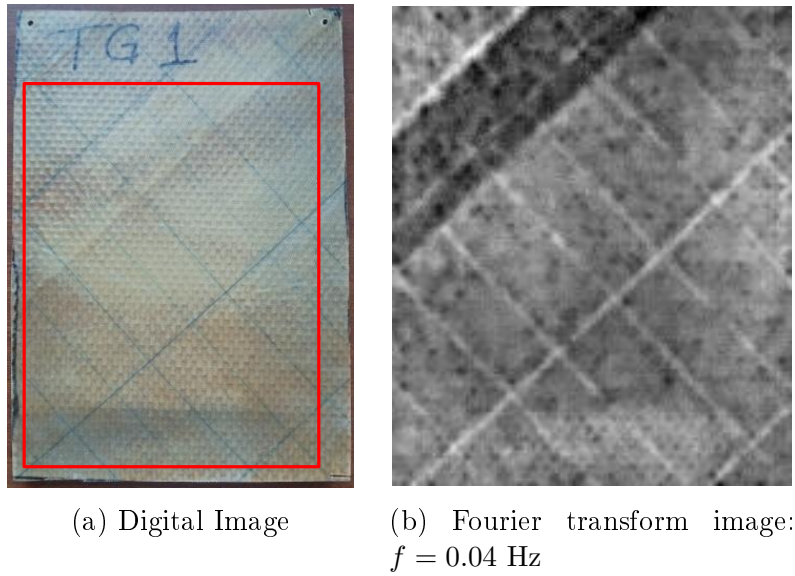
Figure G.27: Rejected Spaceflex part 2: Step heating

(a) Digital Image

(b) Kurtosis and multiscale retinex image
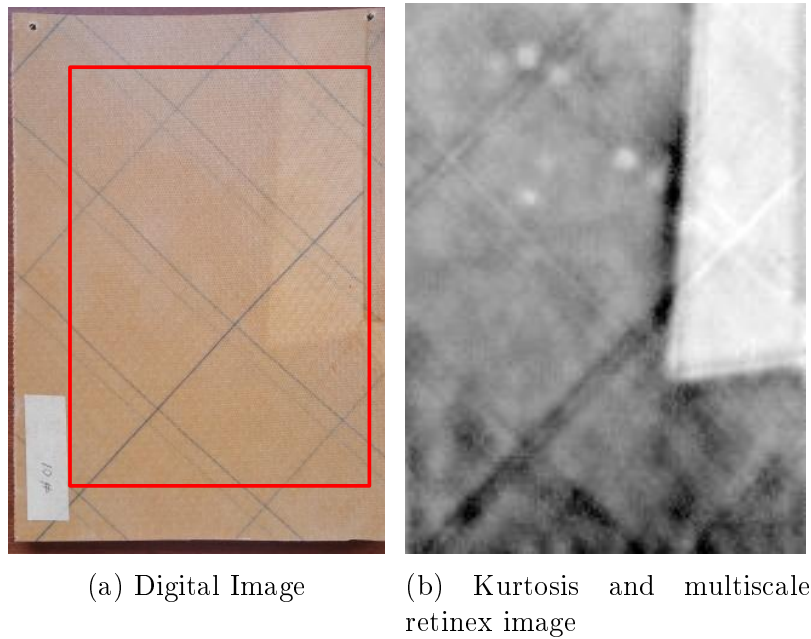
Figure G.28: Rejected Spaceflex part 3: Square pulse heating

(a) Digital Image

(b) Fourier transform image: $f = 0.04$ Hz

Figure G.29: Rejected Spaceflex part 4: Step heating

Table G.1: Measured defect size

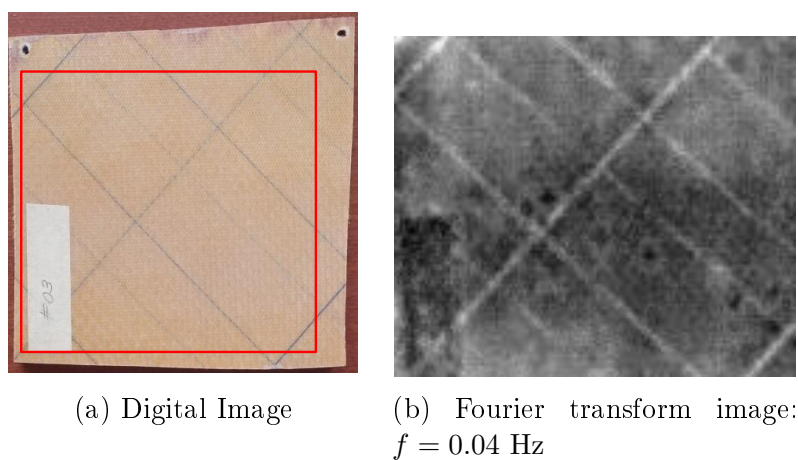| Sample:	D_{actual} mm	Depth 1			Depth 2			Depth 3		
		z mm	D_{meas} mm	Error %	z mm	D_{meas} mm	Error %	z mm	D_{meas} mm	Error %
GFRP200	10	1.35	10	0.0	2.70	11.00	10.0	4.05	12.00	20
	15	1.35	17	13.3	2.70	16.00	6.7	4.05	15.00	0.0
	20	1.35	20	0.0	2.70	21.00	5.0	4.05	22.00	10.0
	25	1.35	25	0.0	2.70	25.00	0.0	4.05	23.00	-8.0
	30	1.35	28	-6.7	2.70	30.00	0.0	4.05	28.00	-6.7
GFRP106A	10	1.31	10	0.0	2.62	10.00	0.0	3.93	9.00	-10.0
	15	1.31	15	0.0	2.62	16.00	6.7	3.93	14.00	-6.7
	20	1.31	20	0.0	2.62	20.00	0.0	3.93	20.00	0.0
	25	1.31	25	0.0	2.62	25.00	0.0	3.93	26.00	4.0
	30	1.31	30	0.0	2.62	31.00	3.3	3.93	31.00	3.3
GFRP106B	10	0.60	10	0.0	1.21	10.00	0.0	1.81	9.00	-10.0
	15	0.60	15	0.0	1.21	15.00	0.0	1.81	16.00	6.7
	20	0.60	20	0.0	1.21	20.00	0.0	1.81	20.00	0.0
	25	0.60	25	0.0	1.21	25.00	0.0	1.81	25.00	0.0
	30	0.60	30	0.0	1.21	30.00	0.0	1.81	30.00	0.0
CFRP200A	10	1.38	n/a	-	2.76	n/a	-	4.13	n/a	-
	15	1.38	15	0.0	2.76	n/a	-	4.13	n/a	-
	20	1.38	20	0.0	2.76	21.00	5.0	4.13	n/a	-
	25	1.38	26	4.0	2.76	27.00	8.0	4.13	n/a	-
	30	1.38	32	6.7	2.76	27.00	-10.0	4.13	n/a	-
CFRP200B	10	1.42	9.00	-10.00	2.84	n/a	-	4.26	n/a	-
	15	1.42	17.00	13.33	2.84	n/a	-	4.26	n/a	-
	20	1.42	23.00	15.00	2.84	n/a	-	4.26	n/a	-
	25	1.42	24.00	-4.00	2.84	n/a	-	4.26	n/a	-
	30	1.42	34.00	13.33	2.84	n/a	-	4.26	n/a	-
CFRP200DEL	15	1.65	15	0.0	3.29	10.00	-33.3	4.94	9.00	-40.0
GFRP200DEL	15	1.28	15	0.0	2.55	15.00	0.0	3.83	15.00	0.0
Clear PMMA Circle	15	2.00	12	-20.0	5.00	n/a		7.00	n/a	-
	15	2.00	16	6.7	5.00	12.00	-20.0	7.00	n/a	-
	20	2.00	21	5.0	5.00	17.00	-15.0	7.00	n/a	-
	25	2.00	26	4.0	5.00	22.00	-12.0	7.00	n/a	-
	30	2.00	32	6.7	5.00	26.00	-13.3	7.00	n/a	-
Opaque PMMA Circle	10	1.00	11	10.0	2.00	9.00	-10.0	3.00	11.00	10.0
	15	1.00	16	6.7	2.00	15.00	0.0	3.00	15.00	0.0
	20	1.00	22	10.0	2.00	21.00	5.0	3.00	20.00	0.0
	25	1.00	27	8.0	2.00	25.00	0.0	3.00	24.00	-4.0
	30	1.00	31	3.3	2.00	31.00	3.3	3.00	30.00	0.0
Clear PMMA Square	10	2.00	10	0.0	5.00	12.00	20.0	7.00	n/a	-
	15	2.00	13	-13.3	5.00	12.00	-20.0	7.00	n/a	-
	20	2.00	19	-5.0	5.00	22.00	10.0	7.00	n/a	-
	25	2.00	24	-4.0	5.00	26.00	4.0	7.00	n/a	-
	30	2.00	29	-3.3	5.00	31.00	3.3	7.00	n/a	-
Opaque PMMA Square	10	1.00	10	0.0	2.00	11.00	10.0	3.00	12.00	20.0
	15	1.00	14	-6.7	2.00	15.00	0.0	3.00	16.00	6.7
	20	1.00	22	10.0	2.00	21.00	5.0	3.00	21.00	5.0
	25	1.00	25	0.0	2.00	26.00	4.0	3.00	27.00	8.0
	30	1.00	29	-3.3	2.00	32.00	6.7	3.00	31.00	3.3
Maximum Error				20.0			33.3			40.0

References

Abate, J & Whitt, W, 2006. "A Unified Framework for Numerically Inverting Laplace Transforms", Informs Journal of Computing, Vol.18, No.4, pp.408-421.

Abdel-Qader, I, Yohali, S, Abudayyeh, O & Yehia, S, 2008. "Segmentation of Thermal Images for Non-destructive Evaluation of Bridge Decks", Nondestructive Testing & Evaluation International, Vol.41, No.5, pp.395-405.

Abdullah-Al-Wadud, M, Hasanul Kabir, M,D, Ali Akber Dewan, M, & Chae, O, 2007. "A Dynamic Histogram Equalization for Image Contrast Enhancement", IEEE Trans., Consumer Electronics, Vol.53, No.2, pp.593-600.

Almond, D.P & Lau, S.K, 1994. "Defect Sizing by Transient Thermography. I: An Analytical Treatment", Journal of Physics D: Applied Physics, Vol.27, Issue 5, pp.1063-1069.

Allport, J.J & McHugh, S.L, 1988. "Quantitative Evaluation of Transient Video Thermography", in Review of Progress in Quantitative Nondestructive Evaluation, Thompson, D.O & Chimenti, D.E (Eds.), Vol.7A, pp.253-262.

AMT Composites, 2015. Ampreg 21 Epoxy Laminating System. Available [Online]: http://www.amtcomposites.co.za/products/epoxy-polyester-systems/epoxy-laminating-resins/ampreg-21-epoxy-laminating-system. (Accessed 17 October 15).

Badghaish, A.A & Fleming, D.C, 2008. "Non-destructive Inspection of Composites Using Step Heating Thermography", Journal of Composite Materials, Vol.42, No.13, pp.1337-1357.

Bai, X, Zhou, F & Xue, B, 2011. "Infrared Image Enhancement Through Contrast Enhancement by Using Multiscale New Top-hat Transform", Infrared Physics & Technology, Vol.54, pp.61-69.

Balageas, D.L, Déom, A.A & Boscher, D.M, 1987. "Characterization and Non-destructive Testing of Carbon-Epoxy Composites by a Pulsed Photothermal

Method", Materials Evaluation, Vol.45, No.4, pp.466-465.

Balageas, D.L, Delpech, Ph, Boscher, D & Déom, A, 1991. "New Developments in Stimulated Infrared Thermography Applied to Nondestructive Testing of Laminates", Rev. of Progress in QNDE 10A, pp.1073-1081.

Balageas, D.L, 2012. "Defense and Illustration of Time-resolved Pulsed Thermography for NDE", Quantitative InfraRed Thermography, Vol.9, No.1, pp.3-32.

Balageas, D, 2013. "In Search of Early Time: An Original Approach in the Thermographic Identification of Thermophysical Properties and Defects", Advances in Optical Technologies.

Balageas, D.L, Roche, J.M, Leroy, F.H, Gorbach, A.M, , 2013. "The Thermographic Signal Reconstruction Method: A Powerful Tool for the Enhancement of Transient Thermographic Images" CB Seminar 2013 on "Advances of IR-thermal Imaging in Medicine", Warsaw, Poland.

Balageas, D.L, Roche, J, Leroy, F, Liu, W & Gorbach, A.M, 2014. "The Thermographic Signal Reconstruction Method: A Powerful Tool For the Enhancement of Transient Thermographic Images", Biocybernetics and Biomedical Engineering, Vol.35, Issue 1, pp.1?9.

Balageas D & Roche J.M, 2014. "Common Tools for Quantitative Time-resolved Pulse and Step Heating Thermography, Part I: Theoretical Basis", Quantitative InfraRed Thermography Journal.

Benítez, H, Maldague, X, Ibarra-Castanedo, C, Loaiza, H, Bendada, A & Caicedo, E, 2006. "Modified Differential Absolute Contrast Using Thermal Quadrupoles for the Nondestructive Testing of Finite Thickness Specimens by Infrared Thermography", in Electrical and Computer Engineering, CCECE, pp.1039-1042.

Benítez, H, Ibarra-Castanedo, C, Bendada, A, Maldague, X, Loaiza, H & Caicedo, E, 2008. "Definition of a New Thermal Contrast and Pulse Correction for Defect Quantification in Pulsed Thermography", Infrared Physics & Technology, Vol.51, pp.160-167.

Benítez, H.D, Loaiza, H, Caicedo, E, Ibarra-Castanedo, C, Bendada, A & Maldague, X, 2009. "Defect Characterization in Infrared Non-destructive Testing with Learning Machines", NDT & E International, Vol.42, pp.630-643.

Biju, N, Ganesan, N, Krishnamurthy, C.V, & Balasubramaniam, K, 2009. "Frequency Optimization for Eddy Current Thermography". NDT & E Inter-

national, Vol.42, No.5, pp.415-420.

Birks, A.S & Green, R.E, 1991. "Ultrasonic Testing", in American Society for Nondestructive Testing, McIntire, P (Ed.), 2nd Edition, Columbus, OH.

Blumm, J, Lindemann, A, Meyer, M & Strasser, C, 2010. "Characterization of PTFE Using Advanced Thermal Analysis Technique". International Journal of Thermophysics, Vol.31, Issue 10, pp.1919-1927.

Borokov, A.A, 1999. "Mathematical Statistics", Taylor & Francis.

Brigante, D, 2014. "New Composite Materials: Selection, Design and Application", Springer International Publishing Switzerland, 1st Edition.

Busse, G & Rosencwaig, A, 1980. "Subsurface Imaging with Photoacoustics", Appl. Phys. Lett., Vol.36, No.10, pp.815-816.

Busse, G, Wu, D, and Karpen, W, 1992. "Thermal Wave Imaging with Phase Sensitive Modulated Thermography", Journal of Applied Physics, Vol.71, No.8, pp.3962-3965.

Butler, M.J.A, Mouchot, M.C, Barale, V & LeBlanc, C, 1988. "The application of remote sensing technology to marine fisheries: an introductory manual", FAO Fisheries Technical Paper 295, pp.165.

Çengal, Y.A, & Ghajar, A.J, 2011. "Heat and Mass Transfer: Fundamentals and Applications", New York, McGraw-Hill, 4th Edition in SI units.

Carlslaw, H.S & Jaeger, J.C, 1959. "Conduction of heat in Solids", Oxford University Press, London.

Carslaw, H & Jaeger, J, 1986. "Conduction of Heat in Solids", 2nd Edition, Oxford: Claredon Press.

Cernuschi, F, Bison, P.G, Marinetti, S, Figari, A, Lorenzoni, L & Grinzato, E, 2002. "Comparison of Thermal Diffusivity Measurement Techniques", in Proceedings of the 6th Conference on Quantitative Infrared Thermography, Balageas, D, Busse, G, Carlomagno, G.M & Vaic, S (Eds.), Dubrovnik, Croatia.

Choi, M, Kang, K, Park, J, Kim, W & Kim, K, 2008. "Quantitative Determination of a Subsurface Defect of Reference Specimen by Lock-in Infrared Thermography" NDT & E International, Vol.41, pp.119-124.

Cielo, P, Maldague, X, Déom, A,A & Lewak, R, 1987. "Thermographic Non-destructive Evaluation of Industrial Materials and Structures", Material Evaluation, Vol.45, pp.452-460.

Ciliberto, A, Cavaccini, G, Salvetti, O, Chimenti, M, Azzarelli, L, Bison, P.G, Marinetti, S, Freda, A & Grinzato, E, 2002. "Porosity Detection in Composite Aeronautical Structures", Journal of Infrared Physics & Technology, Vol.43, pp.139-143.

Drury, J.C, 2004. "Ultrasonic Flaw Detection for Technicians", Silverwing Ltd., 3rd Edition.

Dumoulin J, Ibos L, Marchetti M & Mazioud A, 2011. "Detection of Non Emergent Defects in Asphalt Pavement Samples by Long Pulse and Phase Infrared Thermography", European Journal of Environmental and Civil Engineering, Vol.15, pp.557-574.

Eevblog, 2014. Flir E4 Thermal Imaging Camera Teardown. Available [Online]: http://www.eevblog.com/forum/testgear/flir-e4-thermal-imaging-camera-teardown/msg378926/#msg378926. (Accessed 27 August 15).

Favro, L.D, Han, X, Kuo, P.K, & Thomas, R.L, 1994. "Improving the Resolution of Pulsed Thermal Wave Images with a Simple Inverse Scattering Technique", Journal De Physique IV France, Vol.4, pp.C7-545:C7-550.

Findeis, D, Hobson, O & Gryzagoridis, J, 2014. "Low Cost Digital Shearography Prototype", In Advancement of Optical Methods in Experimental Mechanics, Springer International Publishing, Vol.3, pp.267-274.

FLIR Systems: Indigo Operations, 2008. RTools Application Note: Background Offset Correction. Available [Online]: http://flir.custhelp.com/ci/fattach/get/1667/. (Accessed 30 August 15).

Florence, J.M, Allshouse, C.C, Glaze, F.W, & Hahner, C.H, 1950. "Absorption of Near-Infrared Energy by Certain Glasses", Journal of Research of the National Bureau of Standards, Vol.45, No.2, Research Paper 2118.

Fourier, J.B.J, 1952. "Analytical Theory of Heat", Encyclopedia Britannica, Inc., Chicago IL.

Foy, B, 2009. "Overview of Target Detection Algorithms for Hyperspectral Data", Los Alamos National Laboratory, Tech. Rep. LA-UR-09-00593.

Galmiche, F & Maldague, X, 2000. "Depth Defect Retrieval Using the Wavelet Pulsed Phased Thermography", In Proc. Eurotherm Seminar, No.64, pp.194-199.

Gaussorgues, G & Chomet, S, 2012. "Infrared Thermography", Microwave and RF Techniques and Applications, Springer Netherlands.

González, D, Ibarra-Castanedo, C, Pilla, M, Klein, M & Maldague, X, 2004a. "Automated Differential Absolute Contrast", Quantitative Infrared Thermography.

González, D, Ibarra-Castanedo, C, Pilla, M, Klein, M, López-Higuera, J & Maldague, X, 2004b. "Automatic Interpolated Differentiated Absolute Contrast Algorithm for the Analysis of Pulsed Thermographic Sequences", in Proceedings of 7th International Conference on Quantitative Infrared Thermography, Balageas, D, Buchlin, J, Carlomagno, G, & Busse, G (Eds.), pp.H.16.1-H.16.6, Bruxelles, Belgique.

Gonzalez, D, Ibarra-Castanedo, C, Lopez-Higuera, J & Maldague, X, 2006a. "New Algorithm Based on the Hough Transform for the Analysis of Pulsed Thermographic Sequences", Nondestructive Testing and Evaluation International, Vol.39, pp.617-662.

González, D, Ibarra-Castanedo, C, Madruga, F & Maldague, X, 2006b. "Differentiated Absolute Phase Contrast Algorithm for the Analysis of Pulsed Thermographic Sequences", Infrared Physics & Technology, Vol.48, pp.16-21.

Gonzalez, R.C & Woods, R.E, 2010. "Digital Image Processing", Upper Saddle River: Pearson Education, Inc.

Griffiths, T.A, 2011. "Enhancing Multispectral Imagery of Ancient Documents", Master's Thesis, Utah State University.

Grys, S & Minkina, W, 2010. "Filtered Contrast in Defect Characterization Using Active Infrared Thermography", Measurement Automation and Monitoring, Vol.56, Issue 8, pp.893-896.

Han, X, Favro, L.D, Kuo, P.K & Thomas, R.L, 1996. "Early-Time Pulse-echo Thermal Imaging", in Review of Progress in Quantitative Nondestructive Evaluation, Thompson, D.O & Chimenti, D.E (Eds.), Vol.15, Plenum Press, New York.

Henke, S, Karstädt, D, Möllmann, K.P, Pinno, F & Vollmer, M, 2004. "Identification and Suppression of Thermal Reflections in Infrared Thermal Imaging",

Inframation: The Thermographic Conference, Vol.5, pp.287-298.

Hidalgo-Gato, R, Andrés, J.R, López-Higuera, J.M, Madruga, F.J, 2013. "Quantification by Signal to Noise Ratio of Active Infrared Thermography Data Processing Techniques", Optics & Photonics Journal, Vol.3, pp.20-26.

Ibarra-Castanedo, C, Gonzalez, D, Klein, M, Pilla, M, Vallerand, S, and Maldague, X, 2004a. "Infrared Image Processing and Data Analysis", Infrared Physics & Technology, Vol.46, pp.75-83.

Ibarra-Castanedo, C, González, D & Maldague, X, 2004b. "Automatic Algorithm for Quantitative Pulsed Phase Thermography Calculations", 16th World Conference on NDT, Montreal, Quebec.

Ibarra-Castanedo, C & Maldague, X, 2004c. "Defect Depth Retrieval from Pulsed Phase Thermographic Data on Plexiglas and Aluminum Samples", Thermosense XXVI, Proc. SPIE, Vol.5405, pp.348-356, Orlando.

Ibarra-Castanedo, C, 2005. "Quantitative Subsurface Defect Evaluation by Pulsed Phase Thermography:Depth Retrieval with the Phase". Ph. D. Thesis, Laval University, Quebec.

Ibarra-Castanedo, C & Maldague, X, 2005. "Interactive Methodology for Optimized Defect Characterization by Quantitative Pulsed Phase Thermography", Research in Nondestructive Evaluation, Vol.16, No.4, pp.1-19.

Ibarra-Castanedo, C, Gonzalez, D, Galmiche, F, Maldague, X & Bendada, A.H, 2006. "Discrete Signal Transforms as a Tool for Processing and Analyzing Pulsed Thermographic Data", Proc. SPIE Thermosense-XXVIII, Vol.6205.

Ibarra-Castanedo, C Benítez, H Maldague, X & Bendada, A, 2007. "Review of Thermal-contrast-based Signal Processing Techniques for the Nondestructive Testing and Evaluation of Materials by Infrared Thermography", In Proceedings of International Workshop on Imaging NDE, Kalpakkam, India, pp.1-6.

Ibarra-Castanedo, C, Benitez, H, Maldague, X & Bendada, A, 2007. "Review of Thermal-Contrast-Based Signal Processing Techniques for the Nondestructive Testing and Evaluation of Materials by Infrared Thermography", International Workshop on Imaging Nondestructive Evaluation.

Ibarra-Castanedo, C, Piau, J, Guilbert, S, Avdelidis, N, Genest, M, Bendada, A & Maldague, X, 2009. "Comparative Study of Active Thermography Techniques for NDE of Honeycomb Structures". Research in Nondestructive Eval-

uation, Vol.20, pp.1-31.

Ishikawa, M, Hatta, H, Utsunomiya, S, 2013. "Effects of Heating Duration on Pulse Phase Thermographic Non-Destructive Testing", Journal of Infrared Physics & Technology, Vol.61, pp.216-223.

Jobson, D.J, Rahman, Z & Woodell, G.A, 1997. "A Multiscale Retenix for Bridging the Gap Between Colour Images and the Human Observation of Scenes", IEEE Transactions on Image Processing, Vol.6, No.7, pp.965-976.

Karbhari, V.M, 2013. "Non-Destructive Evaluation (NDE) of Polymer Matrix Composites" Elsevier, Technology & Engineering, pp.300-350.

Kass, M, Witkin, A & Terzopoulos, D, 1988. "Snakes: Active Contour Models", International Journal of Computer Vision, Vol.1, No.4, pp.321-331.

Kaviany, M, 2002. Principles of Heat Transfer. New York, NY: Wiley.

Kim, S.J, 2008. "Damage Detection in Composite Laminates Using Coin-Tap Method", Proceedings of Acoustics Paris, Paris.

Klein, M, Ibarra-Castanedo, C, Bendada, A.H & Maldague, X, 2008a. "Thermographic Signal Processing Through Correlation Operators in Pulsed Thermography", in Thermosense XXX, SPIE Defense and Security Symposium, Vavilov, V.P & Burleigh, D.D (Eds.), Vol.6939, pp.693-915, Orlando, Florida, USA.

Klein, M, Bendada, A, Mariacristina Pilla, M,Ibarra-Castanedo, C & Maldague, X, 2008b. "Enhancing Infrared Images Contrast for Pulsed Thermography", 9th International Conference on Quantitative InfraRed Thermography, Krakow, Poland.

Klein, M, Bendada, A, Ibarra-Castanedo, C and Maldague, X, 2010. "A Hybrid Pulsed Thermography Processing Technique for the Depth Estimation of Subsurface Defects Combining TSR and PPT", 10th International Conference on Quantitative Infrared Thermography, Québec, Canada .

Krapez J.C & Balageas D., 1994. "Early Detection of Thermal Contrast in Pulsed Stimulated Infrared Thermography", Proceedings of the Quantitative InfraRed Thermography Conference, pp 260-266.

Krapez, J, Balegeas, D, Deom, A & Lepoutre, F, 1994b. "Early Detection by Stimulated Infrared Thermography", Advances in Signal Processing for Nondestructive Evaluation of Materials, Ed. Maldague, X, pp.303-321. The Nether-

lands: Kluwer Academic Published.

Maclachlan Spicer, J.W, Kerns, W.D, Aamodt, L.C & Murphy, J.C, 1991. "Time-resolved Infrared Radiometry (TRIR) of Multilayer Organic Coatings Using Surface and Subsurface Heating", in Thermosense XIII, Proc. SPIE, Baird, G.S (Ed.), Vol.1467, pp.311-321.

Madruga, F.J, Ibarra-Castanedo, C, Conde, O.M, López-Higuera, J.M & Maldague, X, 2008. "Automatic Data Processing Based on the Skewness Statistic Parameter for Subsurface Defect Detection by Active Infrared Thermography", 9th International Conference on Quantitative InfraRed Thermography, Krakow, Poland.

Madruga, F.J, Ibarra-Castanedo, C, Conde, O.M, Maldague, X.P & López-Higuera, J.M, 2009. "Enhanced Contrast Detection of Subsurface Defects by Pulsed Infrared Thermography Based on the Fourth Order Statistic Moment, Kurtosis", In SPIE Defense, Security, and Sensing, International Society for Optics and Photonics, pp.72990U-72990U.

Maierhofer, C, Reinhardt, H.W & Dobmann, G, 2010. "Non-Destructive Evaluation of Reinforced Concrete Structures: Non-Destructive Testing Methods", Woodhead Publishing Series in Civil and Structural Engineering, Elsevier Science.

Maierhofer, C, Myrach,P, Röllig & Steinfurth, H, 2014. "Validation of Active Thermography Techniques for the Characterization of CFRP Structures", 11th European Conference on Non-Destructive Testing (ECNDT 2014), Prague, Czech Republic.

Maillet, D, André, S, Batsale, J, Degiovanni, A & Moyne, C, 2000. "Thermal Quadrupoles: Solving the Heat Equation Through Integral Transforms", John Wiley and Sons, USA.

Maldague, X & Marinetti, S, 1996. "Pulse Phase Infrared Thermography", Journal of Applied Physics, Vol.79, No.5, pp.2694-2698.

Maldague, X, 2000. "Applications of Infrared Thermography in NonDestructive Evaluation", in Trends in Optical Nondestructive Testing, Rastogi, P (Ed.), Elsevier, pp.591-609.

Maldague, X.P, 2001. "Theory and Practice of Infrared Technology for Nondestructive Testing", Hoboken: John Wiley & Sons, Inc.

Maldague, X, Galmiche, F & Ziadi, A, 2002. "Advances in Pulsed Phase Thermography", Journal of Infrared Physics & Technology, Vol.43, pp.175-181.

Marin, E., 2010. "Characteristic Dimensions of Heat Transfer", Centro de Investigación en Ciencia Aplicada y Tecnología Avanzada Instituto Politécnico Nacional, Legaria 694, Col. Irrigación, C.P. Mexico.

Marinetti, S, Maldague, X & Prystay, M, 1997. "Calibration Procedure for Focal Plane Array Cameras and Noise Equivalent Material Loss for Quantitative Thermographic NDT", Materials Evaluation, Vol.55, No.3, pp.407-412.

Martin, R.E, Gyekenyesi, A.L & Shepard, S.M, 2003. "Interpreting the Results of Pulsed Thermography Data", Materials Evaluation, Vol.61, Issue 5, pp.611-616.

Mayr, G, Dietermayr, B, Hendorfer, G, & Sekelja, J, 2008. "Characterization of Defects in Curved CFRP Samples Using Pulsed Thermography and 3D Finite Element Simulation", In 9th International Conference on Quantitative Infrared Thermography, Krakow, Poland.

Meola, C & Carlomagno, G.M, 2004. "Recent Advances in the Use of Infrared Thermography", Measurement Science Technology, Vol.15, pp.27-58.

Nezadal, M, Schũr, J & Schmidt, L, 2013. "Imaging System for Non-Destructive Testing of Glass Fibre Reinforced Plastics", 5th International Symposium on NDT in Aerospace, Singapore.

López, F, Nicolau, V.P, Ibarra-Castanedo, C, Sfarra, S & Maldague, X, 2014a. "Comparative Study of Thermographic Signal Reconstruction and Partial Least Squares Thermography for Detection and Evaluation of Subsurface Defects", NDT & E International, Elsevier, Vol.66, pp.128-138.

López, F, Ibarra-Castanedo, C, Nicolau, V.P & Maldague, X, 2014b. "Optimization of Pulsed Thermography Inspection by Partial Least-squares Regression", NDT & E International, Vol.66, pp.128-138.

Omar, M, Hassan, M & Saito, K, 2005. "Optimizing Thermography Depth Probing with a Dynamic Thermal Point Spread Function, Infrared Physics & Technology, Vol.46, Issue 6, pp.506-514.

Olbrycht, R, Więcek, B, Gralewicz, G, Świątczak, T & Owczarek, G, 2007. "Comparison of Fourier and Wavelet Analyses for Defect Detection in Lock-in and Pulse Phase Thermography", Quantitative InfraRed Thermography Jour-

nal, Vol.4, Issue 2, pp.219-232.

Oswald-Tranta, B, Maier, A & Schledjewski, R, 2014. "Defect Depth Determination in a CFRP Structure Using TSR Technique", The 12th International Conference on Quantitative InfraRed Thermography, Bordeaux.

Özisik, M.N, 1985. "Heat Transfer ? A Basic Approach", McGraw-Hill, Singapore.

Park, G.H, Cho, H.H & Choi, M.R, 2008. "A Contrast Enhancement Method Using Dynamic Range Separate Histogram Equalization", IEEE Transactions on Consumer Electronics, Vol.54, pp.1981-1987.

Parker, W.J, Jenkins, R.J, Butler, C.P, Abbott, G.L, 1961. "Flash Method of Determining Thermal Diffusivity, Heat Capacity, and Thermal Conductivity", Journal of Applied Physics, Vol.32, Issue 9, pp.1679-1684.

Planck, M, 1914. "The Theory of Heat Radiation", 2nd Edition, P. Blakiston Son & Co.

Rahman, Z, Woodell, G.A & Jobson, D.J, 2001. "Retinex Image Enhancement: Application to Medical Images", Presented at the NASA workshop on New Partnerships in Medical Diagnostic Imaging, Greenbelt, Maryland.

Rajic, N, 2002a. "Principal Component Thermography", Defense Science and Technology Organisation Victoria (Australia) Aeronautical and Maritime Research Laboratory, Technical Report 012-294.

Rajic, N, 2002b "Principal Component Thermography for Flaw Contrast Enhancement and Flaw Depth Characterisation in Composite Structures", Composite Structures, Vol.58, No.4, pp.521-528.

Restrepo, A & Loaiza, H, 2012. "New Method for Basic Detection and Characterization of Flaws in Composite Slabs Through Finite Difference Thermal Contrast (FDTC)", 11th International Conference on Quantitative InfraRed Thermography, Naples, Italy.

Ringermacher, H.I, Mayton, D.J, Howard, D.R, Cassenti, B.N, 1998. "Review of Progress in Qualitative Nondestructive Evaluation", Plenum Press, Vol.17, pp.425-426.

Roche, J, Leroy, F & Balageas, D, 2013. "Images of Thermographic Signal Reconstruction Coefficients: A Simple Way for Rapid and Efficient Detection of

Discontinuities", Materials Evaluation, Vol.72, No.1, pp.73-82.

Roche, J.M, Leroy, F.H, Balageas, D.L, 2014. "Information Condensation in Defect Detection Using TSR Coefficients Images", The 12th International Conference on Quantitative InfraRed Thermography, Bordeaux, France.

Roche J.M & Balageas D, 2014. "Common Tools for Quantitative Time-resolved Pulse and Step Heating Thermography, Part II: Experimental Validation", Proceedings of the Quantitative InfraRed Thermography Conference.

Roemer, J, Pieczonka,L, Szwedo, M, Uhl, T & Staszewski, W.J, 2013. "Thermography of Metallic and Composite Structures - Review of Applications", International Workshop on Smart Materials, Structures & SHM NDT in Canada 2013 Conference & NDT for the Energy Industry, Calgary, Alberta, Canada.

Rybicki, G.B, & Lightman, A.P, 1979. "Radiative Processes in Astrophysics", John Wiley and Sons.

Saintey, M.B & Almond, D.P, 1995. "Defect Sizing by Transient Thermography II: A Numerical Treatment", Journal of Physics D: Applied Physics, Vol.28, pp.2539-2546.

Savitzky A & Golay, M.J.E, 1964. "Analytical Chemistry", Vol.36, pp.1627?1639.

Schuöcker, D, 1999. "High Power Lasers in Production Engineering", Imperial College Press.

Sebastian, M, 2011. Plexiglass Sheets, Fiberglass, UHMW, Polycarbonate & Engineering plastics. Available [Online]: http://www.plasticgenius.com/2011/05/infrared-and-ultraviolet-transmission.html. (Accessed 07 November 15).

Sedgewick, J, 2014. "Wavelength-spectrums-LED-xenon-tungsten", image, viewed 3 October 2015. Available [Online]: http://scientific.datacolor.com/white-balancing-and-accurate-color/.

Servais, P, 2006. "Development of a New NDT Method Using Thermography for Composite Inspection on Aircraft with Portable Military Thermal Imager", Proceedings of European Conference for Non-Destructive Testing - We.4.1.1.

Shannon, C.E, 1949. "Communication in presence of noise", Proc. IRE, Vol.37, pp.10-21.

Sheet, D, Garud, H, Suveer, A, Mahadevappa, M & Chatterjee, J, 2010. "Brightness Preserving Dynamic Fuzzy Histogram Equalization", in Consumer Electronics, IEEE Transactions, Vol.56, No.4, pp.2475-2480.

Shepard, S, Lahota, J, Rubadeux, B, Wang,D & Ahmed, T, 2003. "Reconstruction and Enhancement of Active Thermography Image Sequences", Optical Engineering, Vol.42, Issue 5, pp.1337-1342.

Shepard, S.M, 2007. "Flash Thermography of Aerospace Composites", IV Conferencia Panamericana de END Buenos Aires.

Shepard, S, 2014. "Approaches to Data Reduction, Visualization and Analysis in Thermographic Signal Reconstruction", Proceedings of Quantitative InfraRed Thermography 2014.

Stabik, J, Dybowska, A, Pluszyński, J, Szczepanik, M & Suchoń, L, 2010. "Magnetic Induction of Polymer Composites Filled with Ferrite Powders", World Academy of Materials and Manufacturing Engineering, Vol.41, Issue 1, pp.13-20.

Stehfest, H, 1970. "Algorithm 368: Numerical inversion of Laplace transform", Communication of the ACM, Vol.13, No.1, pp.47-49.

Steinberger, R, Valadas Leitaõ, T.I, Ladstätter, E, Pinter, G, Billinger, W & Lang, R,W, 2006. "Infrared Thermographic Techniques for Non-Destructive Damage Characterization of Carbon Fibre Reinforced Polymers during Tensile Fatigue Testing", International Journal of Fatigue, Vol.28, pp.1340-1347.

Štruc, V, Žibert, J & Pavešić, N, 2009. "Histogram Remapping as a Preprocessing Step for Robust Face Recognition", WSEAS Transactions on Information Science and Applications, Vol.6, No.3, pp.520-529.

Sun, J, 2003. U.S. Patent No.6,542,849. Washington, DC: U.S. Patent and Trademark Office.

Sun, J.G, 2006. "Analysis of Pulsed Thermography Methods for Defect Depth Prediction", Journal of Heat Transfer, Vol.128, No.4, pp.329-338.

Sun, B, Ma, Q & Zhao, H, 2007. "Fitting-Correlation Analysis of Pulsed Thermographic Sequence Data", Proceedings of the 2007 IEEE International Conference on Mechatronics and Automation.

Sultan, R, Guirguis, S, Younes, M & El-Soaly, E, 2012. "Active Infrared Thermography Technique for the Non Destructive Testing of Composite Mate-

rial", International Journal of Mechanical Engineering and Robotics research, Vol.1, No.3, pp.131-142.

Susa, M, Svaić, S, & Boras, I, 2007. "Pulse Thermography Applied on a Complex Structure Sample: Comparison and Analysis of Numerical and Experimental Results", in IV Pan American Conference for Non Destructive Testing.

Susa, M, Benitez, H, Ibarra-Castanedo, C, Loaiza, H, Bendada, H & Maldague, X, 2006. "Phase Contrast Using a Differentiated Absolute Contrast Method", Quantitative Infrared Thermography, Vol.3, pp.219-230.

Theodorakeas, P, Avdelidis, N.P, Hrissagis, K, Ibarra-Castanedo, C, Koui, M & Maldague, X, 2011. "Automated Transient Thermography for the Inspection of CFRP Structures: Experimental Results and Developed Procedures", In SPIE Defense, Security, and Sensing, International Society for Optics and Photonics, pp.80130W-80130W.

Theodorakeas, P, Avdelidis, N.P, Ibarra-Castanedo, C, Koui, M, & Maldague, X, 2014. "Pulsed Thermographic Assessment of CFRP Structures: Experimental Results and Image Analysis Tools", in SPIE Smart Structures and Materials: Nondestructive Evaluation and Health Monitoring, pp.90620F-90620F. International Society for Optics and Photonics.

Usamentiaga,R, Venegas, P, Guerediaga, J, Vega, L & López, I, 2012. "A Quantitative Comparison of Stimulation and Post-Processing Thermographic Inspection Methods Applied to Aeronautical Carbon Fiber Reinforced Polymer",11th International Conference on Quantitative InfraRed Thermography.

Usamentiaga, R, Venegas, P, Guerediaga, J & Vega, L, 2014. "Towards Automatic Defect Detection in Carbon Fiber Composites Using Active Thermography", The 12th International Conference on Quantitative InfraRed Thermography, Bordeaux.

Varis, J, Rantala, J & Hartikainen, J, 1995. "Numerical Study on the Effects of Line Heating in Layered Anisotropic Carbon Fiber Composites", Research in Nondestructive Evaluation, Vol.6, No.2, pp.69-83.

Vavilov, V, Maldague, X, Dufort, B, Robitaille, F & Picard, J, 1993. "Thermal Nondestructive Testing of Carbon Epoxy Composites: Detailed Analysis and Data Processing", NDT & E International, Vol.26, No.2, pp.85-95.

Vavilov, V, Nesteruk, D, Shiryaev, V, Ivanov, A, & Swiderski, W, 2010. "Thermal (Infrared) Tomography: Terminology, Principal Procedures, and Application to Nondestructive Testing of Composite Materials", Russian Journal of

Nondestructive Testing, Vol.46, No.3, pp.151-161.

Venegas, P, Usamentiagau, R, Vega, L, Guerediaga, J, Jorge, I, López, I & Sáez de Ocáriz, I, 2012. "Image and Data Processing Techniques Applied to Infrared Thermographic NonDestructive Inspections of Aeronautical Composite Components", 4th International Symposium on NDT in Aerospace - We.2.A.1.

Winfree, W.P & Zalameda, J.N, 2003. "Thermographic Determination of Delamination Depth in Composites" Thermosense XXV, Cramer, K.E & Maldague, X.P Eds., Proceedings of SPIE Vol. 5073.

Zalameda, J.N, Rajic, N, & Winfree, W, 2003. "A Comparison of Image Processing Algorithms for Thermal Nondestructive Evaluation", SPIE Proc. Thermosense XXV, Vol.5073, pp.374-385.

Zauner, G, Mayr, G & Hendorfer, G, 2010. "Subsurface Defect Characterization in Pulsed Phase Thermography by Means of Wavelet Analysis", In 2nd International Symposium on NDT in Aerospace, Tu, Vol.1.